Optogenetic Methods to Regulate Water Transport and Purify Proteins
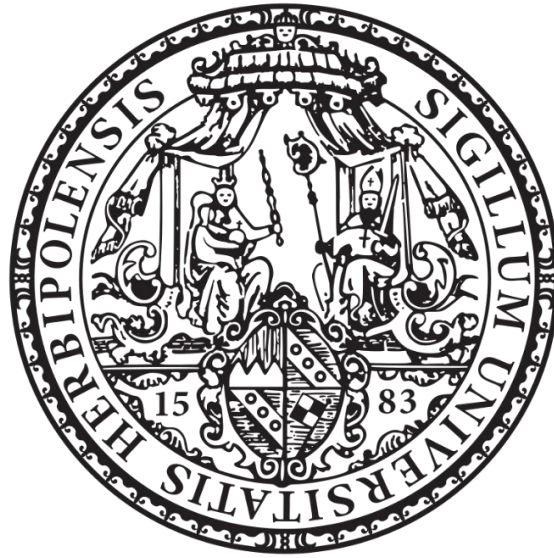
Doctoral thesis for a doctoral degree

in Julius-Maximilians-Universität Würzburg

Ruijing Tang

From Jiangsu, China

Würzburg, 2021

Submitted on: ………………………………………………………..

Members of the Promotionskomitee:

Chairperson:

Primary Supervisor: Prof. Dr. Georg Nagel

Secondary Supervisor: Prof. Dr. Robert Kittel

Third Supervisor: Prof. Dr. Thomas Müller

Date of Public Defense: ……………………………………….……

Date of Receipt of Certificates: …………………………………………

Contents

Abstract

Water transport through the water channels, aquaporins (AQPs), is involved in epithelial fluid secretion and absorption, cell migration, brain edema, adipocyte metabolism, and other physiological or pathological functions. Modulation of AQP function has therapeutic potential in edema, cancer, obesity, brain injury, glaucoma, etc. The function of AQPs is in response to the osmotic gradient that is formed by the concentration differences of ions or small molecules. In terms of brain edema, it is a pathophysiological condition, resulting from dysfunction of the plasma membrane that causes a disorder of intracellular ion homeostasis and thus increases intracellular fluid content. Optogenetics can be used to regulate ion transport easily by light with temporal and spatial precision. Therefore, if we control the cell ion influx, boosting the water transport through AQPs, this will help to investigate the pathological mechanisms in e.g. brain edema. To this end, I investigated the possibility for optogenetic manipulating water transport in *Xenopus* oocytes. The main ions in *Xenopus* oocyte cytoplasm are ~10 mM Na^+, ~50 mM Cl^- and ~100 mM K^+, similar to the mammalian cell physiological condition. Three light-gated channels, ChR2-XXM 2.0 (light-gated cation channel), *Gt*ACR1 (light-gated anion channel) and SthK-bPAC (light-gated potassium channel), were used in my study to regulate ion transport by light and thus manipulate the osmotic gradient and water transport. To increase water flow, I also used coexpression of AQP1. When expressing ChR2-XXM 2.0 and *Gt*ACR1 together, mainly Na^+ influx was triggered by ChR2-XXM2.0 under blue light illumination, which then made the membrane potential more positive and facilitated Cl^- influx by *Gt*ACR1. Due to this inward movement of Na^+ and Cl^-, the osmotic gradient was formed to trigger water influx through AQP1. Large amounts of water uptake can speedily increase the oocyte volume until membrane rupture. Next, when co-expressing *Gt*ACR1 and SthK-bPAC, water efflux will be triggered with blue light because of the light-gated KCl efflux and then oocyte shrinking could be observed.

I also developed an optogenetic protein purification method based on a light-induced protein interactive system. Currently, the most common protein purification method is based on affinity chromatography, which requires different chromatography columns and harsh conditions, such as acidic pH 4.5 - 6 and/or adding imidazole or high salt concentration, to elute and collect the purified proteins. The change in conditions could influence the activity of target proteins. So, an easy and flexible protein purification

method based on the photo-induced protein interactive system iLID was designed, which regulates protein binding with light in mild conditions and does not require a change of solution composition. For expression in *E. coli*, the blue light-sensitive part of iLID, the LOV2 domain, was fused with a membrane anchor and expressed in the plasma membrane, and the other binding partner, SspB, was fused with the protein of interest (POI), expressed in the cytosol. The plasma membrane fraction and the soluble cytosolic fraction of *E. coli* can be easily separated by centrifugation. The SspB-POI can be then captured to the membrane fraction by light stimulation and released to clean buffer in the dark after washing. This method does not require any specific column and functions in mild conditions, which are very flexible at scale and will facilitate extensive protein engineering and purification of proteins, sensitive to changed buffer conditions.

Zusammenfassung

Der Wassertransport durch die Wasserkanäle, Aquaporine (AQPs), ist unter anderem an der Sekretion und Absorption der Epithelflüssigkeit, der Zellmigration, dem Hirnödem und dem Adipozytenstoffwechsel beteiligt. Die Modulation der AQP-Funktion hat therapeutisches Potenzial bei Ödemen, Krebs, Fettleibigkeit, Hirnverletzungen, Glaukom usw. Die Funktion von AQPs reagiert auf den osmotischen Gradienten, der durch Konzentrationsunterschiede von Ionen oder kleinen Molekülen gebildet wird. In Bezug auf das Hirnödem handelt es sich um einen pathophysiologischen Zustand, der aus einer Funktionsstörung der Plasmamembran resultiert und eine Störung der intrazellulären Ionenhomöostase verursacht und somit den intrazellulären Wassergehalt erhöht. Die Optogenetik kann verwendet werden, um den Ionentransport durch Licht mit zeitlicher und räumlicher Präzision leicht zu regulieren. Wenn wir also den Ioneneinstrom in die Zelle erhöhen, wird dies den Wasserimport durch AQPs fördern. Eine solche Methode den Wassertransport zu kontrollieren könnte dazu beitragen, die pathologischen Mechanismen bei Hirnödemen besser zu untersuchen und zu verstehen. Zu diesem Zweck unternahm ich Versuche für die optogenetische Manipulation des Wassertransports in Xenopus-Oozyten. Die Hauptionen im Xenopus-Oozyten-Zytoplasma bestehen aus ~ 10 mM Na^+, ~ 50 mM Cl^- und ~ 100 mM K^+, ähnlich dem physiologischen Zustand der Säugetierzellen. Drei lichtgesteuerte Kanäle, ChR2-XXM 2.0 (lichtgesteuerter Kationenkanal), GtACR1 (lichtgesteuerter Anionenkanal) und SthK-bPAC (lichtgesteuerter Kaliumkanal), wurden in meiner Studie zur Regulierung des Ionentransports durch Licht verwendet. Außerdem erhöhte ich durch Coexpression von AQP1 den Wasserfluss. Bei gleichzeitiger Expression von ChR2-XXM 2.0 und GtACR1 wurde der Na^+-Einstrom hauptsächlich durch ChR2-XXM2.0 unter Blaulichtbeleuchtung ausgelöst, wodurch das Membranpotential positiver wurde und der Cl^- Einstrom durch GtACR1 erleichtert wurde. Aufgrund dieser Einwärtsbewegung von Na^+ und Cl^- wurde der osmotische Gradient gebildet, um den Wasserzufluss zu erhöhen bis einzelne Oozyten platzten. Dagegen wurde bei der Coexpression von GtACR1 und SthK-bPAC der Wasserausfluss aufgrund des lichtgesteuerten KCl-Ausflusses mit blauem Licht ausgelöst und konnte ein Schrumpfen der Eizellen beobachtet werden.

Ich habe auch eine optogenetische Proteinreinigungsmethode entwickelt, die auf einem lichtinduzierten interaktiven Proteinsystem basiert. Gegenwärtig basiert das

gebräuchlichste Proteinreinigungsverfahren auf der Affinitätschromatographie, die unterschiedliche Chromatographiesäulen und raue Bedingungen wie sauren pH 4.5 bis 6 und/oder Zugabe von Imidazol oder hohe Salzkonzentration erfordert, um die gereinigten Proteine zu eluieren und zu sammeln. Die Änderung dieser Bedingungen könnte die Aktivität des Zielproteins beeinflussen. Daher wurde eine einfache und flexible Proteinreinigungsmethode entwickelt, die auf dem photoinduzierten interaktiven Proteinsystem iLID basiert und die Proteinbindung mit Licht unter milden Bedingungen reguliert und keinen Wechsel der Lösungsbedingungen erfordert. In *E. coli* wurde der Licht-empfindliche Teil von iLID, die LOV2-Domäne, mit einem Membrananker fusioniert und in der Plasmamembran exprimiert, und der andere Teil, SspB, wurde mit dem Protein von Interesse (POI) fusioniert, das im Cytosol exprimiert wurde. Die Plasmamembranfraktion und die lösliche cytosolische Fraktion von *E. coli* können leicht durch Zentrifugation getrennt werden. Das zu reinigende Protein (SspB-POI) kann dann durch Lichtstimulation in der Membranfraktion eingefangen und nach dem Waschen im Dunkeln freigesetzt werden. Diese Methode erfordert keine spezifischen Säulen und funktioniert unter milden Bedingungen, die im Maßstab sehr flexibel sind und ein umfassendes Protein-Engineering und die Reinigung von Proteinen ermöglichen, die gegenüber geänderten Pufferbedingungen empfindlich sind.

1 Introduction

1.1 Aquaporin

Aquaporins (AQPs) are a family of plasma membrane water channels that facilitate water transport in response to osmotic gradients. After the first discovery of AQP1 (originally known as CHIP28 [1]) in red blood cells, 13 mammalian AQPs (AQP0-12) have been demonstrated widely in specific cells of various organs and tissues. Unlike simple diffusion that water slowly crosses cell membrane through the lipid bilayer, AQPs as water-selective channels exhibit rapid transmembrane water flow and play a critical role in maintaining water homeostasis in living cells. In addition, a subset of AQPs called aquaglyceroporins also transport glycerol, small polar solutes and gases. Thus, AQPs are involved in many biological functions, including transepithelial fluid transport, cell migration, brain edema, neuroexcitation, cell proliferation, adipocyte metabolism and epidermal water retention [2, 3].

1.1.1 Aquaporin structure

AQP monomer as integral membrane channel is ~30 kDa and consist of six membrane-spanning helical segments (known as M1, M2, M4–M6 and M8), two half helices that do not span the entire membrane (M3 and M7) and five connecting loops (loops a–e) (Figure 1.1a). The N- and C-terminal are located in the cytoplasm to form the cytoplasmic vestibule with loop b and d. The cytoplasmic and extracellular vestibules connected by a narrow aqueous pore co-operate to form the first filter to prevent the permeation of large molecules. In this narrow aqueous pore, two Asn-Pro-Ala (NPA) motifs are found in the N- and C-terminal half (M3 and M7), respectively (Figure 1.1b). Another conserved part in the pore is aromatic residues and an arginine (the ar/R constriction) (Figure 1.1b). The molecular dynamics simulations have elucidated that a synergistic effect between the NPA motifs and the ar/R prevents proton conduction and blocks cation transport according to Grotthuss mechanism. Whereas the NPA motifs are hydrogen-bond donors and acceptors that facilitate water transport. The diameter for the aqueous pore, which is the nearest region made up by the ar/R constriction, is different between classical water-selective aquaporins and aquaglyceroporins. For example, human AQP1 is ~2.8 Å and human AQP4 is ~1.5 Å that sterically excludes the transport of glycerol. On the other hand, the diameter for aquaglyceroporins, like human AQP3 and AQP7, is ~3.4 Å exhibiting more open structure for glycerol transport [4, 5].

AQPs are organized in the membrane as tetramers, and each monomer forms the individual water-conducting pore (Figure 1.1c). The tetramer structure studies about AQP1 highlighted that the hydrophobic helices in the monomer are placed on the outside face of the tetramer, whereas the hydrophilic helices are towards the center [6]. In addition, AQP4 further assembles into higher-order supramolecular in the plasma membrane called orthogonal arrays of particles (OAP) stabilized by the interaction of N-terminal residues in the monomeric units [7].
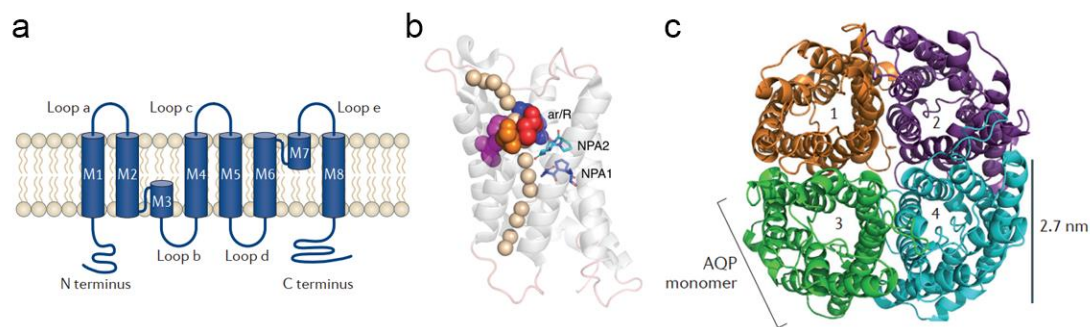
Figure 1.1 Structure of aquaporin.

(a). A schematic of monomer AQP membrane topography.

(b). Monomeric lateral view of the water path (wheat spheres) through human AQP5. Sticks: Asn-Pro-Ala (NPA), Spacefill spheres: the aromatic-arginine (ar/R) constrictions.

(c). A top view of the extracellular face of bovine AQP1 homotetramer with monomers labeled 1–4. Taken from [8, 9].

1.1.2 Water transport regulation

AQPs are important to maintain a constant cell volume and intracellular environment for cell homeostasis. Even small water content changes in cells can alter the concentration of intracellular compartments involving signaling cascades and cell-to-cell communication. To keep cell homeostasis, the permeability of AQPs is always regulated via post-translational modifications including phosphorylation, ubiquitination and glutathionylation. In the renal inner medulla, AQP2 as PKA target is phosphorylated at Ser256 leading to water permeable increasing [10]. To control brain edema and seizure, AQP4 has two phosphorylation sites with opposite effects on water permeability: Ser180 inhibits water transport and Ser111 improves water transport [11]. In addition, the expression level of AQP4 during retinal injury is related to ubiquitin-dependent regulation [12]. Besides AQP4, Blanc et al. [13] have also found that the secretion and location of AQP1 are also regulated by ubiquitination. S-

glutathionylation modification is important to protect cysteine residue from oxidation during redox imbalance, and AQP2 has been reported to involve S-glutathionylation, by which AQP2-dependent water reabsorption in kidney is protected from ROS disturbing [14].

The direct interactions between AQPs and some regulatory proteins, like calmodulin (CaM) and LYST-interacting protein 5 (LIP5), also regulate water conduction by gating or trafficking [15]. The cytoplasmic C-terminal helix is a typical structure among AQPs, in which the hydrophobic side is proposed to mediate the interaction between CaM and AQPs. For example, Ca^{2+}-dependent binding of CaM to APQ0 C-terminal helix contributes to a conformational change that the water-conducting pore is closed [16]. LIP5 also interacts with the C-terminal tail of AQP2 and increases AQP2 degradation, decreasing the abundance of AQP2 in the kidney collecting duct principal cells [17]. Besides gating and trafficking, Stokum et al. [18] found a new water transport regulatory model based on a heterocomplex, in which AQP4 co-assembles with the sulfonylurea receptor 1-transient receptor potential melastatin 4 (SUR1-TRPM4) to form water/ion channel complex SUR1-TRPM4-AQP4 (Figure 1.2). SUR1 physically increases the Ca^{2+} sensitivity of TRPM4 and decreases its desensitization leading to larger Na^+ influx and raised local osmotic pressure, which then drives water influx through AQP4 resulting in astrocytes swelling in a cold injury model of brain edema [19, 20].
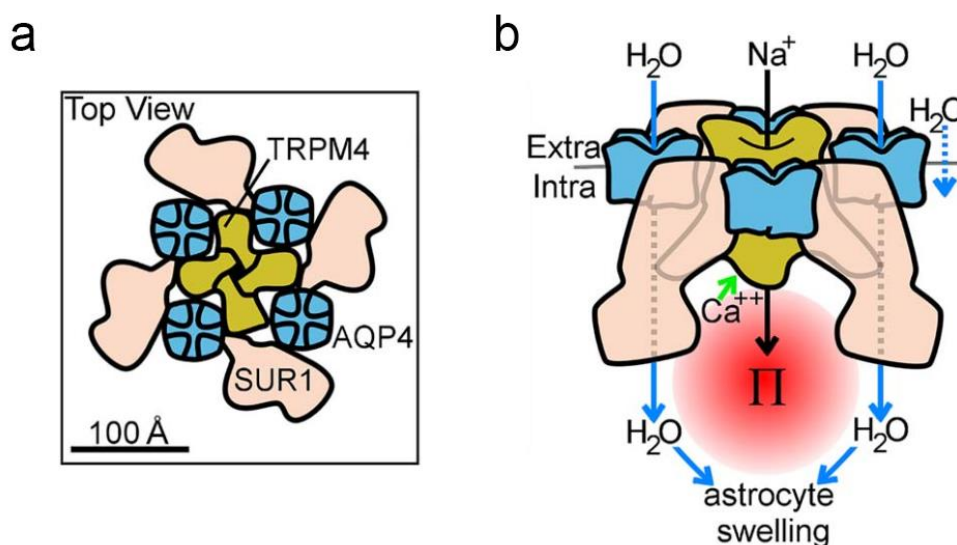

Figure 1.2 Model of SUR1-TRPM4-AQP4 structure and function.

(a). The putative model of SUR1-TRPM4-AQP4 showed AQP4 tetramers (blue) intercalated between SUR1 monomers (pink), and interacted with tetrameric TRPM4 (yellow).

(b). Model of SUR1-TRPM4-AQP4 induced water flux (blue arrows) through AQP4 and the plasmalemma (rightmost arrow). Taken from [18].

Water permeability of AQPs can also be artificially controlled by adding some inhibitors, like Hg^{2+} and other heavy metal ions, which are efficient to prevent water transport. However, heavy metal ions are too toxic for cells. Baumgart et al. [21] genetically modified AQPs with chromophore-assisted light inactivation system (CALI) to inhibit the water transport. The production of oxygen radicals from the fluorophore of CALI after light exposure destroyed the fused AQPs, which is irreversible for water transport regulation. In my thesis, I will try to regulate water transport by blue light based on optogenetic toolboxes.

1.2 Optogenetic toolbox

Optogenetics, which is a rapid, reversible and noninvasive technique that involves protein function and thus cell physiology with light, has been widely used in biological research. The optogenetic tools are not restricted to rhodopsins, but expand to photoactivated adenylyl cyclase (PACs) and light-induced dimers (such as Phytochromes, Cryptochromes and LOV domains,)

1.2.1 Microbial rhodopsins

Rhodopsin is a photoreceptor protein containing the protein opsin of typical seven-transmembrane helix and a covalently bound retinal as chromophore, divided into two superfamilies: microbial rhodopsin (type I) and animal rhodopsin (type II) [22]. Type II rhodopsins are present in eukaryotes and function as G protein-coupled receptors (GPCRs) via conformational change to transduce light information to cell signaling following photon absorption of 11-*cis*-retinal. Type I rhodopsins are found in prokaryotes, algae and fungi binding with the all-*trans* retinal that is isomerized to the 13-*cis* retinal after photon absorption [23]. In addition, a conserved lysine in microbial rhodopsin is covalently bound to the chromosome to form a Schiff base. Because of single and small light-sensitive structure with reversible photochemical reaction and fast kinetics to modulate neuron cells, microbial rhodopsins as light-activated pumps,

light-gated ion channels and enzyme rhodopsins have led to the great development of optogenetics.

1.2.1.1 light-activated pumps

Bacteriorhodopsin (BR) is the first microbial rhodopsin found in the purple membrane of *Halobacterium salinarum*, and functions as a light-activated outward proton pump to maintain a proton gradient across the cellular membrane [24, 25]. Archaerhodopsin 3 (Arch) is a BR-type proton pump from *halorubrum sodomense*, and can generate hyperpolarizing current for the silencing of neurons [26]. The light-activated inward chloride pumps, like Halorhodopsin (*Hs*HR) and *Np*HR, were also discovered. Following the modification for *Np*HR with ER export motifs and the C-terminal trafficking signal from the potassium channel Kir2.1, its membrane targeting efficiency is improved, thereby resulting in enhanced photocurrent amplitude as one popular neural silencing tool [27]. Besides proton and chloride pumps, a light-activated sodium pump was then identified from marine flavobacterium *Krokinobacter eikastus* [28]. After N- and C-terminal modification, the enhanced KR2 (eKR2), like Arch and *Np*HR, has been used to silence mouse hippocampal *in vitro* as a reliable inhibitory optogenetic tool [29].

1.2.1.2 light-gated ion channels

The first identified light-gated cation channels from microbial rhodopsins are two isoforms: channelrhodopsin 1 (ChR1) and 2 (ChR2) [30, 31]. Both of them are membrane proteins with seven transmembrane helices and a C-terminal cytosolic domain, and can be expressed in *Xenopus* oocyte as a functional channel in response to blue light. Because of light sensitivity, fast on and off kinetics and larger photocurrent, ChR2 is now a widely used optogenetic tool for membrane depolarization [32, 33]. To improve the utilization of ChR2 in neuroscience, some mutants have been made based on its structure information, and these mutants exhibit superior properties compared to WT ChR2. Mutation of ChR2 C128 or D156 decreases the closing kinetics and increases the light sensitivity [34, 35]. In addition, the ChR2 D156C mutant (ChR2-XXL) exhibits very large photocurrent as well as D156H (ChR2-XXM). But the kinetics of XXM is faster than XXL, and the sodium and calcium conductance in XXM are both increased compared to WT ChR2 and XXL [36]. The E90R mutant of ChR2

can even change cation conductance to anion conductance [37]. Two natural anion channelrhodopsins (ACRs) have also been discovered afterward named *Gt*ACR1 and *Gt*ACR2 [38]. The maximum excitation wavelength of *Gt*ACR1 is at 515 nm that is slightly red-shifted, and 470 nm for *Gt*ACR2. Compared to ion-pumping rhodopsins, *Gt*ACRs have strict anion-selectivity, higher light sensitivity and larger photocurrent leading to inhibit behavior in Drosophila and larval zebrafish [39, 40]. Mann et al. [41] and Messier et al. [42] modified *Gt*ACRs with a trafficking signal and a C-terminal targeting motif from Kv2.1 increasing membrane targeting and decreasing axonal excitation that made *Gt*ACRs more effective for optogenetic inhibition in mammalian cells.

Kleinlogel et al. [43] fused ChR2 and *Np*HR together by β linker, a transmembrane helix from the β subunit of the rat gastric H^+/K^+-ATPase. These two rhodopsins can then be expressed in the same ratio and location in a cell to achieve precise control for neuronal activation and silencing. In my thesis, I will also fuse ChR2 with *Gt*ACR1 by β linker and then test ion-gradient formation efficiency in *Xenopus* oocyte in response to blue light, which could be used to regulate water transport.

1.2.1.3 Enzyme rhodopsins

The rhodopsin guanylyl cyclase, BeGC1, was found in fungus *Blastocladiella emersonii* containing microbial rhodopsin domain and guanylyl cyclase catalytic domain [44]. The light-regulated guanylyl cyclase activity of BeGC1 was further characterized by heterologous expression in cells and animals, and renamed as *Be*CyclOp [45, 46]. On the other hand, the first rhodopsin phosphodiesterase (RhoPDE) was identified from *Salpingoeca rosetta*, which shows 100 times higher hydrolysis activity for cGMP than that of cAMP [47]. Both BeCyclop and *Sr*RhoPDE exhibit the same structure of eight transmembrane helices and cytosolic N and C terminals that function as a pair of optogenetic cGMP manipulation tools. Two-component cyclase opsins (2c-Cyclops), *Cr*2c-Cyclop1 from *Chlamydomonas reinhardtii* and *Vc*2c-Cyclop1 from *Volvox carteri*, are recently characterized as light-inhibited guanylyl cyclase, and also comprised of eight transmembrane helices. cGMP production by these two opsins is constant under dark, but inhibited resulting from light-blocked phosphoryl transfer in 2c-Cyclops [48].

1.2.2 light-induced dimers

The chemically induced dimerization (CID) system is a traditional approach to bring two proteins together to form a homodimer or heterodimer, and then manipulates protein folding, activation, location and degradation in the living system [49]. Since the first application of rapamycin-inducible FKBP/FRB in gene expressing regulation, this chemical system has dominated the field of small molecular-induced heterodimer pathway [50]. However, the limitation includes rapamycin adding, dosage control, poor reversibility and lack of spatial control in living cells or organs. With the development of optogenetics, more and more light-induced dimers have been designed with the feature of high specific binding affinity, reversibility and easy spatial control based on photosensitive proteins, such as phytochromes (Phy), cryptochromes (CRY) and LOV domain-based photoreceptors.

1.2.2.1 Phytochrome

Phytochromes are originally defined as the photoreceptors regulating multiple aspects of plant photomorphogenesis such as seed germination, de-etiolation, stem growth, pigmentation and flowering. In *Arabidopsis*, there are five phytochromes named PhyA-PhyE as soluble and dimeric chromoprotein with two ~125 kDa polypeptides, which monitor the presence, absence, wavelength and intensity of light in the red/far-red region [51-53]. Each polypeptide folds into two structure domains: N-terminal photosensory domain that contains a covalently linked tetrapyrrole chromophore, phytochromobilin (PCB) and C-terminal domain that mediates homodimerization [54].

In 1959, Butler et al. [55] first revealed two stable, interconvertible forms of Phy: a red-light-absorbing Pr state and a far-red-light absorbing Pfr state. Phy binds PCB by a thioether linkage to a cysteine residue in the conserved domain of Phy. After absorption of red light (660 nm), PCB isomerization changes from "Z" to "E" in the C15/C16 double bond leading to the change of Pr state to Pfr state (Figure 1.3a and b). Pfr state can then be converted to Pr state in the dark or much faster by far-red light (750 nm) [56, 57]. Normally, Pfr state acts as biologically active via initiating an intracellular transduction process that alters the expression of selected genes for directing plant photomorphogenesis, whereas converting to biologically inactive form of Pr state can stop this process [51]. The mechanism of how Phys transduce light information to regulate gene expression is not clear until the identification of a phytochrome-

interacting factor, PIF3, which is a basic helix-loop-helix protein belonging to transcriptional regulators. In addition, PIF3 binds to C-terminal domains of Phys in the state of Prf (Figure 1.3c and d) [58, 59].
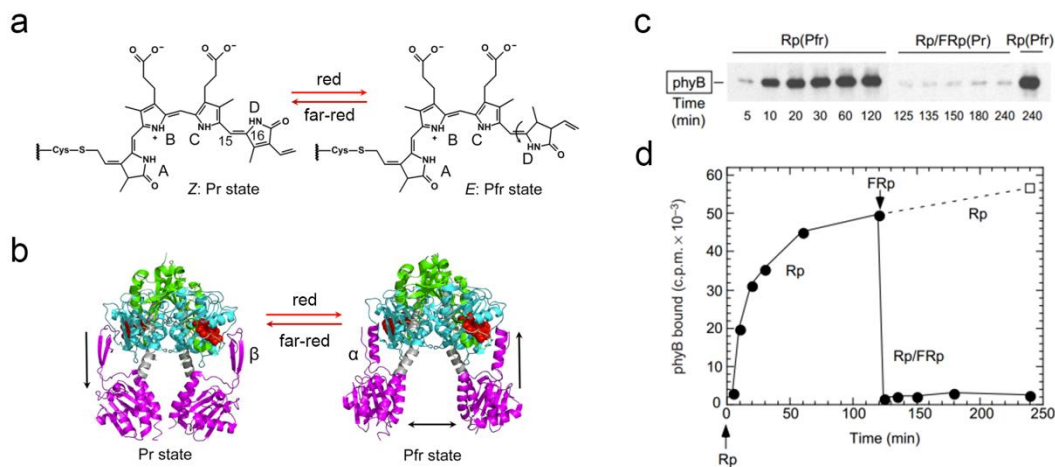
Figure 1.3 Light-driven changes of phytochromes.

(a). Reversible Pr−Pfr isomerization of the C15/C16 double bond in PCB under illumination with red and far-red light.

(b). Light-driven structural rearrangements in phytochrome. α-Helix and β-sheet secondary structures of the PHY-tongue in Pr and Pfr states are indicated, respectively.

(c). The binding of Pfr/Pr form of phytochrome B to PIF3.

(d). Quantitative determination of the amounts of PIF3-bound. Taken from [57, 59].

Shimizu-Sato et al. [60] first exploited PhyB-PIF3 as a light-switchable gene expression system that can be induced rapidly and reversibly by short light pulses in yeast cells. The PhyB-PIF3 dimer was then used to regulate the assembly of split protein and control the interaction between Cdc42 and Wasp *in vitro* [61, 62]. However, Levskaya et al. [63] pointed out that PhyB-PIF3 as a light-induced dimer exhibits relatively weak binding strength and slow reverse kinetics for *in vivo* spatiotemporal control of signaling. Thus, they improved the Phy-based light-induced dimer by a new design of PhyB-PIF6 that targeted protein precisely and reversibly to cell membrane with subcellular spatial resolution and subsecond time resolution. The disadvantage of the PhyB-PIF system is that mammalian cells do not express PCB, which should be artificially added. To solve this problem, Uda et al. [64] designed an expression vector that co-expressed HO1 and PcyA with Ferredoxin and Ferredoxin-NADP$^+$ reductase for PCB synthesis in mammalian cells. In addition, Kaberniuk et al. [65] characterized another Phy-based dimer of BphP1-PpsR2 from *Rhodopseudomonas palustris* bacteria,

in which the chromophore is biliverdin that generally exists in mammalian cells. In addition, as red and far-red light can easily penetrate thick tissues, PhyB-PIF has been widely applied for optogenetic applications, such as the control of protein or organelle localization [66], cell signaling [67] and gene expression [68, 69].

1.2.2.2 Cryptochrome

In 1993, *HY4* gene encoding a blue light photoreceptor, cryptochrome 1 (CRY1), was isolated from *A. thaliana* [70]. It is a 75 kDa flavoprotein that noncovalently binds flavin adenine dinucleotide (FAD) mediating blue light-dependent regulation of seeding development and inhibition of hypocotyl [71, 72]. CRY2, another flavin-type blue light receptor, shows 51% identical in amino acid sequence to CRY1, inhibits hypocotyl elongation and stimulates cotyledon opening under lower intensities of blue light [73].

CRYs includes two domains: N-terminal photolyase-homologous region (PHR) domain and C-terminal domain of various lengths and sequences. The PHR domain is important to facilitate the homodimer formation of CRY2 [74]. Up to now, two mechanisms have been proposed to explain the photoexcitation of cryptochromes based on electron transfer and phosphorylation [75, 76]. (1) The oxidized flavin as a ground-state chromophore in CRYs absorbs blue light effectively, then reduced to $FADH_2$ (or $FADH^-$). From oxidized flavin to reduced flavin, it triggers the conformational change of CRYs and the subsequent signal transduction. This photocycle is finished following the reduced flavin back to oxidized flavin under dark (Figure 1.4a); (2) Given that the PHR domain in CRY1 binds ATP in FAD-access cavity and CRY1 catalyzes autophosphorylation, photoactivation triggers an electron transport from FAD to ATP facilitating phosphortransfer from ATP to a residue of the C-terminal domain of CRY1 (Figure 1.4b). The phosphorylated C-terminal of CRYs separated from PHY domain triggers or alters the interaction between CRYs and their signaling partners (Figure 1.4c). For example, CRY-interacting basic-helix-loop-helix 1 (CIB1) is a transcription factor from *A. thaliana*, which controls gene expression to regulate floral initiation in a blue-light dependent CRY2-interacting manner [77].
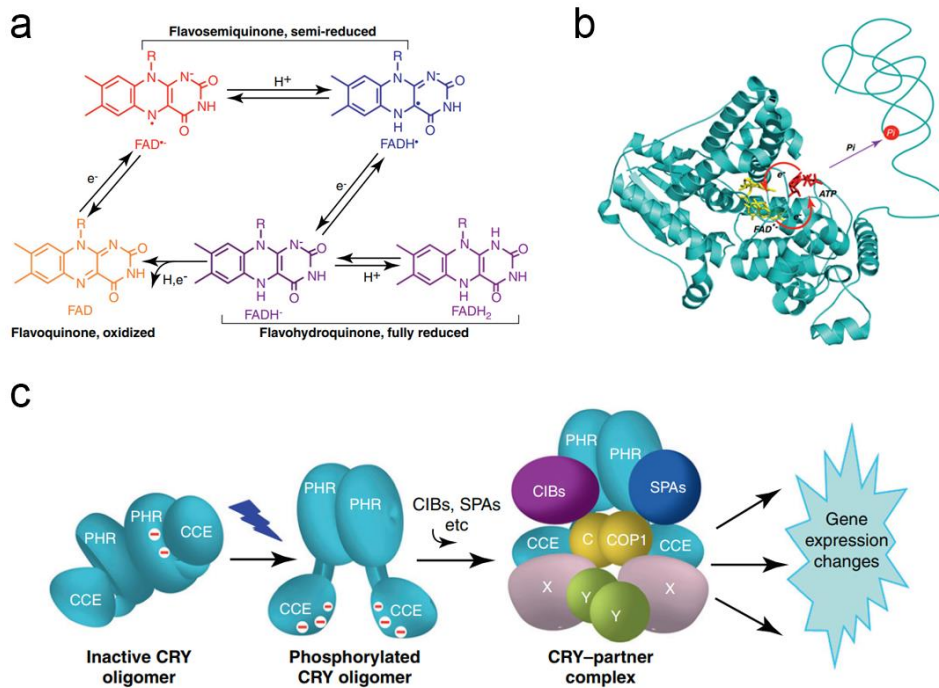
Figure 1.4 Photoexcitation of cryptochromes.

(a). Five possible redox forms of flavins. R: side groups of flavins.

(b). The photolyase-like cyclic electron shuttle model of cryptochrome photoexcitation.

(c). Signal transduction of cryptochromes: photoexcited cryptochrome changes conformation to initiate signal transduction by interacting with signaling proteins including CIB1. Taken from [75, 76]

The photoactivated dimer of CRY2/CIB1 was designed as a blue light-dependent optogenetic tool by Kennedy et al. [78] to relocate protein with subsecond time resolution and control the assembly of split protein fragments to recover activity. To avoid nuclear localization, the signal residues in both CRY2 and CIB1 are mutated and CIB1 is further truncated to CIBN. In addition, upon blue illumination the PHR domain in CRY2 N-terminal can also form reversible oligomeric "photobodies" with similar clustered and uncluttered kinetics [79]. The endogenous transmembrane receptors, like LRR6 and TRKs, can constantly transduce downstream cell signaling after fusing the PHR domain to the receptor binding domain under blue illumination with the existence of ligands [79, 80]. To sum up, CRY2-derived light-induced dimers are useful optogenetic tools for achieving high binding efficiency and fast kinetics and inducing various cellular functions, such as cell motility [81], gene expression [82], functional lipid signaling [83], and organelle transport [84, 85].

1.2.2.3 Phototropin

The phototropins (phot1 and phot2) are characterized as blue-light receptors in plants presenting functions in phototropism, chloroplast migration stomata opening and leaf expansion in *Arabidopsis* [86]. This photoreceptor contains a serine/threonine kinase domain (PKD) in the C-terminal, and two photoreceptive domains, LOV1 and LOV2 (light, oxygen and voltage-sensing), in the N-terminal. Each LOV domain contains a core of Per-Arnt-Sim (PAS) with the binding of flavin mononucleotide (FMN) noncovalently as a chromophore. After photoexcitation, the conformational change is observed in the linker region between LOV2 domain and PKD resulting from four-step photoreactive cycle in FMN: (1) under dark, the typical absorption of oxidized flavin is around 450nm (D450); (2) under blue illumination, the photo-intermediate is formed in a triplet-excited state (L660); (3) isoalloxazine ring of FMN forms an adduct with a conserved cysteine in LOV domain (S390 I); (4) the adduct formation leads to the conformational change of LOV domain (S390 II) (Figure 1.5a) [87]. Interestingly, before photoexcitation, LOV2 domain is docked in the cleft of PKD, which is similar to the interactive model of PKA/PKI [87]. The conformational change of LOV2 then contributes to the dissociation from PKD that will phosphorylate itself and other substrates involved in the light signal transduction *in vivo*. In addition, the conformational change of LOV2 domain is accompanied by the displacement and unfolding of the Jα-helix, which is the extension of LOV2 domain at the C-terminal to link with PKD (Figure 1.5b) [88].
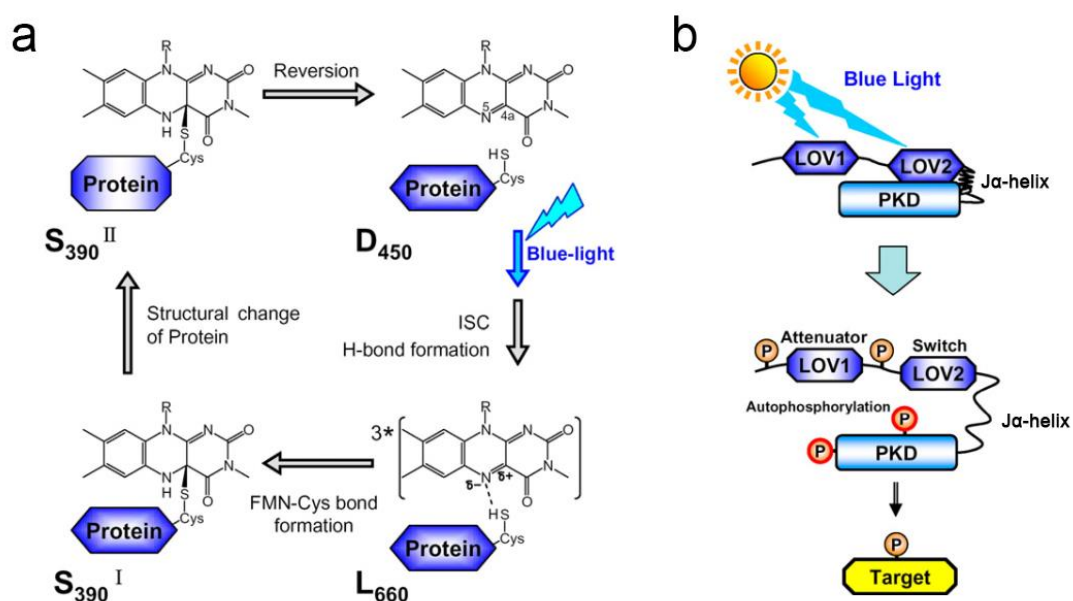

Figure 1.5 Proposed photoreaction scheme of phototropin.

(a). Photocycle of flavin mononucleotide in LOV domain.

(b). Schematic illustration for the phosphorylation mechanism of PKD by LOV1 and LOV2 domains in *At*phot2. Taken from [87].

In 2008, Strickland et al. [89] and Lee et al. [90] supposed a concept of engineering light-induced allosteric control for functional protein, which includes the input domain and the output domain linked via Jα-helix. LOV2 domain from *Avena sativa* phot1 (AsLOV2), as the input part, can transduce light information to allosteric signals via the displacement of Jα-helix. The substrate binding site or catalytic site in functional protein as output domain is blocked by LOV2 domain under dark, whereas following the photoactivation and conformational change the active site will be exposed. Then the functional proteins, like TrpR [89], DHFR [90], Rac [91], and Caspase-7 [92] fused to the C-terminal of LOV2 domain, have been engineered genetically to be photoswitchable proteins. However, this photoactivatable model by direct fusion of entire protein domains is insufficient to regulate protein localization with subcellular spatial resolution. To solve this problem, three AsLOV2 domain-based light-induced dimerization systems are artificially designed: TULIPs, iLID and LOVTRAP.

TULIPs

Besides photoactivated-TrpR [89], Strickland et al. [93] also designed the tunable light-induced dimerization tags (TULIPs) to test optical controlled protein localization and function in HeLa cells and yeast. In this light-induced dimerization system, it contains two components: the ERBIN-derived engineered PDZ (ePDZ) that can be attached to many proteins of interest, and an ePDZ cognate peptide epitope fused to the C-terminal Jα-helix of AsLOV2. Under dark, the epitope is caged sterically resulting from the LOV-Jα interaction, whereas the unfolded Jα helix after photoactivation makes the epitope in the free state to bind with ePDZ domain. In addition, the mutational variants of ePDZ have been exploited that can tune the binding affinity to its cognate peptide from ~0.5 nM to >10 μM enabling this photoswitch tunable for further application [94].

iLID

The improved light-induced dimer (iLID) was designed by Guntas et al. [95] consisting of the AsLOV2-SsrA fused-protein and a domain of SspB. As blue light sensor of iLID, the conformation of AsLOV2 could be changed upon blue illumination, in which the

new covalent is formed between FMN and one conserved cysteine leading to the releasing of C-terminal Jα helix and the fused partner SsrA (AANDENY). SspB is a dimeric adaptor to tether SsrA-tagged proteins to ClpXP protease for degradation in prokaryotes [96]. Monomeric SspB is a compact domain consisting of a β sandwich and one α helix capped at N-terminal, and SsrA peptide binds in a hydrophobic groove formed by one edge of the β sandwich and some loops (Figure 1.6a). The interaction between the first eight residues of SsrA (AANDENYALAA) and SspB was presented in Fig 1.6b: residues 1-4 and 7-8 bind SspB specifically by hydrogen bonding and hydrophobic interactions, whereas residues 9-11 interacts with ClpXP protease [97]. In addition, SspB subunit has a folded domain in the N-terminal α helix to form the homodimer that is important for the ClpXP-based degradation system. McGinness et al. [98] first introduced eight mutations to the α helix, which changed hydrophobic residues to charged and polar residues and made the dimeric SspB to monomer.
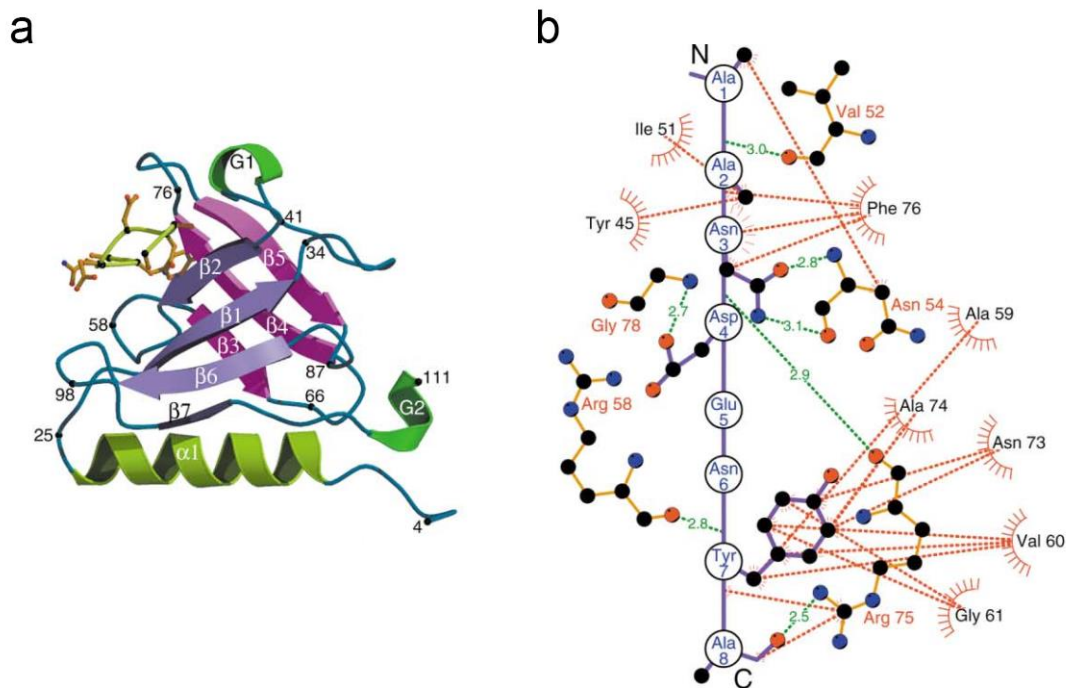

Figure 1.6 The SspB/SsrA Complex.

(a). Ribbon diagram showing the SspB/SsrA complex structure and the secondary structure elements of the SspB monomer. SsrA: yellow.

(b). Schematic diagram showing interactions between SspB and SsrA peptide. Hydrophobic interactions are denoted by red starbursts and dashed lines, hydrogen bonding interactions by the green dashed lines. Taken from [97].

The initial AsLOV2-SsrA design showed only 2-fold change in affinity from 31 nM to 57 nM when activated with light [99]. To stabilize the Jα helix and further decrease dark activity, some mutations were introduced to AsLOV2 as well as the extension of SsrA with single phenylalanine in C-terminal, which then named as improved AsLOV2-SsrA (iLID) in affinity from 132 nM to 4.7 μM when activated with light [95, 99]. Meanwhile, according to different binding affinity, SspB was classified to three categories: SspB_nano (wt), SspB_micro (R73Q, affinity for the iLID partner of 47 μM in the dark and 800 nM in the light) and SspB_milli (A58V/R73Q, affinity for the iLID partner of >1 mM in the dark and 56 μM in the light) [95, 100].

LOVTRAP

Different from TULIPs and iLID, LOVTRAP is a light-induced protein dissociation system: Z subunit from protein A (Zdk1) can bind with AsLOV2 under dark, but dissociate under blue light (dark versus light affinity: 26.2 ± 2.2 nM versus > 4 μM) [101]. Jα helix of AsLOV2 was inserted into a pocket formed by the first two helices of Zdk1, so that AsLOV2's C-terminal cannot link other proteins.

1.2.2.4 Vivid

Vivid (VVD) is a photoreceptor tuning blue-light responses and circadian clock via structure changes from monomer to a homodimer in *Neurospora crassa* [102, 103]. The 36-residue N-terminal truncation of VVD (VVD-36) is homologous to the LOV domain binding with FAD. Two components in VVD-36 are different from LOV domain: an unusual N-terminal cap region and a loop insertion that accommodates the FAD cofactor (Figure 1.7). After blue light illumination, VVD undergoes a photocycle similar to AsLOV2 (flavin ring broken, covalent formation between Cys and FAD and conformational change), which leads VVD-36 to form homodimer via the N-terminal cap [103]. Wang et al. [104] then fused VVD-36 to Gal4 to photo-regulate gene expression in HEK293 cells and mice. Furthermore, double mutant N56K and C71V were then designed, which decreased the dark activity. Another mutant VVD-I52C designed by Nihongaki et al. [105] further increases the homodimer-forming efficiency up to 180%. To improve the application of VVD as photoswitch, Kawano et al. [106] engineered the homodimer interface to develop two different VVD variants named Magnets. One VVD variant in the Magnet system contains positively charged amino acids (designated pMag), and the other VVD variant contains negatively charged amino

acids (designated nMag). These two variants only recognize each other by electrostatic that prevents the homodimer formation after photoexcitation.
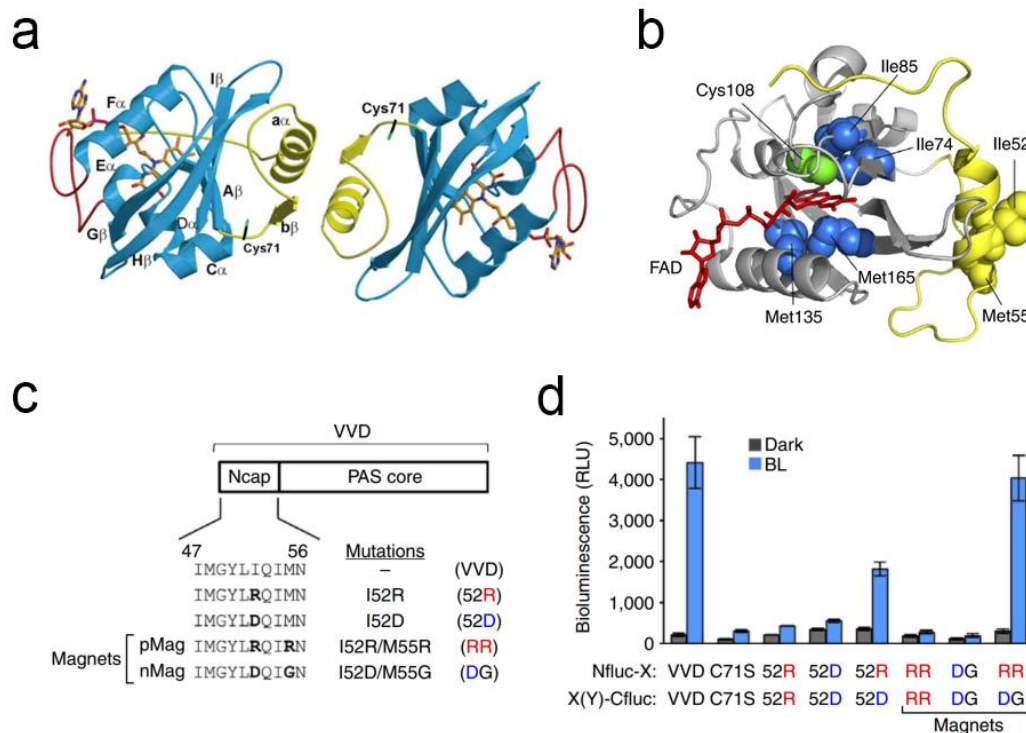
Figure 1.7 VVD structure and application.

(a). Crystallographic dimer of VVD-36, including the PAS core (blue), N-terminal cap (yellow), and FAD insertion loop (red).

(b). The monomer VVD structure and its key amino acid residues.

(c). Schematic representation of VVD domains and its variants.

(d). The assay of VVD dimerization before and after blue light irradiation. Modified from [103, 106].

1.3 Objectives of this study

In this study, I focus on characterizing and engineering optogenetic tools for new applications. The first is to construct and evaluate light-triggered water transport systems based on light-gated channels, including ChR2, *Gt*ACR1 and SthK-bPAC in *Xenopus* oocyte. This system can be used to regulate water transport easily by light with time and spatial precision, even mimic pathophysiological conditions like brain edema in animal models to conduct research on aquaporin function.

The second is to design a light-controlled protein purification system. I aim to develop an easy and flexible protein purification method based on the photo-induced protein interactive system iLID-SspB. In addition, SspB is optimized by point mutations to

inhibit homodimer formation and dark activity, which would further improve the efficiency of binding and dissociation for protein dimer to regulate protein translocation and function.

2 Material and methods

2.1 Molecular biology

2.1.1 DNA manipulation

Target DNA was synthesized by GeneArt Strings DNA Fragments (Life Technologies, Thermo Fisher Scientific) and amplified by Polymerase Chain Reaction (PCR). Phusion High-Fidelity DNA Polymerase (Life Technologies, Thermo Fisher Scientific) was used for PCR with the recipe in Table 2.1. The PCR program for Phusion DNA polymerase was shown in Table 2.2.

Table 2.1 PCR reaction mix

DNA template	1 μL (~20 ng)
HGD buffer	4.6 μL
Forward primer (10 μM)	1 μL
Reverse primer (10 μM)	1 μL
Enzyme	0.2 μL
dNTP	1 μL
ddH$_2$O	11.2 μL
Total	20 μL

Table 2.2 PCR program

Step	Repeat	Temperature	Time
step 1		98 ℃	45 s
step 2	6	98 ℃	15 s
		72 ℃	15 s per kb
step 3	6	98 ℃	15 s
		66 ℃	15 s
		72 ℃	15 s per kb
step 4	26	98 ℃	15 s
		56 ℃	15 s
		72 ℃	15 s per kb
step 5		72 ℃	2 min
		4 ℃	store

The PCR products were mixed with the 6x DNA loading buffer (Table 2.3) for DNA agarose gel electrophoresis and then purified by QIAquick gel Extraction Kit (Qiagen, Hilden, Germany). The purified DNA sample was digested by restriction enzymes to

generate fragments for DNA ligation by T4 DNA ligase (Fermentas, Thermo Fisher Scientific, Waltham, USA). The molar ratio of DNA fragment to vector ranges from 2:1 to 10:1.

Table 2.3 6x DNA loading buffer

Bromophenol blue	0.25%
Glycerol	30%
Store	4 °C

2.1.2 Site-directed mutagenesis

Point mutations were introduced by QuikChange PCR. The primer pairs contained single or multiple basic substitutions to change amino acids. The PCR product was digested by the enzyme of DpnI for 2 hours at 37 °C to remove the template.

2.1.3 Competent cell preparation and transformation

E. coli MRF was first cultured in autoclaved LB medium (Table 2.4) overnight at 37 °C, 220 rpm in a rotary shaker. 1 mL cultures were then inoculated to 100 mL fresh LB medium with same culture condition. When the OD_{600} reached ~0.6, the cell was centrifuged at 4000 rpm, 4 °C for 5 min and resuspended by pre-cooled (on ice) 0.1 M $CaCl_2$. The cell was put on ice for 30 min to form the competent cell. The above obtained DNA products were gently mixed with the competent cell on ice for ~20min, and then transferred to 42 °C for 90 s. Before plating on the LB agar plate (Table 2.4) with appropriate antibiotics (Table 2.5), the competent cell was recovered on ice for 5 min. The plate was put in the 37 °C incubator overnight.

Table 2.4 LB medium recipe

Tryptone	10 g
Yeast extract	5 g
NaCl	5 g
Agar	15 g (only for plate)
Add water to 1 L	

Table 2.5 Antibiotic concentration

Antibiotic	Stock solution	Final concentration

Ampicillin	50 mg/mL in water	50 µg/mL
Kanamycin	50 mg/mL in water	50 µg/mL

2.1.4 *E. coli* cracking and amplification

The colonies from the transformed *E. coli* were selected to mix with the cracking buffer (Table 2.6) for 10 min. The lysed mixtures were checked in DNA gel. Two or three colonies with correct supercoiled plasmid size were inoculated to 6mL LB medium with antibiotic overnight at 37 ℃ for the plasmid extraction next day.

Table 2.6 2x Cracking buffer

NaOH	0.2 N
SDS	0.5%
Sucrose	20%

2.1.5 Plasmid extraction and sequencing

Plasmid extraction was performed by Qiaprep spin miniprep kit (Qiagen, Hilden, Germany). 6 mL overnight culture was centrifuged at 5000 rpm for 5 min and extracted according to the protocol. The plasmid was eluted by H_2O, and the concentration was measured by a nano photometer (NanoPhotometer^{TM}, Implen, Munic, Germany) at the absorption of 260 nm. The plasmid was then sent to GATC Biotech (GATC Biotech, Constance, Germany) for sequencing.

2.1.6 RNA preparation

The plasmid was first digested by the enzyme of NheI for 2 hours at 37 ℃ to form linearized plasmid DNA. The AmpliCap-MaxT7 High Yield Message Maker Kit (Epicentre Biotechnologies) was used to transcribe the linearized DNA to cRNA as shown in Table 2.7. The 10 µL mixture was then incubated at 37 ℃ for 3 h. 5 M Ammonium acetate (10 µL) was added to the mixture and frozen at -20 ℃ for 30 min. The mixture was then centrifuged at 4 ℃, 30000 rpm for 30 min. The supernatant was discarded. The pellet (cRNA) was washed by 50 µL 70% ethanol and dried to become transparent. 15 µL RNasefree H_2O was added to dissolve the cRNA. The concentration was measured by a nano photometer (NanoPhotometerTM, Implen, Munic, Germany). The cRNA were then stored at -20 ℃ for further use.

Table 2.7 *In vitro* transcription

Reagent	Amount
Linearized DNA product	2.7 μL (600 ng)
AmpliCap-Max™ Cap/NTP PreMix	4 μL
100 mM Dithiothreitol (DTT)	1 μL
10×AmpliCap-Max™ T7 Transcription Buffer	1 μL
AmpliCap-Max™ T7 Enzyme (5 U/μL)	1 μL
RNase Inhibitor (20 U/μL)	0.3 μL

2.2 *Xenopus laevis* oocyte

2.2.1 Oocyte preparation

The oocytes from *Xenopus laevis* were digested with 5 mg/mL collagenase for 1.5 h. After digestion, the oocytes were washed by ND96 (Table 2.8). The obtained oocytes were transferred into a dish incubated at 16 °C before cRNA injection.

Table 2.8 ND96 buffer

NaCl	96 mM
KCl	2 mM
$MgCl_2$	1 mM
$CaCl_2$	1 mM
Hepes	5 mM
Adjust pH to 7.6	

2.2.2 RNA injection

cRNA was injected into oocytes by the nano injection machine (NanojectIII, Drummond Scientific Company). The injection capillary (3.511 Drummond #3-000-203-G/X; Drummond Scientific Company) was made by a vertical Puller (PP-83, Narishige). The injected oocytes were cultured in ND96 buffer at 16 °C with (for rhodopsin constructs) or without (for non-rhodopsin constructs) additional 10 μM ATR.

2.2.3 Shrinking and swelling observation in oocyte

The oocytes expressed channels were tested in different buffers including ND96, NMG-Asp (Table 2.9), and high K^+ buffer (Table 2.10) under blue light (Figure 2.1a). If the outside osmolarity is smaller than oocyte inside osmolarity, water will go inside the

oocyte increasing oocyte volume as swelling (Figure 2.1b). On the other hand, water in the oocyte will go outside decreasing oocyte volume as shrinking (Figure 2.1b).
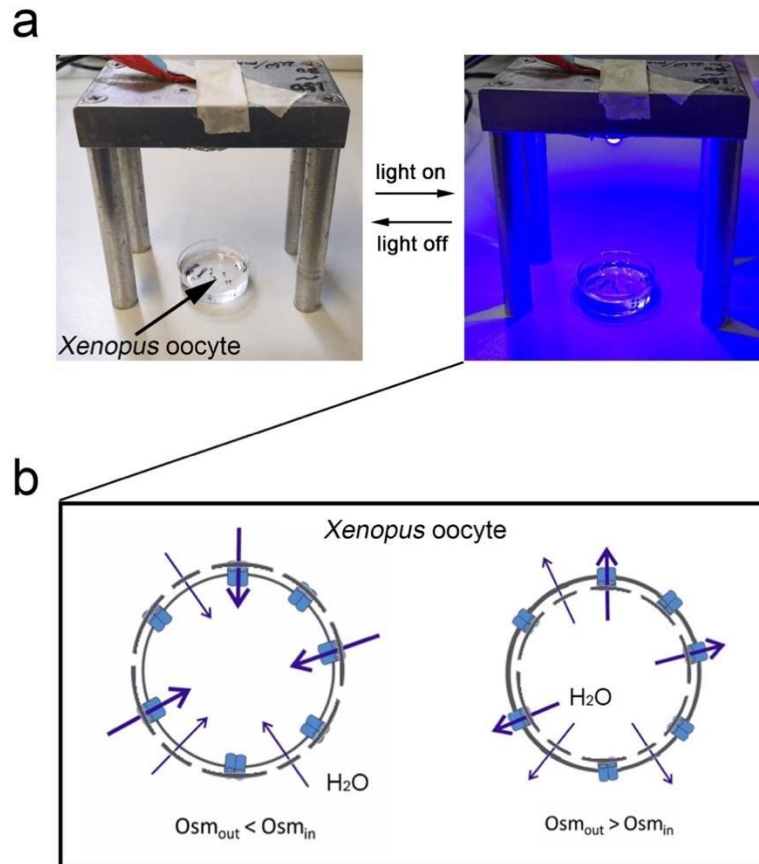
Figure 2.1 Condition for oocyte swelling and shrinking.

(a). LED (470 nm, 100 μW/mm^2).

(b). *Xenopus* oocyte swells in the hypotonic solution and shrinks in the hypertonic solution.

Table 2.9 NMG-Aspartate buffer

NMG	115 mM
MgCl$_2$	1 mM
Hepes	5 mM
Adjust pH to 7.6 with DL-Aspartate	

Table 2.10 High K$^+$ buffer

KCl	100 mM
MgCl$_2$	10 mM
Hepes	5 mM
Adjust pH to 7.6	

2.2.4 Soluble fraction/membrane fraction extraction and reaction *in vitro*

Soluble fraction: the oocytes expressing soluble protein (YFP-SspB) were pooled and washed three times by 300 µL buffer A (Table 2.11). After being gently homogenized by pipette, the lysed mixture was centrifuged at 30000 rpm, 4 °C for 15 min. The sediment was discarded. The supernatant was then transferred to a fresh tube for further use.

Membrane fraction: 25 oocytes expressing membrane protein (Lyn-iLID) were pooled and washed three times by 300 µL buffer A. After gently homogenized by pipette, the lysed mixture was centrifuged at 500 rpm for 5 min. The sediment was discarded. The supernatant was transferred to a fresh tube and centrifuged at 30000 rpm, 4 °C for 2 min. The sediment containing membrane fraction was resuspended and washed three times by buffer A for further use.

Binding: the soluble fraction containing YFP-SspB and the membrane fraction containing Lyn-iLID were mixed in one tube with 300 µL buffer A (Figure 2.2). The mixture was under blue light (470 nm, 100 µW/mm^2) or dark as control to stimulate the binding of light-induced dimer iLID-SspB. After stimulation, the mixture was centrifuged at 30000 rpm, 4 °C for 1 min to separate the membrane fraction and unbonded soluble fraction. The supernatant was transferred to a fresh tube and the rest concentration of YFP-SspB was measured according to fluorescence emission. The sediment was resuspended by 300 µL buffer A and washed three times. The precipitated YFP-SspB by membrane fraction was also measured according to fluorescence emission.

Release: the resuspended membrane fraction in 300 µL buffer A binding with YFP-SspB was transferred to dark. The affinity between iLID and SspB decreased under dark that contributed to the release of YFP-SspB from membrane fraction (Figure 2.2). After centrifugation at 30000 rpm, 4 °C for 10 min, the sediment was resuspended by 300 µL buffer and washed three times. The rest fluorescence in membrane fraction was measured.
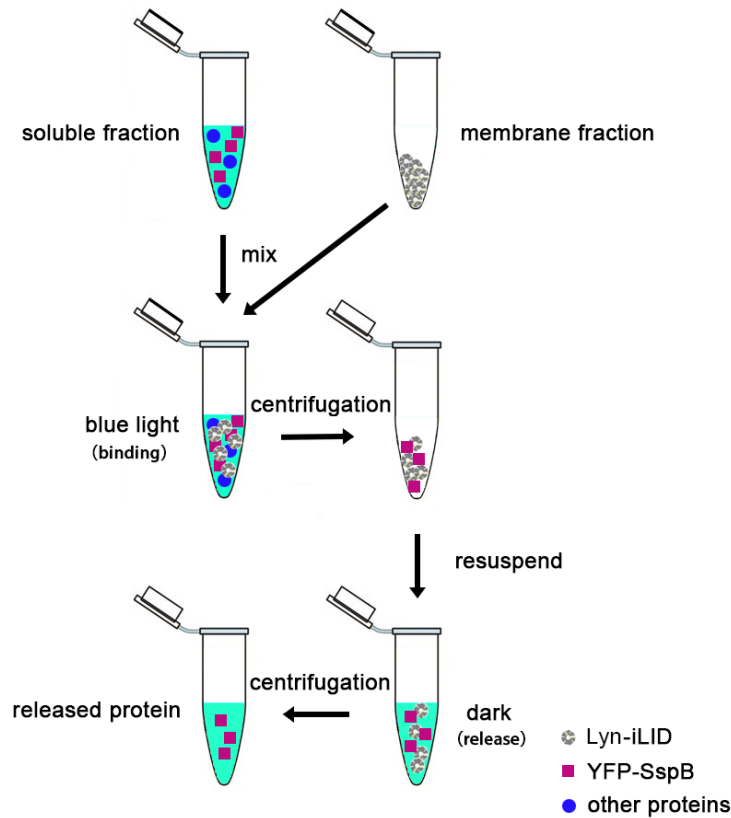
Figure 2.2 Light-controlled protein reaction between soluble fraction and membrane fraction.
YFP was fused to the N-terminal of SspB, expressed as soluble fraction in *Xenopus* oocyte. iLID
was fused to the C-terminal of Lyn, expressed as membrane fraction in *Xenopus* oocyte. These two
parts were mixed under blue light for the binding between iLID and SspB. After washing and
removing unspecific bounded proteins via centrifugation (30000 rpm, 4 °C), the iLID and YFP-
SspB complex was moved into dark for release.

Table 2.11 Buffer A

Tris-HCl	75 mM
NaCl	100 mM
MgCl$_2$	2 mM
DTT	5 mM
Adjust pH to 7.6	

2.3 Protein quantification by fluorescence

To quantitate the binding and releasing efficiency, we used the relative fluorescence
units (RFU) to analyze the amount of YFP-tagged protein. Purified YFP protein
standard (RayBiotech, 10 μg) was diluted to 2500 ng/mL in buffer A to calibrate the

fluorometer. Fluorescence emission was measured at the range of 510-580 nm using the QuantusTM Fluorometer (Promega) with 495 nm excitation.

2.4 Electrophysiology

Two-electrode voltage clamp (TEVC) was used to measure photocurrent from *Xenopus* oocyte expressing target proteins. One oocyte in a small chamber with the flowing buffer was shown in Figure 2.3. The potential electrode (UE) and current electrode (IE) were injected into the oocyte. The oocyte membrane potential U_m was recorded by the difference between UE and U_{ref}. The current injected to the oocyte by the setup to maintain the command potential corresponds to the current across the oocyte membrane. TURBO TEC-05 system (npi electronic GmbH, Tamm, Germany) was used in this study.
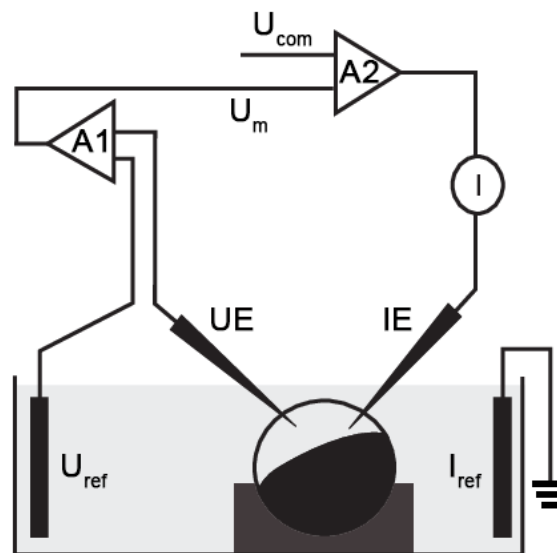
Figure 2.3 Two electrode voltage-clamp (TEVC) with *Xenopus* Oocyte.

One oocyte in the chamber was injected by potential electrode (UE) and current electrode (IE). Two reference electrodes for potential (U_{ref}) and current (I_{ref}) were connected to the buffer solution. U_m refers to the membrane potential of the oocyte. U_{com} refers to the command potential inputted by the computer program. A1 and A2 refer to the potential amplifier and feedback amplifier.

2.5 cAMP ELISA assay

Oocytes injected with bPAC were incubated at 16 °C for three days in ND96. 10 oocytes for each group were pooled and homogenized by pipetting in 100 μL buffer A with 1x Protease Inhibitor Cocktail (Roche). The lysed mixture was centrifuged at 30000 rpm, 4 °C for 10 min. The supernatant was transferred to a fresh tube as soluble

extract and dialyzed by an ultra-centrifugal filter tube to remove endogenous ATP/cAMP. 10 μL soluble extract as one oocyte was mixed with 1 mM ATP and illuminated by blue light (473nm, 0.3 mW/mm^2) at different time points (1min and 5min). cAMP was quantified by using DetectX High Sensitivity Direct Cyclic AMP Chemiluminescent Immunoassay Kit (Arbor Assays).

2.6 Protein expression and manipulation

2.6.1 Protein expression in *E. coli*

pET28b-YFP-SspB and pET28b-H1021-iLID were introduced into *E. coli* BL21(DE3). Single colonies were pre-cultured in 5 mL LB media with 50 μg/mL kanamycin overnight at 37 °C. Then 1 mL LB media was inoculated into 100 mL fresh LB media and cultured around 4 h at 37 °C reaching an OD_{600} value of ~0.6. 0.5 mM isopropyl-β-D-thiogalactopyranoside (IPTG) was added into LB media to induce protein expression and the temperature was changed to 28 °C for overnight growth.

2.6.2 Soluble fraction and membrane fraction preparation

Soluble fraction: 50 mL of the culture expressing YFP-SspB were harvested by centrifugation at 5000 rpm for 5 min, resuspended by 1mL buffer A (SspB tagged DNA polymerase was resuspended by 1mL buffer B (Table 2.12)), and washed three times. The cells were homogenized by ultrasonic processor UP50H for 10 min on ice. The lysed mixture was centrifuged at 30000 rpm for 30 min, and the supernatant was transferred to a fresh tube for further use (Figure 2.4).

Membrane fraction: 50 mL of the culture expressing H1021-iLID were harvested by centrifugation at 5000 rpm for 5 min, resuspended by 1mL buffer A, and washed three times. The cells were homogenized by ultrasonic processor UP50H for 20 min on ice. The lysed mixture was centrifuged at low speed (2000 rpm, 2 min). The supernatant was transferred to a fresh tube and centrifuged at high-speed (10000 rpm, 1 min). After second time centrifugation, the supernatant was discarded, but the sediment was resuspended by 200 μL buffer A and washed three times for further use (Figure 2.4).
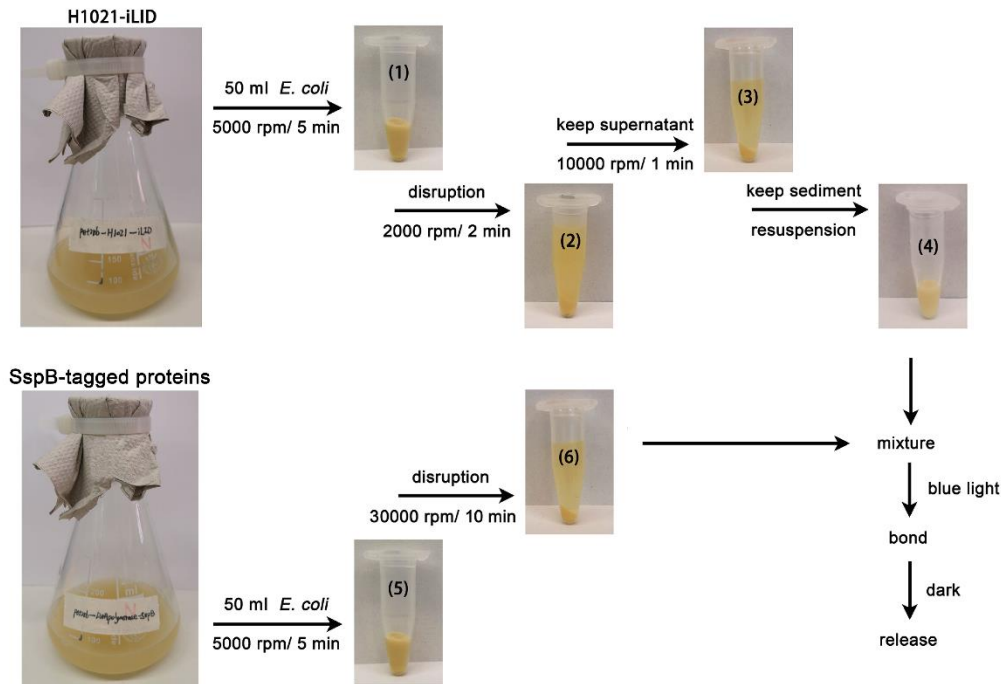
Figure 2.4 The process for sample preparation and reaction.

Samples were harvested from 50 mL culture. Membrane fraction was collected by two-step centrifugation from cell lysate. The first low-speed (2000 rpm, 2min) centrifugation was used to centrifuge down cell debris. The second high-speed (10000 rpm, 1 min) centrifugation was used to centrifuge down membrane fraction (1-4). Soluble fraction was collected by high-speed centrifugation (30000 rpm, 10 min) from cell lysate (5-6).

Table 2.12 Buffer B

Tris-HCl	75 mM
KCl	300 mM
$MgCl_2$	2 mM
DTT	5 mM
Adjust pH to 7.6	

2.6.3 Protein binding and releasing

Soluble fraction containing YFP-SspB and membrane fraction containing H1021-iLID were mixed in one tube with buffer A (Figure 2.4). The mixture was under blue light (470 nm, 100 uW/mm^2) or dark as control to stimulate the binding of light-induced dimer iLID-SspB. After stimulation, the mixture was centrifuged at 10000 rpm for 1 min to separate the membrane fraction and soluble fraction. The supernatant was discarded. The sediment was resuspended by 300 μL buffer A and washed three times.

The precipitated YFP-SspB by membrane fraction was measured according to fluorescence emission. In addition, the resuspended membrane fraction was transferred to dark. The affinity between iLID and SspB decreased under dark that contributed to the release of YFP-SspB from membrane fraction. After centrifugation at 30000 rpm, 4 °C for 30 min, the supernatant was transferred to a fresh tube, and the fluorescence emission was measured to calculate protein purification efficiency.

2.6.4 SDS-PAGE

Protein samples were analyzed by Sodium Dodecyl Sulfate Polyacrylamide Gel Electrophoresis (SDS-PAGE) performed in an electrophoresis system. SDS polyacrylamide gels were prepared according to the system instructions including stacking gel (Table 2.13) and separating gel (Table 2.14). Protein samples were prepared by mixing 2x SDS sample buffer (Table 2.15), and then denatured at 98 °C for 10 min. After loading into the gel, electrophoresis was carried out at 80 V when protein samples were running in stacking gel, and changed to 120 V when protein samples were arrived at separating gel with running buffer (Table 2.16). By comparison with a pre-stained protein molecular weight marker (Life Technologies, Thermo Fisher Scientific), the molecular weight of the target protein was estimated.

Table 2.13 Stacking gel (3.2%)

Components	Amount
4xTris-HCl/SDS, pH 6.8 (0.5 M Tris, 0.4% SDS)	1.25 mL
H_2O	3.3 mL
40% Acrylamide	0.4 mL
10% APS	50 μL
TEMED	5 μL

Table 2.14 Separating gel (10%)

Components	Amount
4xTris-HCl/SDS, pH 8.8 (1.5 M Tris, 0.4% SDS)	2.5 mL
H_2O	4.9 mL
40% Acrylamide	2.5 mL
10% APS	50 μL
TEMED	5 μL

Table 2.15 2x SDS Sample buffer

Components	Amount
SDS	4%
Tris-HCl, pH 6.8	0.5 M
Glycerol	20%
Bromophenol blue	0.004%
DTT	10%

Table 2.16 1xRunning buffer

Components	Amount
SDS	0.1%
Tris	25 mM
Glycine	190 mM

2.6.5 Native PAGE

Protein samples were analyzed by native polyacrylamide gel electrophoresis (native PAGE) performed in an electrophoresis system. Native polyacrylamide gels were prepared according to the system instructions including stacking gel (Table 2.17) and separating gel (Table 2.18). Protein samples were prepared by mixing 2x sample buffer (Table 2.19). As shown in Fig 2.5, protein samples carrying different charges could move to different polars in the gel. After loading, electrophoresis was carried out at 80 V in both stacking gel and separating gel with running buffer (Table 2.20). By comparison with a standard protein BSA, the molecular weight of the target protein was estimated.
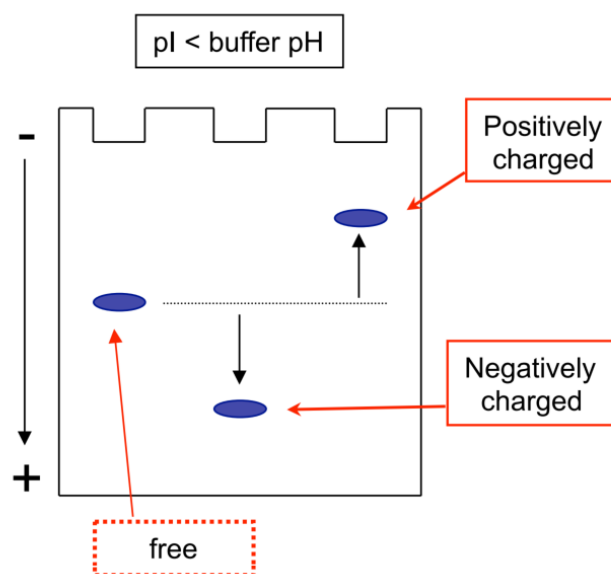
Figure 2.5 Schematic of native PAGE.

The electrophoresis direction setting depends on the charge that the protein carried. The charge was regulated by the sample buffer according to isoelectric point (pI) of the protein.

Table 2.17 Stacking gel (3.2%)

Components	Amount
4xTris-HCl/SDS, pH 6.8 (0.5M Tris)	1.25 mL
H_2O	3.3 mL
40% Acrylamide	0.4 mL
10% APS	50 μL
TEMED	5 μL

Table 2.18 Separating gel (10%)

Components	Amount
4xTris-HCl/SDS, pH 8.8 (1.5M Tris)	2.5 mL
H_2O	4.9 mL
40% Acrylamide	2.5 mL
10% APS	50 μL
TEMED	5 μL

Table 2.19 2x Sample buffer

Components	Amount

Tris-HCl, pH 6.8	0.5 M
Glycerol	20%
Bromophenol blue	0.004%

Table 2.20 1xRunning buffer

Components	Amount
Tris	25 mM
Glycine	190 mM

2.6.6 Protein staining

EZBlue (Sigma) was used for the unspecific staining of proteins and allowed the visualization of protein bands in both SDS-PAGE gel and native PAGE gel. After finishing electrophoresis, gels were incubated in EZBlue for 30 min on a rocker and then washed by water directly.

2.6.7 Western Blot

The protein samples were subjected to 10% SDS–PAGE and transferred into PVDF membranes (Millipore, USA), which should be activated by methanol and then soaked in the transfer buffer (Table 2.21). Membranes carrying proteins were blocked in Tris-buffered Saline with Tween 20 (TBST) (Table 2.22) containing 5% BSA for 0.5 h and subsequently incubated overnight at 4 °C with diluted primary antibodies against YFP with HRP conjugation (1:2000 dilution, Invitrogen). The band was washed by TBST and incubated in ECL solution (Thermo Fisher Scientific) for 1 min. For imaging, the Odyssey Fc Imaging System from LI-COR Biosciences was used.

Table 2.21 Transfer buffer

Components	Amount
Tris	25 mM
Glycine	190 mM
Methanol	20%

Table 2.22 Tris-buffered Saline with Tween 20 (TBST)

Components	Amount

Tris-HCl pH 7.5	20 mM
NaCl	150 mM
Tween 20	0.2%

2.7 Statistical analysis

Results are presented as mean ± standard error of the mean (SEM) via GraphPad Prism software (San Diego, CA, USA).

3 Results

3.1 light-triggered water transport

3.1.1 Photocurrent of ChR2 and *Gt*ACR1 in *Xenopus* oocyte

Passive water transport across the plasma membrane of cells responds to the osmotic gradient formed by the movement of solutes. Na^+ concentration in *Xenopus* oocyte cytoplasm is ~10 mM, and Cl^- concentration is ~50 mM [107]. To create osmotic gradients by changing ion concentration, the light-gated cation channel ChR2-XXM was expressed in *Xenopus* oocyte, from which Na^+ influx could be tested in ND96 buffer by blue light illumination. We hypothesized that via Na^+ influx formation by ChR2-XXM, the membrane potential from oocytes could become more positive, creating the electrochemical driving force to facilitate the movement of anions. Then if the light-gated anion channel *Gt*ACR1 is also expressed in oocytes, it will further accelerate osmotic gradient formation based on Cl^- influx. Testing if ChR2-XXM and *Gt*ACR1 could cooperate in oocytes, TEVC recording under different voltages was performed. From the current-voltage relationship, *Xenopus* oocytes expressing *Gt*ACR1 or co-expressing ChR2-XXM and *Gt*ACR1 have the same reversal potential, ~-20 mV, two days post injection (dpi) (Figure 3.1a and b). For the closing pattern, oocytes co-expressing ChR2-XXM and *Gt*ACR1 were slower than oocytes expressing *Gt*ACR1, but were similar to oocytes expressing ChR2-XXM. These two characters indicated that ChR2-XXM and *Gt*ACR1 could be expressed and cooperate in oocytes very well.
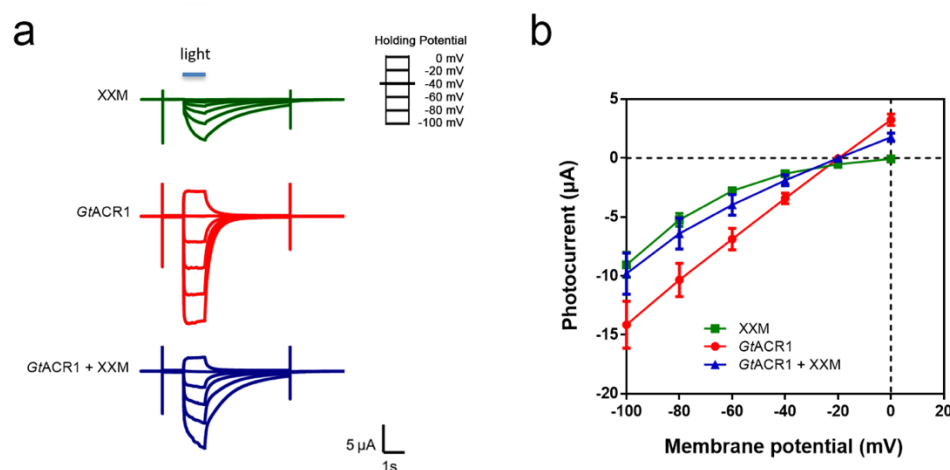

Figure 3.1 Co-expression of ChR2-XXM and *Gt*ACR1 in *Xenopus* oocyte.
(a). 30 ng ChR2-XXM or 5 ng *Gt*ACR1 by single cRNA injection or mixture injection to oocytes were expressed for two days. Photocurrents were measured 2 dpi in ND96 buffer (96 mM NaCl, 2

mM KCl, 1 mM MgCl$_2$, 5 mM Hepes, pH 7.6) under 1 s blue illumination. A 473 nm laser at 3 mW/mm^2 was used here. The holding potential was changed from -100 to 0 mV.

(b). The current-voltage relationship was concluded from 6 oocytes in each group.

A new variant of ChR2-XXM2.0 was designed in our lab, which has a higher photocurrent than ChR2-XXM. The oocyte co-expressing ChR2-XXM2.0 and *Gt*ACR1 exhibited much higher inward photocurrent than the oocyte co-expressing ChR2-XXM and *Gt*ACR1 (Figure 3.2a and b). I then chose ChR2-XXM2.0 cooperating with *Gt*ACR1 to induce the osmotic gradient.
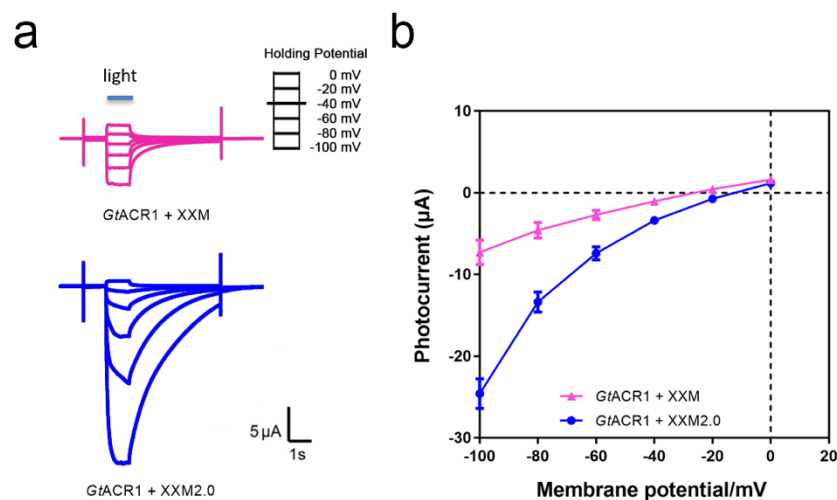

Figure 3.2 Photocurrent comparison of different ChR2-XXM variants.

(a). 30 ng cRNA of ChR2-XXM or XXM2.0 with 10 ng cRNA of *Gt*ACR1 were injected for oocytes expression. Photocurrents were measured 2 dpi in ND96 buffer under 1 s blue illumination. A 473 nm laser at 3 mW/mm^2 was used. The holding potential was changed from -100 to 0 mV.

(b). The current-voltage relationship was concluded from 6 oocytes in each group.

3.1.2 Expression of AQP1 in *Xenopus* oocyte

Typically, if the external osmolarity is higher than oocyte cytoplasm osmolarity, *Xenopus* oocyte will shrink due to water loss, and then the separation between the cytoplasm membrane and vitelline membrane can be observed by a microscope. On the other hand, if the external osmolarity is lower than oocyte cytoplasm osmolarity, oocytes will swell due to water uptake, and large amounts of water uptake can speedily increase the oocyte volume until the cell membrane rupture. However, when the oocyte was transferred into the hypertonic solution（2x ND96 buffer), it was not easy to observe morphological change after 2 min by only simple water diffusion (Figure 3.3a).

Meanwhile, in the hypotonic buffer (only water), the oocyte was stable without volume change after 1 min due to protection from the vitelline membrane (Figure 3.3b). To accelerate water transport based on osmotic gradient, mammalian AQP1 was expressed in *Xenopus* oocyte. The AQP1 expressing oocytes were also tested in 2x ND96 buffer and water, respectively. The morphological change of the oocyte was recorded under different time points. In the 2x ND96 buffer, the cell membrane was significantly separated from the vitelline membrane after 40 s from the AQP1 expressing oocyte (Figure 3.3a). In addition, the AQP1 expressing oocyte significantly exploded after 40 s in water (Figure 3.3b). Therefore, AQP1 could be co-expressed with optogenetic tools to test light-triggered water transport.
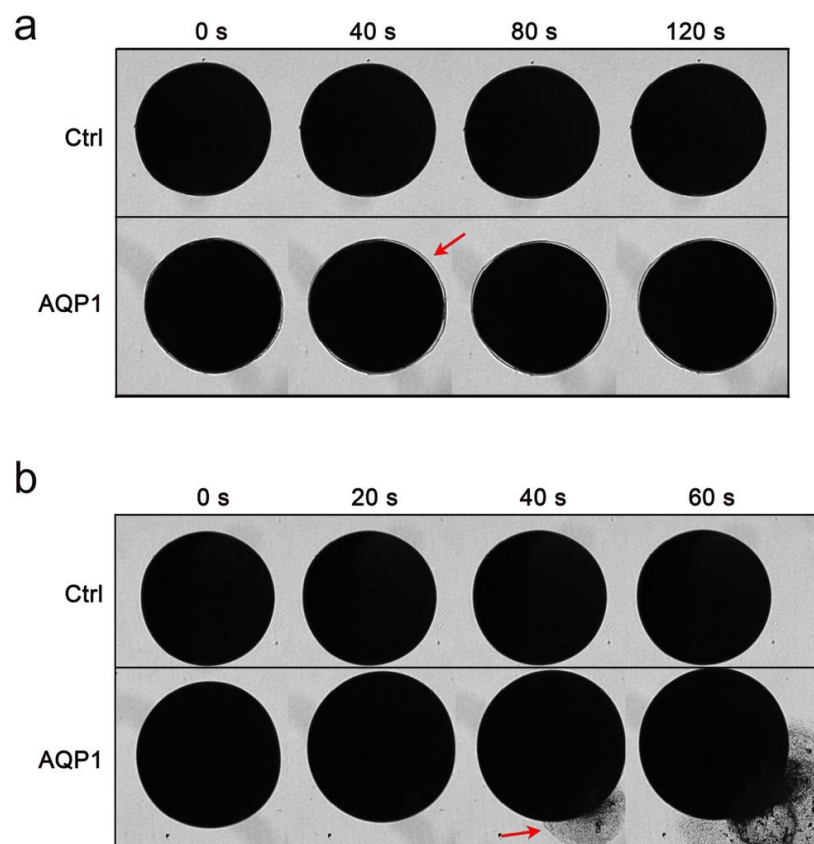

Figure 3.3 The AQP1 expressing oocyte in hypertonic or hypotonic buffer.

5 ng cRNA of AQP1 were injected for oocyte expression in ND96 buffer. For control, the oocyte was injected with water. The oocytes were measured 2 dpi in the hypertonic buffer (2x ND96) (a) or the hypotonic buffer (water) (b), respectively. The morphological change was recorded at different time points by microscope. Red arrow: the separated part between the cytoplasm membrane and vitelline membrane or the explosive part from the oocyte.

3.1.3 Oocyte swelling in ND96 buffer via Na$^+$/Cl$^-$ influx

To mimic physiological conditions, ND96 buffer was used for water transport efficiency testing. Since the AQP1 expressing oocyte is sensitive to the osmotic gradient, ND96 buffer should be ensured as an isotonic condition not triggering water transport through oocytes. As shown in Figure 3.4, the AQP1 expressing oocyte was stable in ND96 buffer without shrinking or swelling after 10 min, indicating that oocyte cytoplasm osmolarity is close to ND96 buffer, ~210 mOsm/kg [108]. However, if the concentration of ND96 buffer decreased to 0.9x (hypotonic condition) or increased to 2.0x (hypertonic condition), swelling or shrinking can be observed from the AQP1 expressing oocytes (Figure 3.4).
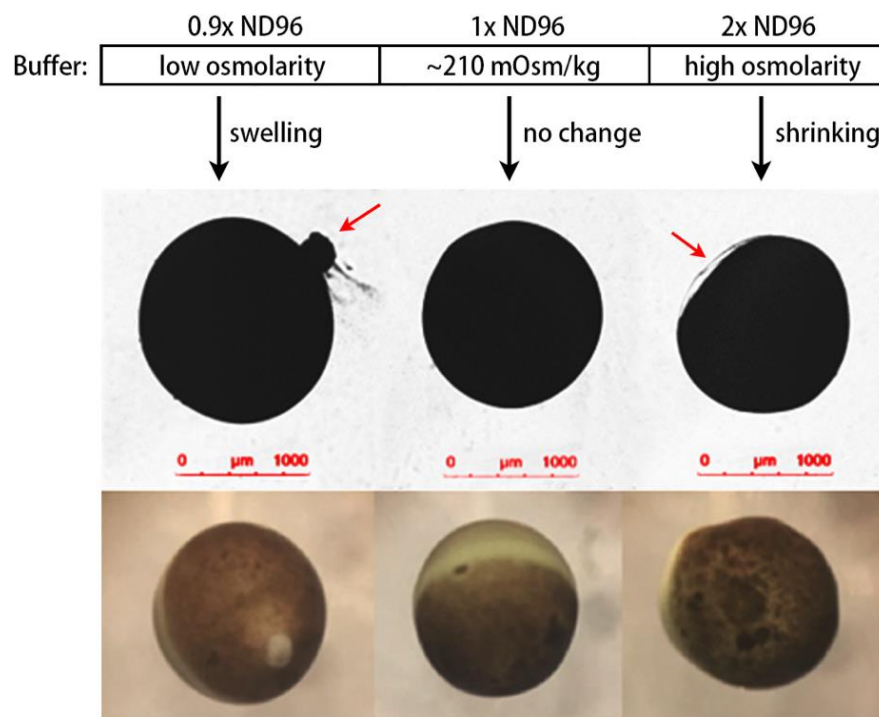

Figure 3.4 *Xenopus* oocyte expressing AQP1 in different concentrations of ND96.
5 ng cRNA of AQP1 were injected for oocyte expression in ND96 buffer. The oocyte morphological changes were compared 2 dpi in different concentrations of ND96 buffers: 0.9x, 1x and 2x. The images were taken after 10 min. Red arrow: the separated part between the cytoplasm membrane and vitelline membrane or the explosive part from oocytes.

As ND96 buffer was isotonic for oocyte, we then compared water uptake efficiency based on ion influx production from the oocytes expressing (1) AQP1, (2) AQP1 and ChR2-XXM2.0, (3) AQP1 and *Gt*ACR1, (4) AQP1, ChR2-XXM2.0 and *Gt*ACR1, (5) ChR2-XXM2.0, (6) *Gt*ACR1, and (7) ChR2-XXM2.0 and *Gt*ACR1. After 20 min blue

illumination, the oocyte cytoplasm leaked out in the group (4) due to large amounts of water uptake and pressure release (Figure 3.5), indicating that water transport efficiency was the highest from oocytes co-expressing AQP1, ChR2-XXM2.0 and GtACR1. This phenomenon results from two conditions: (1) the formation of osmotic gradient between oocyte cytoplasm and extracellular condition; (2) water fast transport through the cell membrane. From group (4), ChR2-XXM2.0 and GtACR1 could efficiently create the osmotic gradient due to the influx of Na^+/Cl^-, and then AQP1 sensed osmotic gradient and accelerated water transport. However, without a sizeable osmotic gradient or AQP1, the swelling oocyte cannot be observed in a short time from other groups.
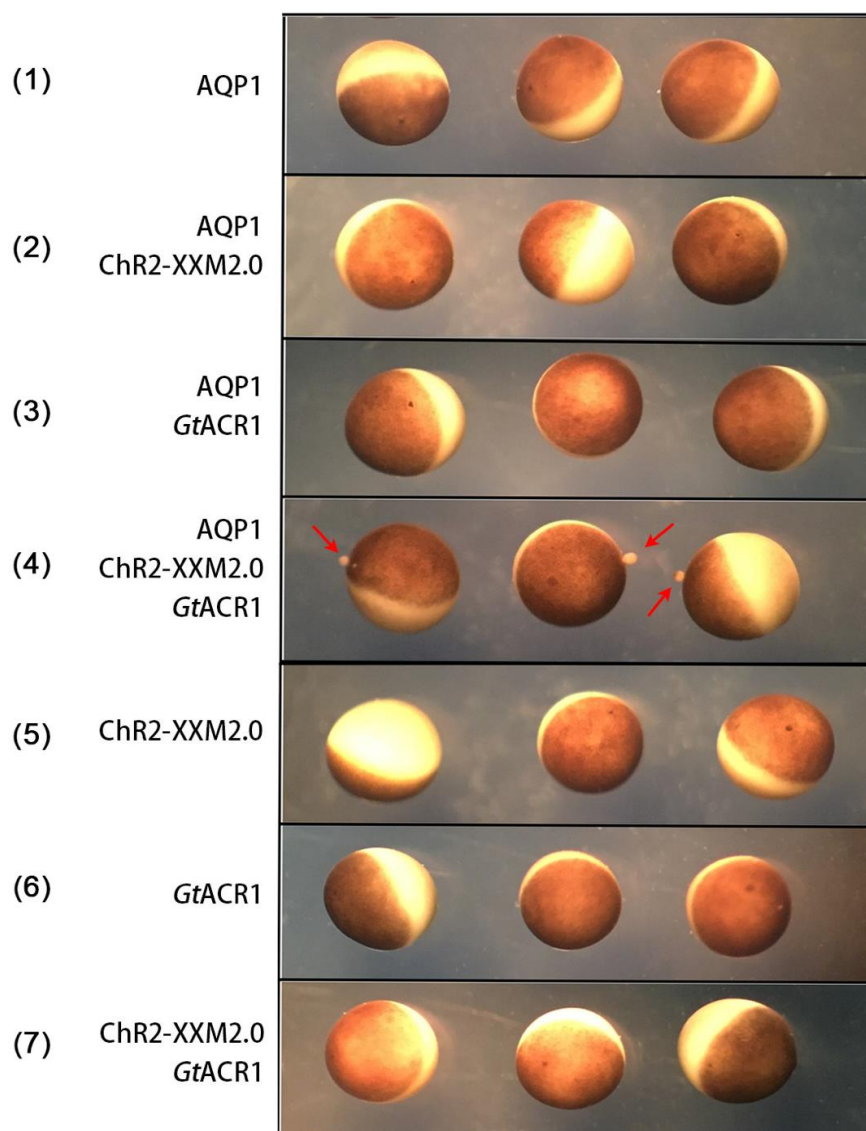

Figure 3.5 Light-induced oocyte swelling in ND96 buffer after expressing different combinations of proteins.

The oocytes injected with different cRNAs (1) AQP1, (2) AQP1 and ChR2-XXM2.0, (3) AQP1 and *Gt*ACR1, (4) AQP1, ChR2-XXM2.0 and *Gt*ACR1, (5) ChR2-XXM2.0, (6) *Gt*ACR1, and (7) ChR2-XXM2.0 and *Gt*ACR1, were tested 2 dpi in ND96 buffer for swelling efficiency according to the oocyte morphological changes. Before taking images, the oocytes were stimulated by 20 min blue illumination (LED: 470 nm, 100 μW/mm^2). Red arrow: the explosive part in the oocyte. cRNA amount: 5 ng AQP1, 30 ng ChR2-XXM2.0, 10 ng *Gt*ACR1.

3.1.4 Oocyte shrinking in NMG-Asp buffer via Na$^+$/Cl$^-$ efflux

To further confirm the practicability of the light-triggered water transport via ChR2-XXM2.0 and *Gt*ACR1, I selected NMG-Asp buffer without Na$^+$ to check whether the oocyte could shrink or not due to ion efflux. The AQP1 expressing oocyte began to shrink slightly after 10 min in NMG-Asp buffer, which is a hypertonic buffer and not appropriate for water transport testing (Figure 3.6). Therefore, the concentration of NMG-Asp buffer was diluted to 0.9x, 0.8x and 0.7x. After 10 min maintaining in different buffers, the AQP1 expressing oocyte was stable in 0.9x NMG-Asp buffer, but exploded in 0.8x and 0.7x NMG-Asp buffer, suggesting that the osmolarity of 0.9x NMG-Asp buffer is close to 210 mOsm/kg as an isotonic condition that could be used to test light-triggered water transport efficiency (Figure 3.6).
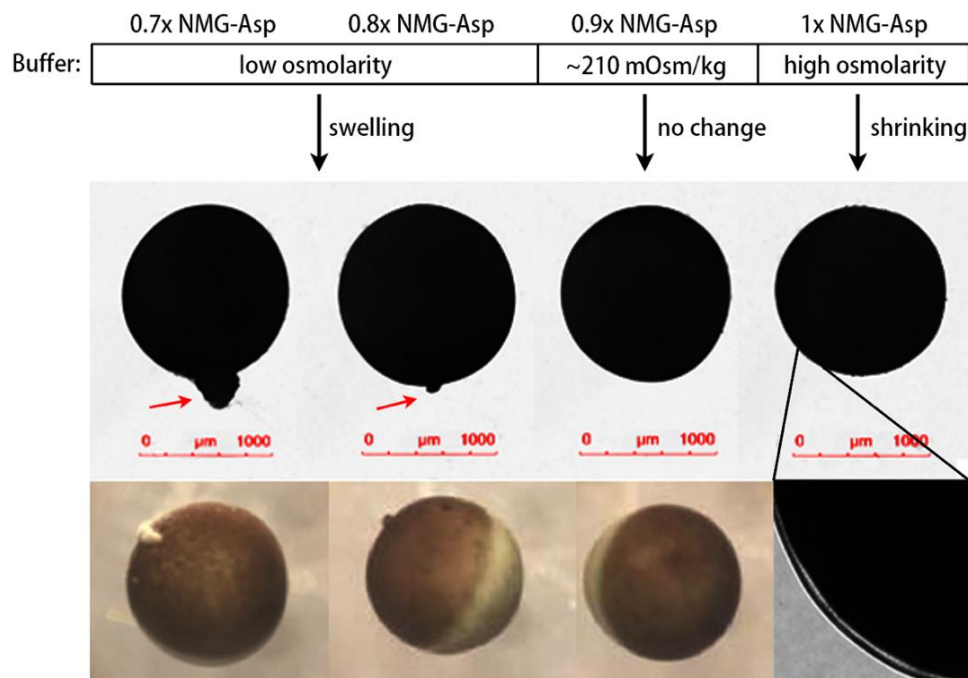

Figure 3.6 *Xenopus* oocyte expressing AQP1 in different NMG-Asp buffer.

5 ng cRNA of AQP1 were injected for oocyte expression. Water transport efficiency according to the oocyte morphological changes was compared 2 dpi in different concentrations of NMG-Asp

buffers: 0.7x, 0.8x, 0.9x and 1x. The images were taken after 10 min. Red arrow: the separated part between the cytoplasm membrane and vitelline membrane or the explosive part in oocytes. (NMG-Asp buffer: 115mM NMG, 1mM $MgCl_2$, 5mM Hepes, pH 7.6)

Next, ion efflux efficiency from oocytes expressing (1) AQP1, (2) AQP1 and ChR2-XXM2.0, (3) AQP1 and *Gt*ACR1, (4) AQP1, ChR2-XXM2.0 and *Gt*ACR1, (5) ChR2-XXM2.0, (6) *Gt*ACR1, and (7) ChR2-XXM2.0 and *Gt*ACR1, were compared in 0.9x NMG-Asp buffer. After 20 min blue light illumination, the oocytes from group (4) exhibited shrinking significantly due to rapid osmotic gradient formation and high-speed water transport (Figure 3.7). Unlike ND96 buffer, Na^+ efflux was produced by ChR2-XXM2.0 in NMG-Asp buffer, which made oocyte membrane potential more negative to facilitate Cl^- movement from oocyte cytoplasm to outside through *Gt*ACR1. Taken together, two light-gated channels, ChR2-XXM2.0 and *Gt*ACR1 can be expressed in oocytes to produce osmotic gradients based on the movement of Na^+ and Cl^- in both ND96 buffer and NMG-Asp buffer. Meanwhile, this osmotic gradient could drive water transport through AQP1 to change the oocyte morphology, including swelling and shrinking.
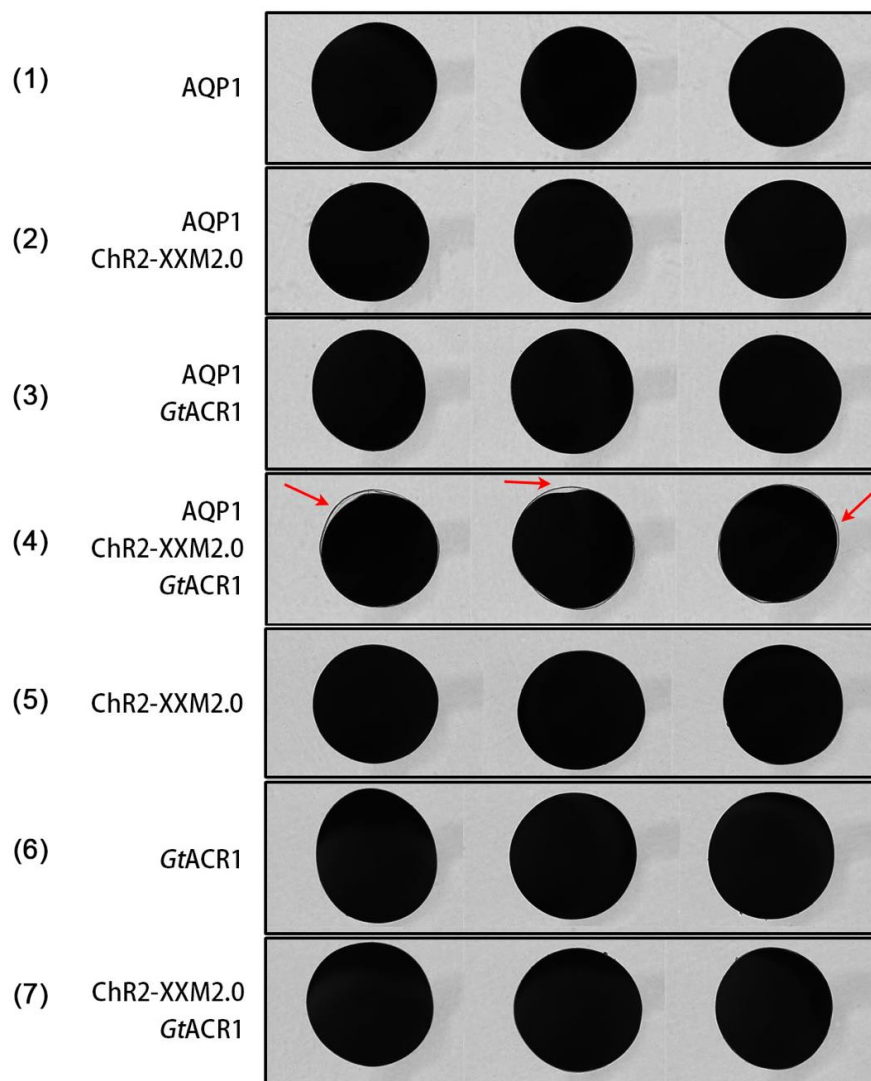
Figure 3.7 Light-induced oocyte shrinking in 0.9x NMG-Asp buffer after expressing different combinations of proteins.

The oocytes injected with different cRNAs (1) AQP1, (2) AQP1 and ChR2-XXM2.0, (3) AQP1 and *Gt*ACR1, (4) AQP1, ChR2-XXM2.0 and *Gt*ACR1, (5) ChR2-XXM2.0, (6) *Gt*ACR1, and (7) ChR2-XXM2.0 and *Gt*ACR1, were tested 2 dpi in 0.9x NMG-Asp buffer for shrinking efficiency according to the oocyte morphological changes. Before taking images, the oocytes were stimulated by 20 min blue illumination (LED: 470 nm, 100 μW/mm^2). Red arrow: the separated part between the cytoplasm membrane and vitelline membrane in oocytes. RNA amount: 5 ng AQP1, 30 ng ChR2-XXM2.0, 10 ng *Gt*ACR1.

3.1.5 Strategy for the tandem expression of ChR2 and *Gt*ACR1

The expression ratio for ChR2-XXM2.0 and *Gt*ACR1was not clear in oocytes by mixture RNA injection. To keep stable 1:1 expression level and make a convenient injection by only one RNA, two strategies to fuse ChR2-XXM2.0 and *Gt*ACR1 as a

single chain were compared. β linker is a transmembrane helix from the β subunit of the rat gastric H^+/K^+-ATPase [43]. Another one is the P2A sequence, one self-cleaving peptide from porcine teschovirus 2A [109]. ChR2-XXM2.0 was constructed in the N-terminal of β linker or P2A sequence while *Gt*ACR1 was in the C-terminal. The photocurrent from oocytes expressing (1) ChR2-XXM2.0 and *Gt*ACR1 (mixture injection), (2) ChR2-XXM2.0-β-*Gt*ACR1, and (3) ChR2-XXM2.0-P2A-*Gt*ACR1, were tested under different voltages. As shown in Figure 3.8, the inward photocurrent from ChR2-XXM2.0-β-*Gt*ACR1 was larger than that from ChR2-XXM2.0-P2A-*Gt*ACR, indicating that β linker is more efficient than the P2A sequence to link ChR2-XXM2.0 and *Gt*ACR1 together for ion transport.
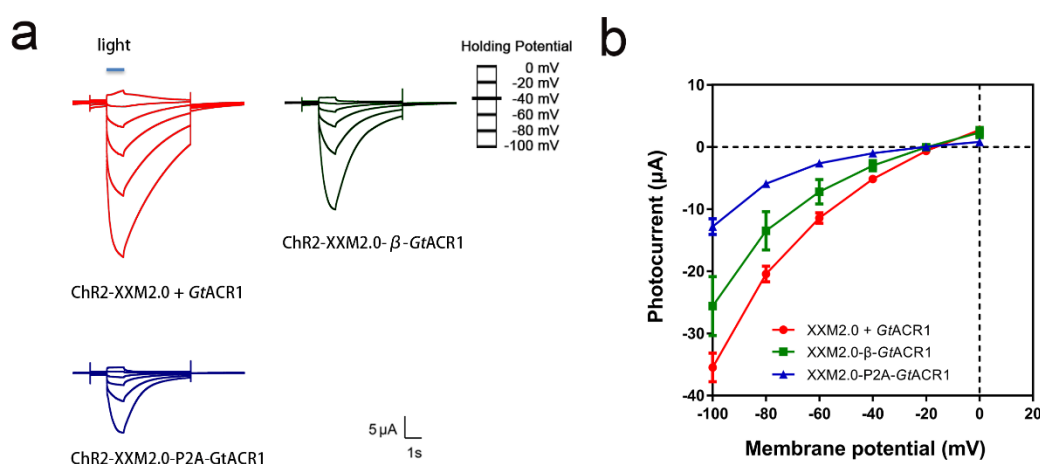

Figure 3.8 Integrating strategy comparison by photocurrent between using β linker and P2A sequence.

(a). 30 ng cRNA of ChR2-XXM2.0-β-*Gt*ACR1 or ChR2-XXM2.0-P2A-*Gt*ACR1 were injected for oocytes expression. ND96 buffer was used to test photocurrent from oocyte 2 dpi under different holding potentials by 1 s blue illumination. A 473 nm laser at 3 mW/mm^2 was used. The holding potential was changed from -100 to 0 mV. The mixture injection of 30 ng cRNA of ChR2-XXM2.0 and 10 ng *Gt*ACR1 were also tested as a control.

(b). The current-voltage relationship was concluded from 6 oocytes in each group.

As the mixture injection of ChR2-XXM2.0 and *Gt*ACR1 exhibited the highest photocurrent, we continued to use the mixture injection group as a positive control to compare water transport efficiency with ChR2-XXM2.0-β-*Gt*ACR1 and ChR2-XXM2.0-P2A-*Gt*ACR. In ND96 buffer, the oocytes expressing (1) AQP1, (2) AQP1, ChR2-XXM2.0 and *Gt*ACR1, (3) AQP1 and ChR2-XXM2.0-β-*Gt*ACR1, and (4) AQP1 and ChR2-XXM2.0-P2A-*Gt*ACR1 were exposed to blue light. The number of

swelling oocytes from each group was recorded every 20 min. 10 oocytes were tested in each group, and the recording was operated three times for statistical analysis. After the first 20 min, the significant swelling oocytes were observed from the group expressing ChR2-XXM2.0/GtACR1 or ChR2-XXM2.0-β-GtACR1(Figure 3.9a). Meanwhile, the significant shrinking oocytes were also exhibited in the two groups by changing ND96 buffer to 0.9x NMG-Asp buffer (Figure 3.9c). Even after 1 h, the percentage of swelling or shrinking oocytes from the group expressing ChR2-XXM2.0-β-GtACR1 was higher than ChR2-XXM2.0-P2A-GtACR1 expressing group, indicating that the water transport efficiency by β linker fused strategy is better than that of P2A sequence (Figure 3.9b and d).
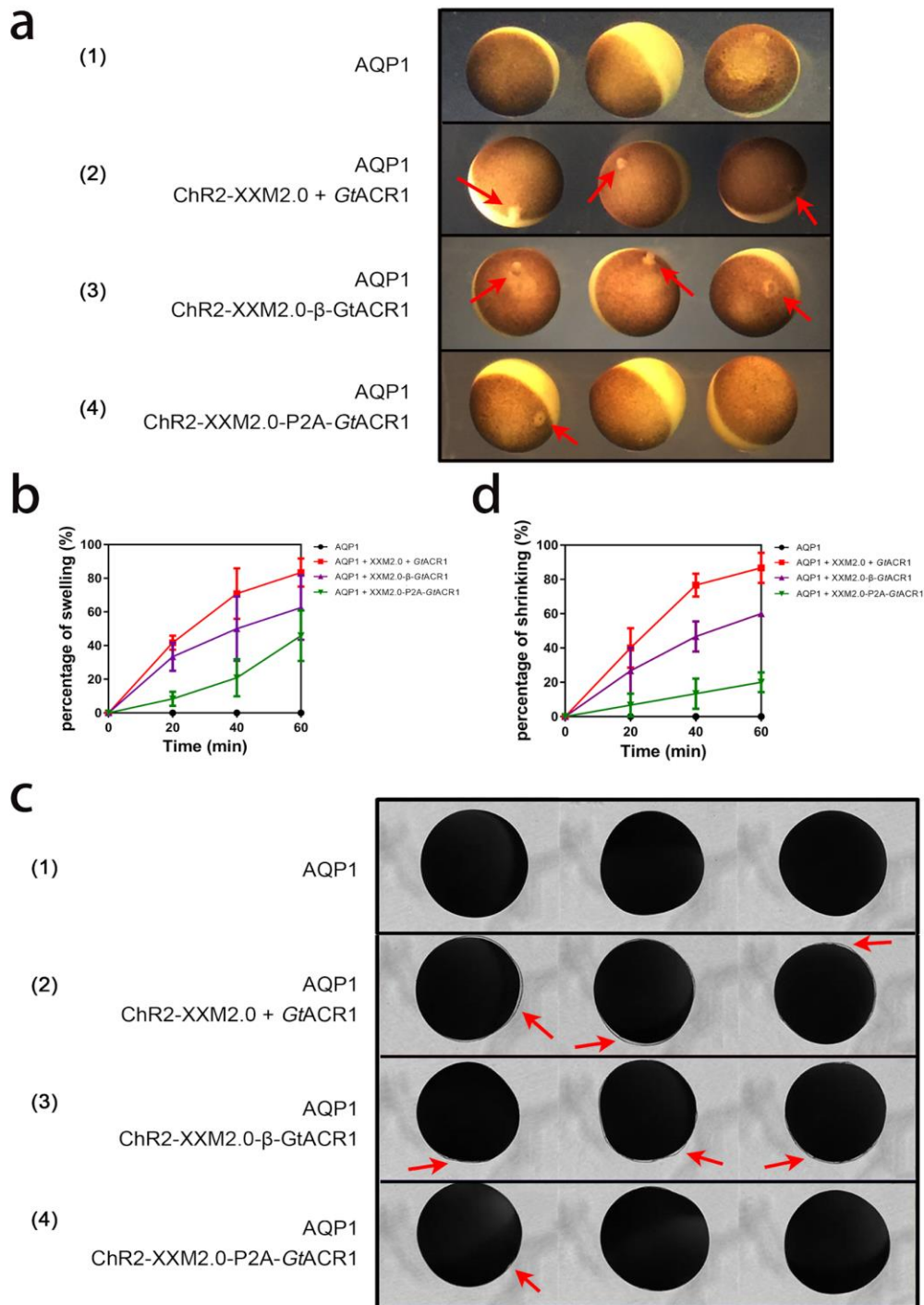
Fig. 3.9 Water transport efficiency comparison between β linker and P2A sequence fusion.
(a) and (c). The oocytes were tested 2dpi in ND96 buffer (a) and 0.9x NMG-Asp buffer (c) to compare light-triggered water transport efficiency via swelling and shrinking of oocyte morphological changes. The oocyte images were taken after 20 min blue illumination (LED: 470 nm, 100 μW/mm^2). Red arrow: the separated part between the cytoplasm membrane and vitelline membrane or the explosive part in oocytes. cRNA amount: 5 ng AQP1, 30 ng ChR2-XXM2.0, 10 ng *Gt*ACR1, 30 ng ChR2-XXM2.0-β-*Gt*ACR1, 30 ng ChR2-XXM2.0-P2A-*Gt*ACR1.

(b). 9 oocytes in each group were stimulated by blue illumination. The number of swelling oocytes was recorded every 20 min. n=3 experiments, error bars=SEM.

(d). 10 oocytes in each group were stimulated by blue illumination. The number of shrinking oocytes was recorded every 20 min. n=3 experiments, error bars=SEM.

3.1.6 Photocurrent of Sthk-bPAC and *Gt*ACR1 in *Xenopus* oocyte

As one of the most important ions in oocytes, the concentration of K^+ is higher than Na^+, ~100 mM [107]. I then designed another optogenetic tool for water transport regulation by K^+ channel. SthK-bPAC is a light-gated K^+ channel by fusing bacterial photoactivated adenylyl cyclase (bPAC) and cAMP-sensitive K^+ channel (SthK) together [110]. TEVC was performed to compare the oocytes expressing SthK-bPAC, *Gt*ACR1, and SthK-bPAC/*Gt*ACR1 under 0 mV in ND96 buffer (Figure 3.10). The *Gt*ACR1 expressing oocyte showed faster onset and offset by 1s blue light illumination than the oocyte expressing SthK-bPAC. Moreover, for the mixture injected oocyte with SthK-bPAC and *Gt*ACR1, the current exhibited both SthK-bPAC and *Gt*ACR1 characterizes: fast onset by blue light illumination and sustaining a long time under dark, indicating that SthK-bPAC and *Gt*ACR1 expressed well and could work together in one oocyte.
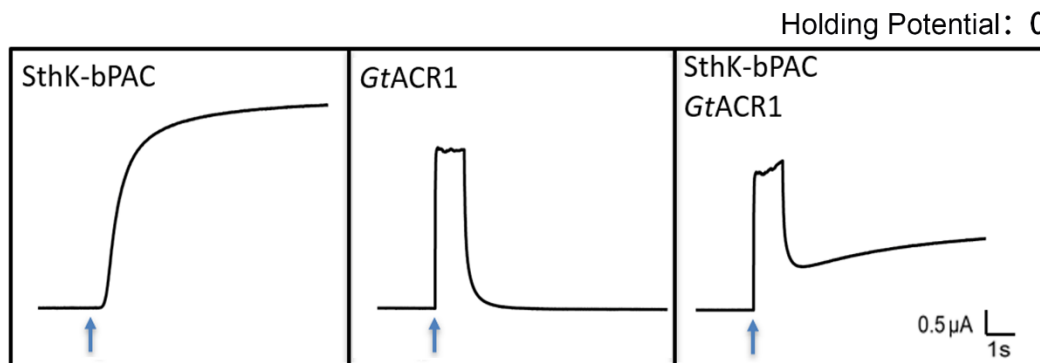
Figure 3.10 Co-expression of light-gated potassium and anion channels in *Xenopus* oocyte.
Photocurrents of 10 ng SthK-bPAC and 10 ng *Gt*ACR1 by single cRNA injection and mixture injection for oocytes expression were measured 2 dpi in ND96 buffer under 0 mV holding potential. The blue arrow indicated the start point of 1 s blue illumination. A 473 nm laser at 3 mW/mm^2 was used.

3.1.7 Oocyte shrinking in ND96 buffer via K^+/Cl^- efflux

In ND96 buffer, swelling can be found from the oocyte expressing AQP1, ChR2-XXM2.0 and *Gt*ACR1 under blue light illumination. This phenomenon resulted from

Na^+/Cl^- influx to establish the osmotic gradient and then stimulate water transport. Therefore, if SthK-bPAC and GtACR1 were co-expressed in oocytes, K^+ efflux could be induced and then made oocyte membrane potential more negative to promote Cl^- efflux. To compare the osmotic gradient formation based on K^+/Cl^- efflux by SthK-bPAC and GtACR1, the oocytes expressing (1) AQP1, (2) AQP1 and SthK-bPAC, (3) AQP1 and GtACR1, (4) AQP1, SthK-bPAC and GtACR1, (5) SthK-bPAC, (6) GtACR1, and (7) SthK-bPAC and GtACR1 were maintained in ND96 buffer. After 20 min illumination, the oocyte expressing AQP1, SthK-bPAC and GtACR1 showed a significant shrinking state, but nothing changed in other groups, suggesting that SthK-bPAC could connect with GtACR1 to fast induce osmotic gradient via K^+/Cl^- efflux under blue light and then accelerate water transport through AQP1 (Fig. 3.11).
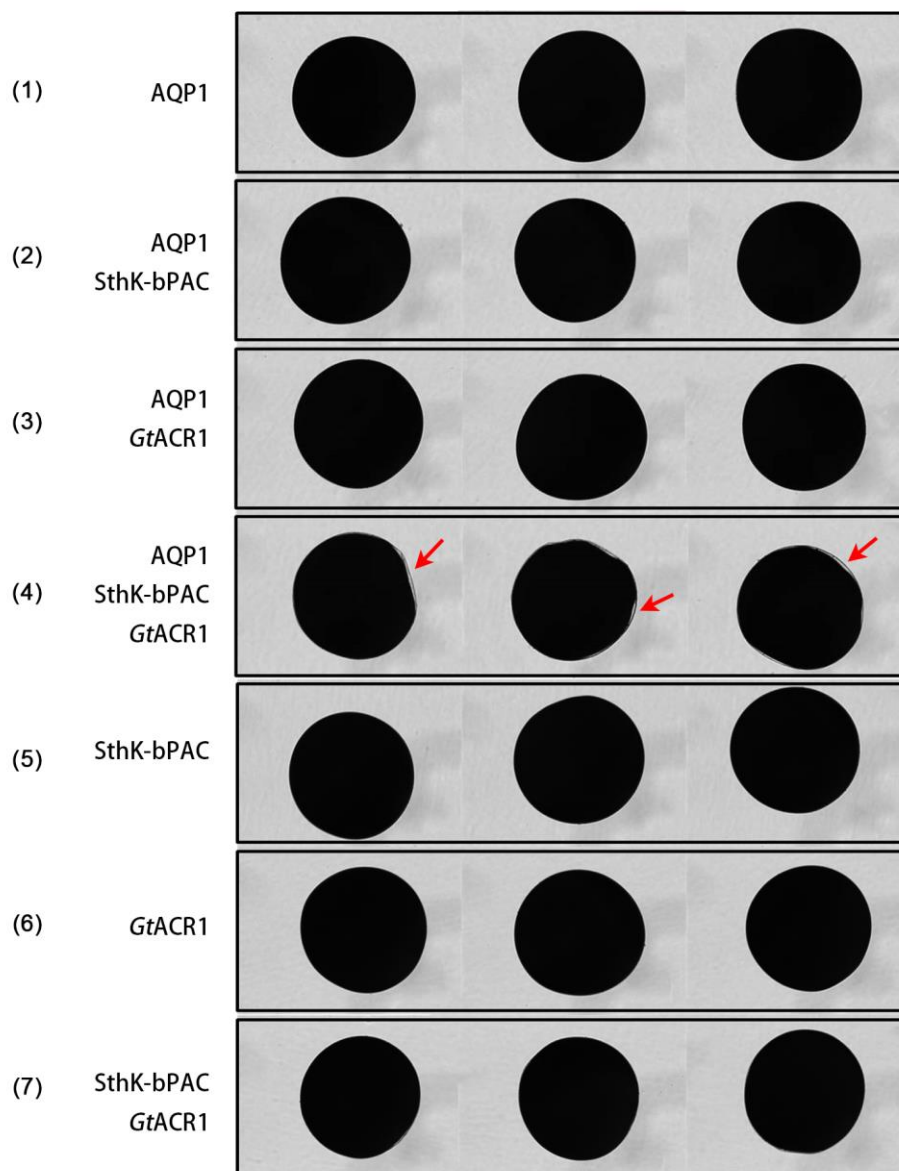
Figure 3.11 Light-induced oocyte shrinking in ND96 buffer after expressing different combinations of proteins.

The oocytes injected with different cRNAs (1) AQP1, (2) AQP1 and SthK-bPAC, (3) AQP1 and *Gt*ACR1, (4) AQP1, SthK-bPAC and *Gt*ACR1, (5) SthK-bPAC, (6) *Gt*ACR1, and (7) SthK-bPAC and *Gt*ACR1, were tested 2 dpi in ND96 buffer for shrinking efficiency according to the oocyte morphological changes. Before taking images, the oocytes were stimulated by 20 min blue illumination (LED: 470 nm, 100 μW/mm^2). Red arrow: the separated part between the cytoplasm membrane and vitelline membrane in oocytes. cRNA amount: 5 ng AQP1, 10 ng SthK-bPAC, 10 ng *Gt*ACR1.

3.1.8 Oocyte swelling in high K$^+$ buffer via K$^+$/Cl$^-$ influx

Besides shrinking, a high K$^+$ buffer was prepared to detect the opposite water movement efficiency based on K$^+$/Cl$^-$ influx through SthK-bPAC and *Gt*ACR1. The oocytes expressing (1) AQP1, (2) AQP1 and SthK-bPAC, (3) AQP1 and *Gt*ACR1, (4) AQP1, SthK-bPAC and *Gt*ACR1, (5) SthK-bPAC, (6) *Gt*ACR1, and (7) SthK-bPAC and *Gt*ACR1were maintained in high K$^+$ buffer to check swelling efficiency (Figure 3.12). As expected, after 20 min blue light illumination, the AQP1, SthK-bPAC and *Gt*ACR1 mixture injected oocytes exhibited swelling faster than other groups, indicating the successful cooperation of SthK-bPAC and *Gt*ACR1 to produce K$^+$/Cl$^-$ influx to form osmotic gradient by light and accelerate water uptake through AQP1.
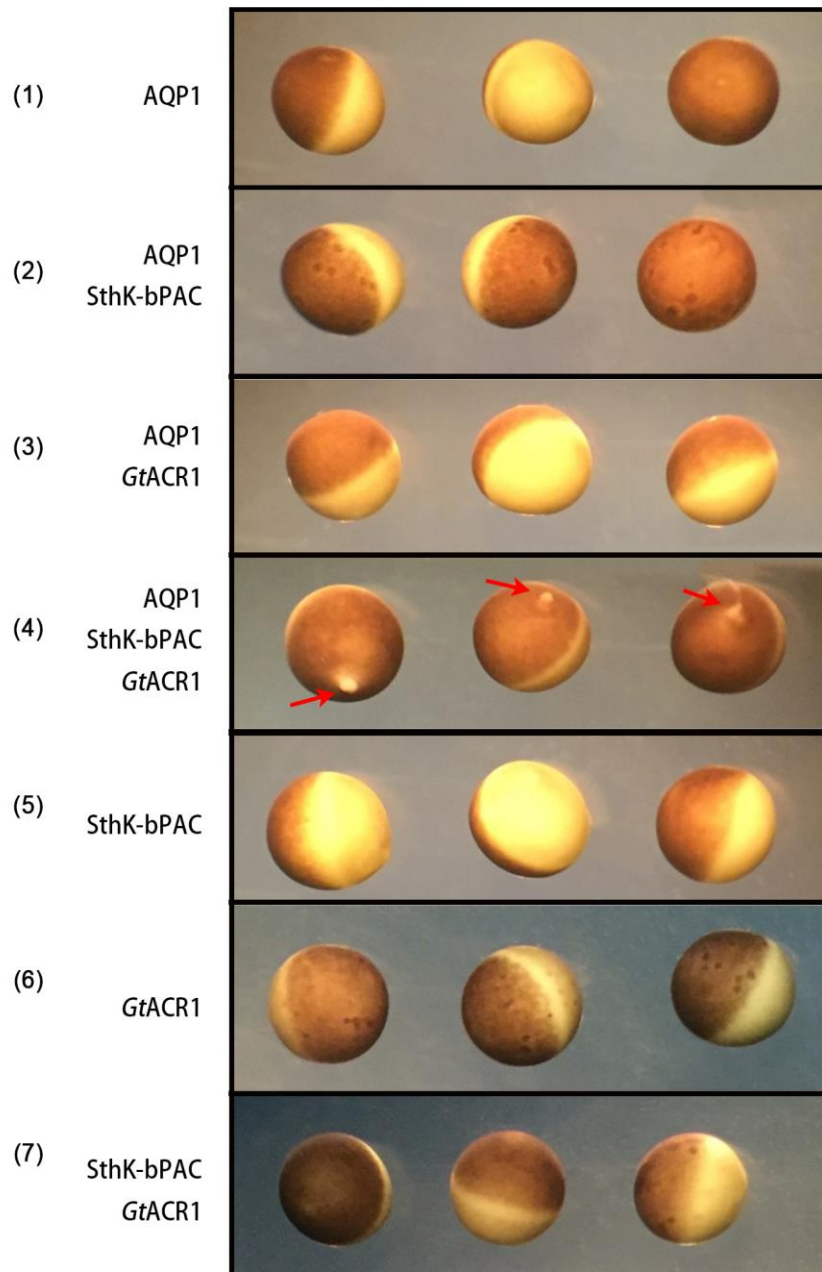
Figure 3.12 Light-induced oocyte swelling in high K⁺ buffer after expressing different combinations of proteins.

The oocytes injected with different RNAs (1) AQP1, (2) AQP1 and SthK-bPAC, (3) AQP1 and GtACR1, (4) AQP1, SthK-bPAC and *Gt*ACR1, (5) SthK-bPAC, (6) *Gt*ACR1, and (7) SthK-bPAC and *Gt*ACR1, were tested 2dpi in high K⁺ buffer (KCl 100 mM, MgCl₂ 10mM, Hepes 5mM, pH 7.6) for swelling efficiency according to the oocyte morphological changes. Before taking images, the oocytes were stimulated by 20 min blue illumination (LED: 470 nm, 100 μW/mm²). Red arrow: the explosive part in the oocyte. RNA amount: AQP1 5 ng, 10 ng SthK-bPAC, 10 ng *Gt*ACR1.

3.1.9 Strategy for the tandem expression of Sthk-bPAC and *Gt*ACR1

Fusing SthK-bPAC and *Gt*ACR1, β linker or P2A sequence were used again. Considering that SthK-bPAC includes two components and bPAC is functional as a homodimer, I further compared the difference of SthK-bPAC in N- and C-terminal when fused with *Gt*ACR1. For *Gt*ACR1, I modified the N-terminal via adding LucyRho (LR) signal peptide, increasing the membrane targeting efficiency [111]. After the expression of SthK-bPAC/*Gt*ACR1 and SthK-bPAC/LR-*Gt*ACR1 in oocytes, the photocurrent was compared in ND96 buffer. Under 0 mV holding potential, the photocurrent from LR-*Gt*ACR1 stimulated by 10s blue light was higher than *Gt*ACR1 photocurrent, suggesting that LR peptide modification could increase anion conductance (Figure 3.13a and b). Then, we designed four constructs: (1) SthK-bPAC-β-*Gt*ACR1, (2) Sthk-bPAC-P2A-*Gt*ACR1, (3) LR-*Gt*ACR1-SthK-bPAC, and (4) LR-*Gt*ACR1-YFP-SthK-bPAC to analyze photocurrent. After recording, we found LR-*Gt*ACR1-YFP-SthK-bPAC exhibited the largest photocurrent than other groups, indicating that SthK-bPAC should be fused in the C-terminal. Between SthK-bPAC and *Gt*ACR1, YFP or β linker could make the two channels more flexible, which is better than direct integration (Figure 3.13a and b). Meanwhile, similar to ChR2-XXM2.0-P2A-*Gt*ACR1, SthK-bPAC-P2A-*Gt*ACR1 also showed low photocurrent, suggesting low self-cleaving efficiency of P2A sequence in *Xenopus* oocyte. Taken together, two constructs, SthK-bPAC-β-*Gt*ACR1 and LR-*Gt*ACR1-YFP-SthK-bPAC, were selected to compare light-triggered water transport efficiency further.
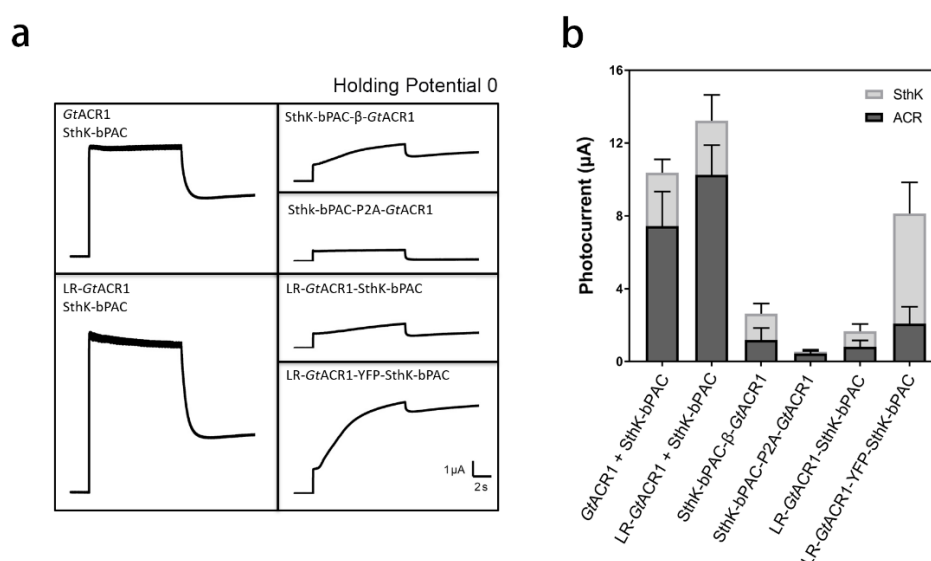

Figure 3.13 Fusion strategy comparison by photocurrent.

(a). Photocurrents from different SthK-bPAC and *Gt*ACR1 oocyte injection pathways were measured 2 dpi in ND96 buffer under 0 mV holding potential. For mixture injection, the cRNA amount of SthK-bPAC or *Gt*ACR1was 10 ng. For fused SthK-bPAC and *Gt*ACR1, 20 ng cRNA was injected for oocytes expression. The blue illumination was 10 s. A 473 nm laser at 3 mW/mm^2 was used.

(b). 6 oocytes in each group were concluded, error bars = SEM.

For swelling test by ND96 buffer, we prepared four groups (1) AQP1, (2) AQP1, SthK-bPAC and *Gt*ACR1, (3) AQP1 and SthK-bPAC-β-*Gt*ACR1, and (4) AQP1 and LR-*Gt*ACR1-YFP-SthK-bPAC. Based on large K$^+$/Cl$^-$ conductance, the oocyte expressing LR-*Gt*ACR1-YFP-SthK-bPAC exhibited large amounts of shrinking, closing to 90% after 1 h blue light stimulation (Figure 3.14a and b). Meanwhile, the oocytes with different injections were compared in the high K$^+$ buffer for swelling efficiency recording. The LR-*Gt*ACR1-YFP-SthK-bPAC expressing oocytes also exhibited faster water transport efficiency than the oocytes expressing SthK-bPAC-β-*Gt*ACR1 (Figure 3.14c and d). The fusing pattern of LR-*Gt*ACR1-YFP-SthK-bPAC is more suitable for light-triggered water transport application based on photocurrent and water transport efficient comparison.
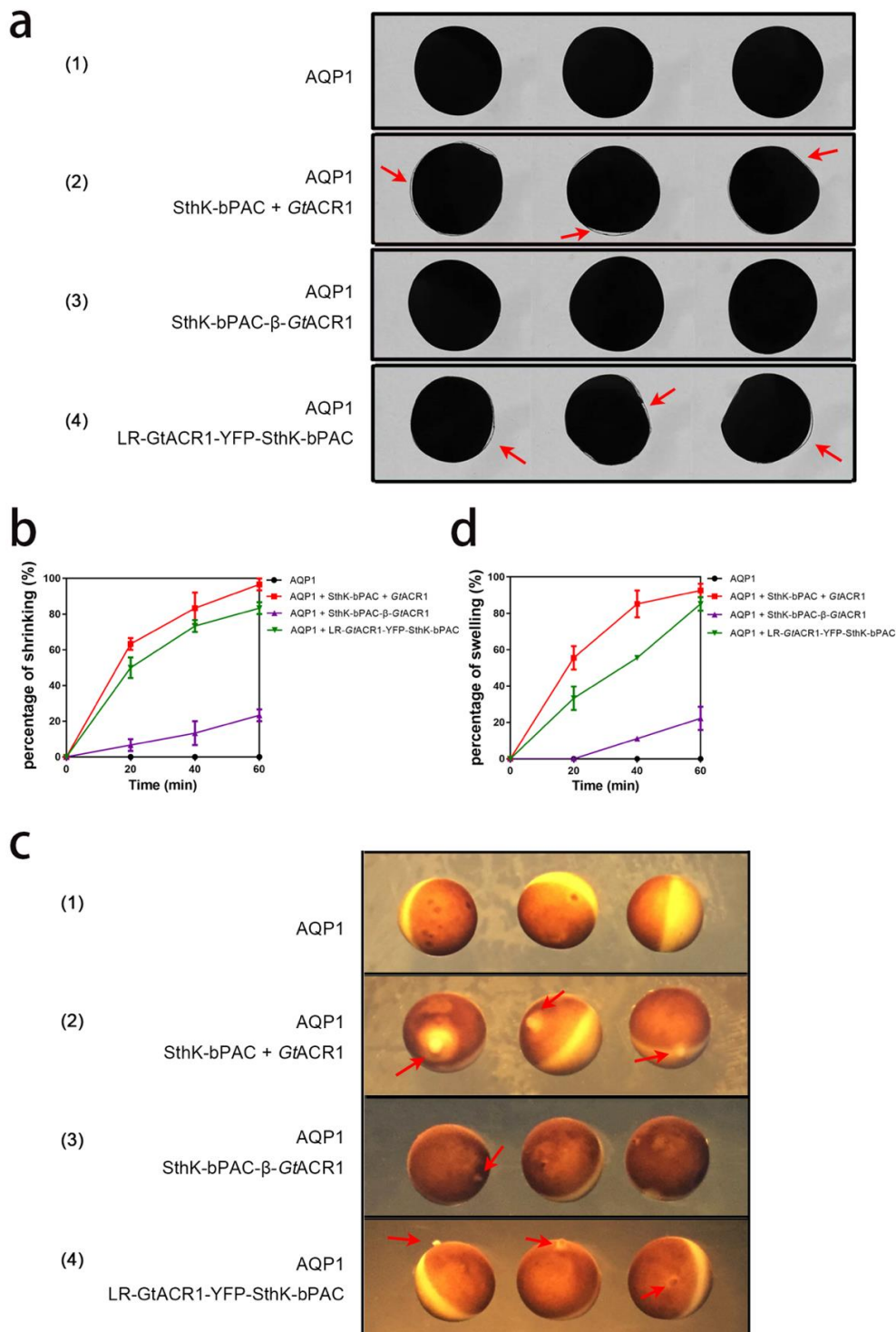
Figure 3.14 The comparison of light-triggered water transport efficiency.

(a) and (c). The oocytes were tested 2 dpi in ND96 buffer (a) and high K^+ buffer (c) to compare light-triggered water transport efficiency via shrinking and swelling of oocyte morphological changes. The oocyte images were taken after 20 min blue illumination (LED: 470 nm, 100 $\mu W/mm^2$). Red arrow: the separated part between the cytoplasm membrane and vitelline membrane or the

explosive part in oocytes. cRNA amount: 5 ng AQP1, 10 ng SthK-bPAC, 10 ng *Gt*ACR1, 20 ng SthK-bPAC-β-*Gt*ACR1, 20 ng LR-*Gt*ACR1-YFP-SthK-bPAC.

(b). 10 oocytes in each group were stimulated by blue illumination. The number of swelling oocytes was recorded every 20 min. n=3 experiments, error bars=SEM.

(d). 9 oocytes in each group were stimulated by blue illumination. The number of shrinking oocytes was recorded every 20 min. n=3 experiments, error bars=SEM.

3.2 light-controlled protein purification

3.2.1 Characterization of iLID-SspB via *Xenopus* oocyte

To measure the binding efficiency between iLID and SspB in *Xenopus* oocyte, I first focused on SspB_nano with the highest binding affinity (4.7 µM in the dark and 0.132 µM in the light) [95]. YFP was fused to the N- or C-terminal of SspB_nano for oocyte expression as a soluble protein, respectively (Figure 3.15a). According to YFP fluorescence of the supernatant harvested from oocytes expressing YFP-SspB_nano or SspB_nano-YFP for two days, these two constructs showed similar expression levels (Figure 3.15b). Membrane targeting peptide Lyn11 (11 amino acids from the N-terminal myristoylated/palmitoylated domain of human Lyn tyrosine kinase) was fused to the N-terminal of iLID for oocyte membrane targeting expression. After two days expression in the dark, the supernatant was harvested by 5 min low-speed centrifugation, which comprised the membrane fragments and soluble proteins. And then, by 1.5 min high-speed centrifugation, membrane fractions with Lyn-iLID were isolated from this supernatant. The whole process of membrane isolation should be in the dark to keep Lyn-iLID in the caged stage. Based on the high affinity between iLID and SspB_nano, I hypothesized that if the soluble fraction with YFP-SspB_nano or SspB_nano-YFP and membrane fraction with Lyn-iLID were mixed under blue light (470 nm, ~100 µW/mm^2), Lyn-iLID could bond and precipitate YFP-SspB_nano or SspB_nano-YFP from the soluble fraction after high-speed centrifugation. As expected, after 30 min illumination, the results elicited a significant fluorescence decrease in the soluble fraction compared with the dark (Figure 3.15c). Meanwhile, YFP fluorescence from the sediment of membrane fraction, which has bonded soluble SspB in the light, was detected and indicated ~6-fold fluorescence increase compared with that in the dark (Figure 3.15d). In addition, YFP-SspB_nano and SspB_nano-YFP showed similar precipitate efficiency (~50%) by Lyn-iLID. Then the position of iLID and SspB was exchanged: SspB_nano was anchored to the oocyte membrane by Lyn sequence and iLID was fused with YFP as the soluble fraction (Figure 3.15a). However, the results showed a low YFP-iLID expression level and weak binding affinity (Figure 3.15b, c and d). Therefore, YFP-SspB_nano/Lyn-iLID was chosen for further research based on high binding efficiency.
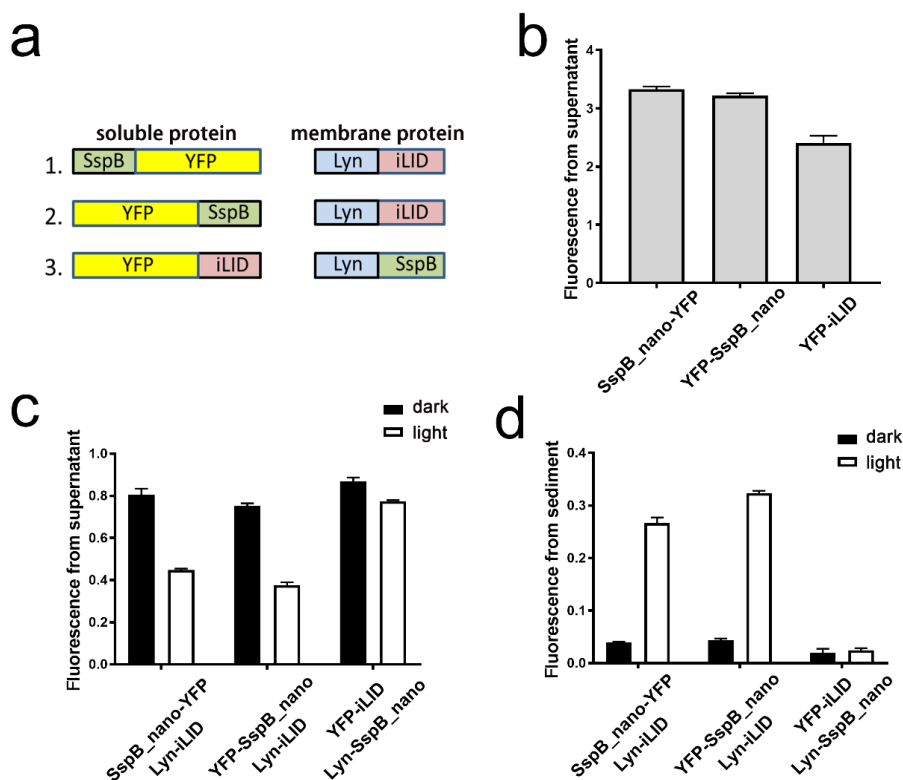
Figure 3.15 Evaluating the binding of iLID/sspB_nano.

(a). Schematic of SspB_nano/iLID constructs.

(b). The expression level of SspB_nano-YFP, YFP-SspB_nano and YFP-iLID in soluble fractions were compared by fluorescence emission values of YFP. 20 ng cRNA for each construct were expressed in *Xenopus* oocyte for 2 days. The soluble fraction from 10 oocytes was harvested after 30 min high-speed centrifugation.

(c) and (d). The rest of YFP fluorescence emission values in the soluble fraction (c) and the increase of YFP fluorescence emission values in the membrane fraction (d) after binding under dark or 30 min blue illumination. 30 ng cRNA of Lyn-iLID or Lyn-SspB was expressed in *Xenopus* oocyte as membrane fraction. The initial concentration for the soluble fraction in each test was 20 nM (in 300 μL buffer A), and the membrane fraction was from 25 oocytes. n=3 experiments, error bars=SEM.

Long time blue light exposure could contribute to irreversible recovery under dark for LOV2 domain *in vitro*. Thus time-dependent binding efficiency was further checked. The robust interaction for YFP-SspB_nano/Lyn-iLID was observed within 20 min (Figure 3.16a), suggesting that 20 min illumination was enough for precipitation *in vitro*. Then the time-dependent releasing efficiency of YFP-SspB_nano from Lyn-iLID was tested under dark. The sediment, including YFP-SspB_nano/Lyn-iLID from Fig. 3.16a, was harvested and resuspended by fresh buffer A, and moved into dark condition for release at different times. After 1.5 min high-speed centrifugation for soluble fraction

and membrane fraction separation, the released (also purified) YFP-sspB_nano from membrane fraction reached ~2 nM by 30 min (Figure 3.16b), suggesting that light-controlled binding and releasing by iLID system could be confirmed in *Xenopus* oocyte.
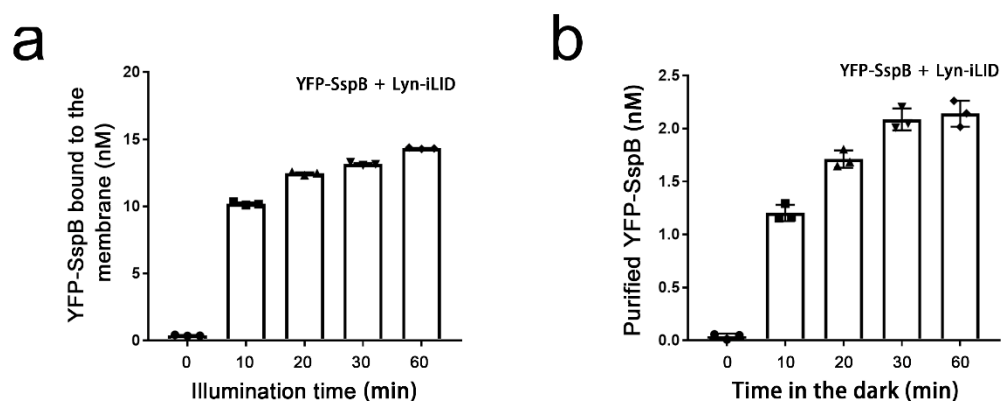

Figure 3.16 Time-dependent binding and dissociation efficiency of YFP-SspB_nano/Lyn-iLID.
(a). Time-dependent binding efficiency between Lyn-iLID and YFP-SspB under blue illumination. Each reaction contained 40 nM YFP-SspB (in 300 μL buffer A) and membrane fraction from 25 oocytes.

(b) Time-dependent release efficiency from Lyn-iLID and YFP-SspB binding complex stimulated by 20 min blue light from (a). The binding complex was resuspended by 300 μL fresh buffer A after three-time washing. The concentration of released YFP-SspB in supernatant was tested according to fluorescence emission after 30 min high-speed centrifugation at 4 °C. n = 3, error bars = SEM.

SspB_nano has two other variants: SspB_micro (binding affinity 47 μM in the dark and 0.8 μM in the light) and SspB_milli (binding affinity >1 mM in the dark and 56 μM in the light) [100]. I then fused YFP to the N-terminal of SspB_micro and SspB_milli expressed in oocyte for two days. The supernatant containing YFP-SspB_micro or YFP-SspB_milli and the sediment containing Lyn-iLID were mixed like YFP-SspB_nano/Lyn-iLID. After 20 min blue light illumination or in the dark as control, the fluorescence in supernatant and sediment were tested following high-speed centrifugation. YFP fluorescence value in the supernatant showed that more than 50% YFP-SspB were precipitated from both YFP-SspB_nano/Lyn-iLID and YFP-SspB_micro/Lyn-iLID, and ~6-fold fluorescence increased in sediment by light compared to dark group (Figure 3.17a and b). However, for YFP-SspB_milli/Lyn-iLID, the fluorescence in the supernatant and sediment did not exhibit significant light-dependent change (Figure 3.17a and b). According to the analysis from competitive fluorescence polarization binding assays by Guntas et al. [95], the concentration of Lyn-iLID for reaction from 25 oocytes could be 500 nM, which is lower than SspB_nano

and SspB_micro light binding affinity. Therefore, the precipitated efficiency from YFP-SspB_micro/Lyn-iLID was lower than that from YFP-SspB_nano/Lyn-iLID, and nothing was found in YFP-SspB_milli/Lyn-iLID. The isolated sediment was resuspended by fresh buffer A and moved into the dark to make YFP-SspB release. After 30 min, the fresh supernatant and sediment were isolated again by 1.5 min high-speed centrifugation, and the fluorescence was detected separately. However, due to the low concentration of Lyn-iLID in membrane fraction from oocytes, YFP-SspB_micro showed lower dissociated efficiency than YFP-SspB_nano (Figure 3.17c and d). Thus, these results further confirmed that the oocyte system could be used to prove iLID-SspB interaction *in vitro*. But, because of the low expression level and release efficiency, *Xenopus* oocyte was not appropriate for testing protein purification efficiency by light-controlled dimer.
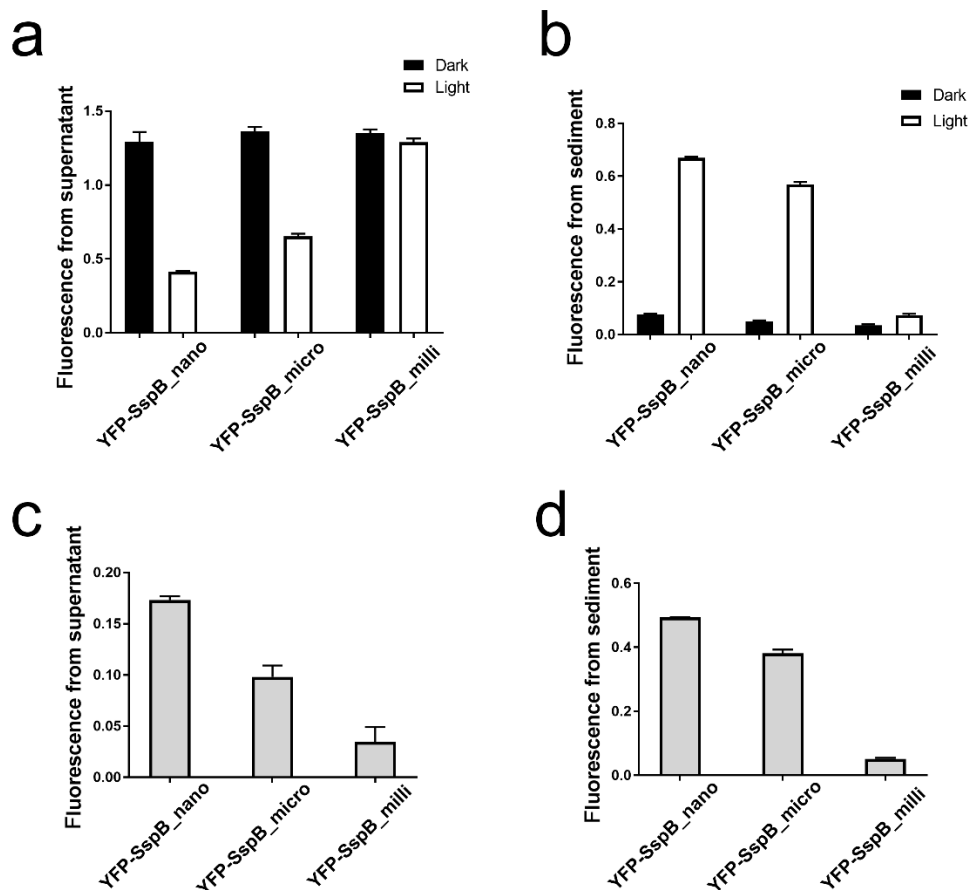

Figure 3.17 Characterization of SspB_nano, SspB_micro, and SspB_milli.

(a) and (b). The rest of YFP fluorescence emission values in the soluble fraction (a) and the increase of YFP fluorescence emission values in the membrane fraction (b) after binding under dark or 30 min blue illumination. 30 ng cRNA of each construct were expressed in *Xenopus* oocyte for 2 days.

The initial concentration for the soluble fraction in each test was 25 nM (in 300 μL buffer A), and the membrane fraction was from 25 oocytes. n=3 experiments, error bars=SEM.

(c). YFP fluorescence in the fresh supernatant was the released YFP-SspB from the light-induced binding complex of (b). The binding complex was resuspended by 300 μL fresh buffer A, moved into dark for 30 min, and centrifuged with high speed.

(d). The membrane fraction was harvested from (c), washed and resuspended by 300 μL buffer A to test the rest of YFP fluorescence after release. n=3, error bars=SEM.

3.2.2 iLID-SspB expression and YFP purification in *E. coli*

Plasmids pET28b-YFP-SspB_nano and pET28b-H1021-iLID were introduced into *E. coli* BL21(DE3), separately. Samples were treated by ultrasonic disruption and centrifuged to separate soluble fraction and membrane fraction. SDS-PAGE analysis was carried out with the collected samples to get an overview on the expression level of YFP-SspB and H1021-iLID (H1021: Membrane targeting peptide for *E. coli* [112]). For soluble protein YFP-SspB_nano, an expected band of 45 kDa in the supernatant was seen after induced by 0.5 mM IPTG (Figure 3.18). Meanwhile, membrane protein H1021-iLID was detected in sediment with a size of 24 kDa.
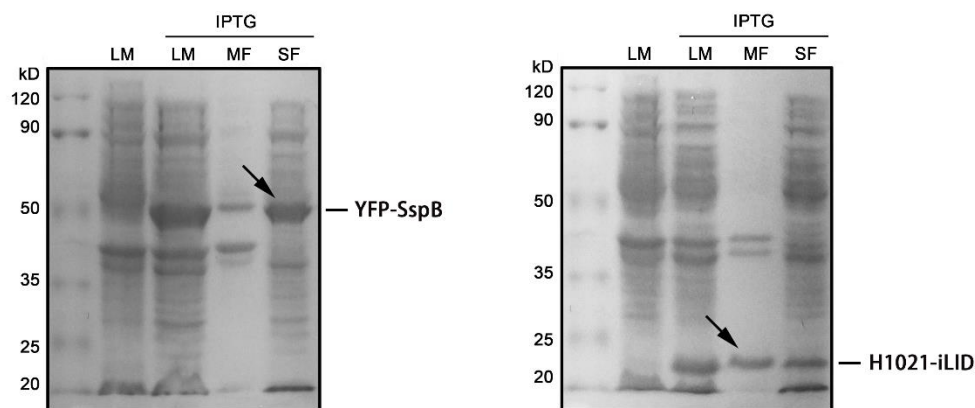
Figure 3.18 Expression of YFP-SspB and H1021-iLID in *E. coli*.

Expression of YFP-SspB_nano and H1021-iLID in *E. coli*. 50 mL media with cultured *E. coli* was washed and resuspended by 1 mL buffer A. 5 μL from each sample was mixed with loading buffer to run SDS-PAGE. The gel was stained by EZBlue for 30 min and washed by water. LM: the lysed mixture after ultrasonic treatment. MF: membrane fraction. SF: soluble fraction. YFP-SspB (45 kDa) in the soluble fraction or H1021-iLID (24 kDa) in the membrane fraction was indicated by the black arrow.

Due to low releasing efficiency by SspB in *Xenopus* oocyte system, we then fused YFP to the N-terminal of SspB_nano, SspB_micro and SspB_milli expressed in *E. coli*

BL21(DE3) to compare light-controlled protein purification efficiency, respectively. Soluble fractions with YFP-SspB (4 μM) and membrane fractions with H1021-ILID (from 10 mL *E. coli* media) were mixed under dark or 20 min blue illumination. After precipitation by centrifugation, the unbonded soluble fraction was washed off. The membrane fraction was washed three times, resuspended by 200 μL buffer A, and moved into dark condition to release the bonded soluble fraction. The released soluble fraction containing YFP-SspB was harvested by 30 min high-speed centrifugation, and the concentrations of YFP-SspB_nano, YFP-SspB_micro, and YFP-SspB_milli were calculated by fluorescent emission value. Interestingly, the concentration of released SspB_milli was ~10 times higher than SspB_nano and SspB_micro (Figure 3.19a). Then, 10 μL of each sample was loaded in SDS-PAGE to analyze whether the released soluble fraction was pure or not. As shown in Fig. 3.19b, only one band of YFP-SspB_milli can be seen from the light group, indicating that H1021-iLID/SspB_milli can be used for light-controlled protein purification.

As mention before, the affinity of SspB_nano is ~400 times higher than SspB_milli under light, so that H1021-iLID could precipitate and release more YFP-SspB_nano. However, the significant release of YFP-SspB_nano was not observed. To compare the light and dark affinity among the dimers of YFP-SspB_nano/H1021-iLID, YFP-SspB_micro/H1021-iLID and YFP-SspB_milli/H1021-iLID, different concentrations of YFP-SspB were used to mix with H1021-iLID harvested from 2.5 mL *E. coli* media. After 20 min reaction, the fluorescence of YFP-SspB in the membrane fraction was tested, reflecting the precipitated efficiency by H1021-iLID. As shown in Fig. 3.19c, SspB_nano exhibited very high dark activity with an L/D ratio (light activity/dark activity) of ~1.4 under 4 μM soluble fraction mixture, which contributes to low releasing efficiency in the dark. The light activities between SspB_micro and SspB_milli were similar, whereas SspB_milli showed lower dark activity. Under 4 μM soluble fraction, the L/D ratio for SspB_micro and SspB_milli is ~1.5 and 6, respectively. Therefore, iLID/SspB_milli exhibited the highest releasing efficiency that can be used as a light-controlled protein purification tool.
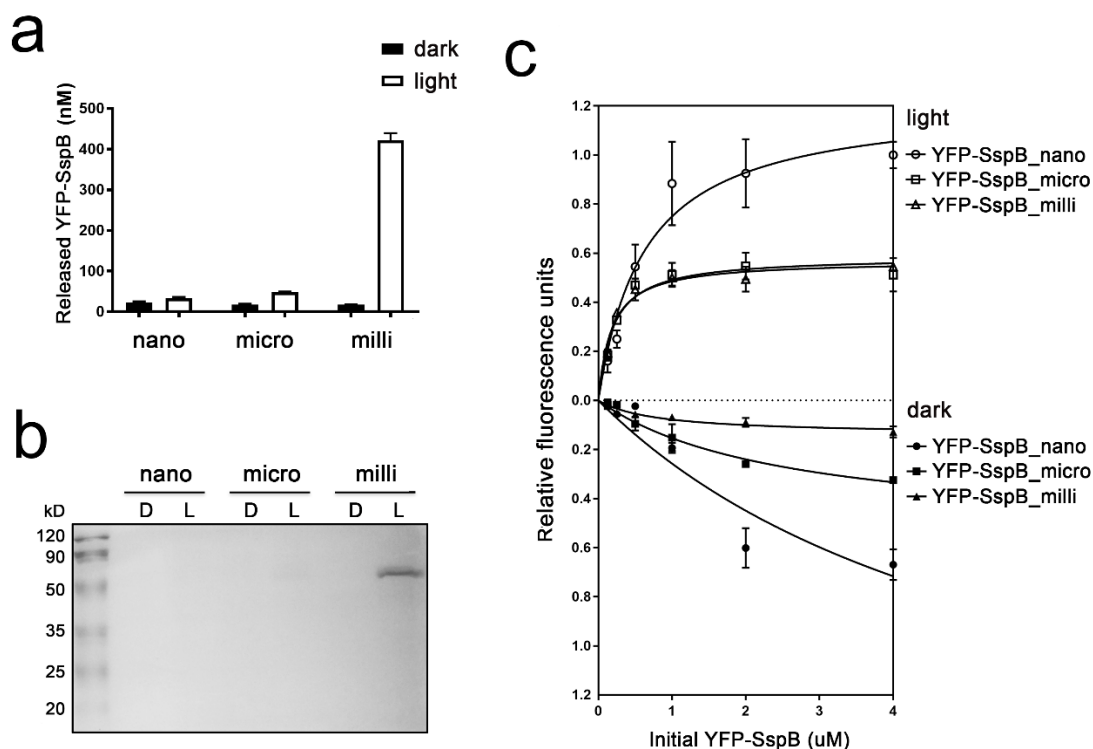
Figure 3.19 The purity of YFP-SspB after releasing.

(a). The membrane fraction (from 10 mL *E. coli*) binding with the soluble fraction (4 μM YFP-SspB) by dark or 20 min blue illumination was moved into dark for 30 min. The binding complex was resuspended by 200 μL fresh buffer A. The concentration of released YFP-SspB in the supernatant was tested according to fluorescence emission after 30 min high-speed centrifugation in 4 °C. (nano: YFP-SspB_nano. micro: YFP-SspB_micro. milli: YFP-SspB_milli.)

(b). 10 μL of the released YFP-SspB from (a) were tested in SDS-PAGE. YFP-SspB was indicated by the black arrow. D: binding in the dark. L: binding in the light.

(c). The amount of precipitated YFP-SspB was tested according to fluorescence emission from membrane fractions (H1021-iLID) after mixture with soluble fractions (YFP-SspB_nano/micro/milli) under dark or 20 min blue illumination. In each reaction, the membrane fraction from 2.5 mL *E. coli* was mixed with different concentrations of YFP-SspB (in 300 μL buffer A). Before testing, the membrane fractions were washed three times by 300 μL buffer A. Fluorescence emission values were normalized with light-induced reaction under 4 μM YFP-SspB_nano as 1 after subtraction of control emission values. n = 3, error bars = SEM.

3.2.3 Monomeric SspB generation and characterization

Despite the light-controlled protein purification based on iLID/SspB_milli is applicable, the target protein activity fused with SspB_milli was not clear. It should be pointed out that SspB is functional as a homodimer to regulate SsrA-tagged substrate degradation.

The dimeric form of SspB may affect the activity of target proteins. To check the dimeric level of YFP-SspB_milli, the purified YFP-SspB_milli was loaded in native PAGE gel with the soluble fraction from *E. coli* expressing YFP-SspB_milli. BSA was loaded as the marker, 66 kDa in a monomeric state and 132 kDa in a dimeric form. For YFP-SspB_milli, its isoelectric point (pI) is ~5. Therefore, in buffer A with pH 7.6, YFP-SspB_milli was carrying the negative charge and capable of moving in native PAGE gel. As shown in Fig. 3.20a, the position of YFP-SspB_milli was around 100 kDa, suggesting that the purified protein with a SspB_milli tag is apt to form the dimer. To solve this problem, eight mutations (L6R, R9E, Y12Q, L13K, A16E, F17K, W20E, D23K [98]) were introduced into SspB α-helix 1 (SspB_milli-8M), which has been reported to disturb hydrophobic interaction in the dimer-interface exhibiting monomeric state in native PAGE (Figure 3.20a). I next used membrane fraction from 2.5 mL *E. coli* media containing H1021-iLID to precipitate YFP-SspB_milli-8M. However, the fluorescence in the sediment was too low to be observed, indicating that SspB_milli-8M cannot be used for protein purification due to low binding affinity (Figure 3.20b).
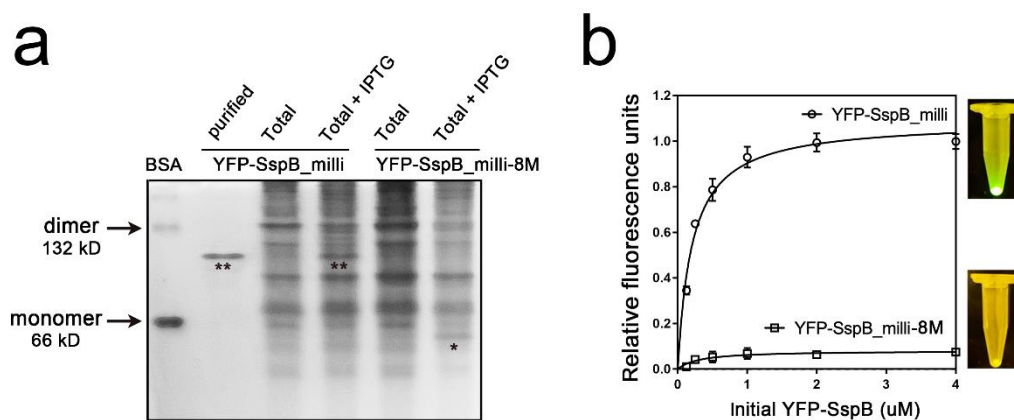
Figure 3.20 the comparison of monomeric and dimeric SspB.

(a). The protein state of YFP-SspB_milli and YFP-SspB_milli-8M in native PAGE. YFP-SspB expressed by *E. coli* with or without IPTG induce from 50 mL media was washed and resuspended by 1 mL buffer A. 5 μL from each sample was mixed with the loading buffer to run native PAGE. The gel was stained by EZBlue for 30 min and washed by water. Total: the whole cell lysed mixture after ultrasonic treatment (∗: monomer, ∗∗: dimer).

(b). The difference of binding affinity between monomeric and dimeric YFP-SspB_milli to H1021-iLID under 20 min blue illumination. In each reaction, the membrane fraction from 2.5 mL *E. coli* was mixed with different concentrations of YFP-SspB (in 300 μL buffer A). Fluorescence emission

values were normalized with light-induced reaction under 4 µM YFP-SspB_milli as 1 after subtraction of control emission values. n = 3, error bars = SEM.

However, unlike SspB_milli-8M, SspB_nano-8M still keeps the affinity to SsrA [98]. Therefore, we next compared light and dark activity between SspB_nano and SspB_nano-8M. In addition, according to the structure of the dimeric SspB complex in antiparallel form (Figure 3.21a), I then constructed two new mutants: SspB_nano-3M (K9A, Y12L and L13V) and SspB_nano-3AM (K9A, Y12A and L13A) (Figure 3.21e). The mutations were selected for the following reasons. First, the hydrophobic residues Tyr12 and Leu13, which are important to maintaining hydrophobic core in SspB, participate in the interaction of dimeric SspB (Figure 3.21b and c) [97, 98]. Second, Lys9 could interact with Asp100* through a hydrogen bond in the dimer interface (Figure 3.21d). After fusing with YFP, the binding affinity of SspB_nano, SspB_nano-3M, SspB_nano-3AM and SspB_nano-8M to H1021-iLID were compared together. I found that if the residues Tyr12 and Leu13 are mutated to polar, like that in SspB_nano-8M, or smaller residues, like that in SspB_nano-3AM, the hydrophobic core of SspB was destroyed, affecting the binding between SspB and SsrA further (Figure 3.21f). For SspB_nano-3M, the light activity was close to SspB_nano, whereas the dark activity decreased significantly, indicating that SspB_nano-3M could also be used for protein purification (Figure 3.21f). I then purified YFP-SspB_nano-3M like YFP-SspB_milli and loaded in native PAGE gel. As shown in Fig. 3.21g, YFP-SspB_nano-3M exhibited the main band ~48 kDa as a monomer, indicating that three mutations (K9A, Y12L and L13V) in α-helix 1 of SspB successfully prevent homodimer formation.
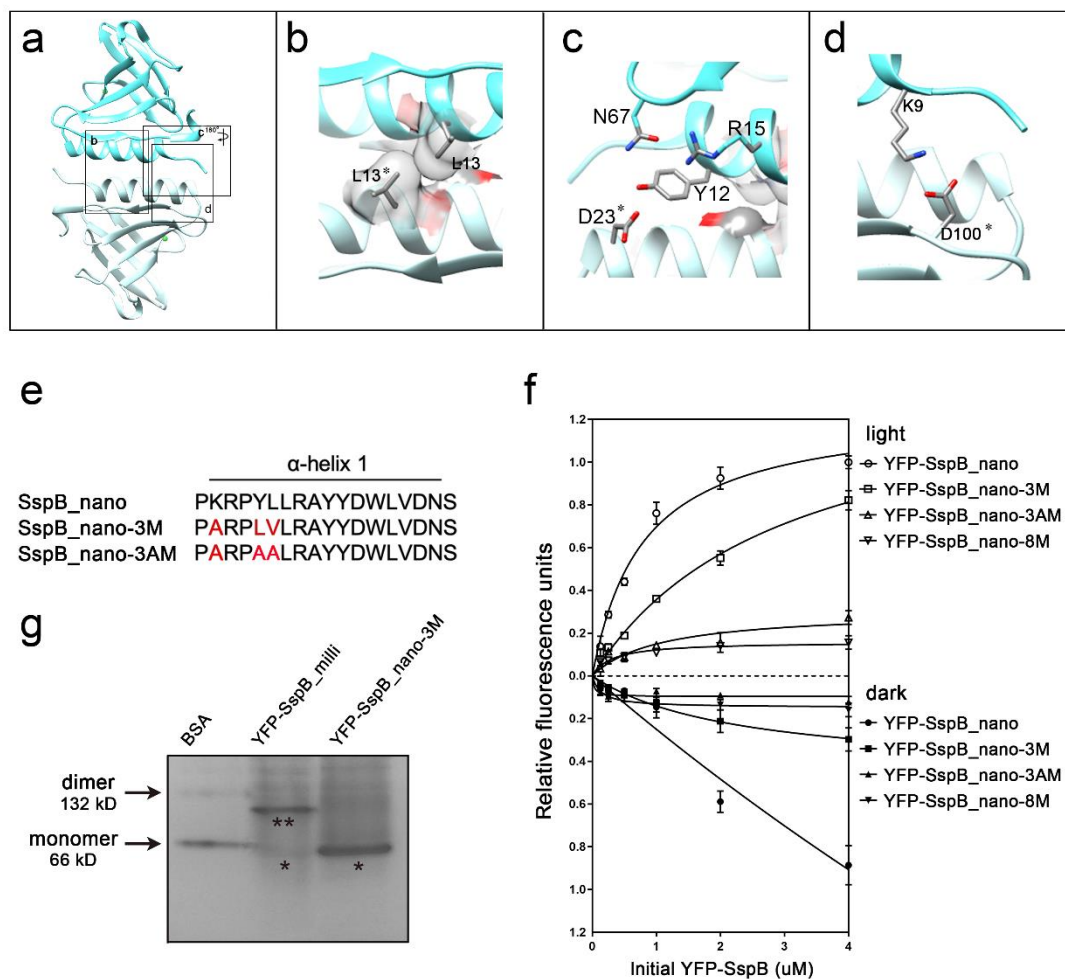
Figure 3.21 The binding affinity comparison between SspB mutants.

(a). The dimeric SspB complex in antiparallel form. (generated from PDB ID: 1ZSZ).

(b) The hydrophobic interaction between Leu13 and Leu13* in the dimer-interface. (*: the antiparallel SspB)

(c) The Tyr12 form a potential interaction with Asp23* through a hydrogen bond in the dimer-interface and might also participate in maintaining the monomer structure by interactions with Asn67 and Arg15.

(d) The Lys9 interacted with Asp100* through a hydrogen bond in the dimer-interface.

(e) The position of point mutations in SspB α-helix1 (red: K9, Y12 and L13).

(f) The amount of precipitated YFP-SspB was tested according to fluorescence emission from membrane fractions (H1021-iLID) after mixture with soluble fractions (different variants of YFP-SspB) under dark or 20 min blue illumination. In each reaction, the membrane fraction from 2.5 mL E. coli was mixed with different concentrations of YFP-SspB (in 300 μL buffer A). Before testing, the membrane fractions were washed three times by 300 μL buffer A. Fluorescence emission values were normalized with light-induced reaction under 4 μM YFP-SspB_nano as 1 after subtraction of control emission values. n = 3, error bars = SEM.

(g) The protein state of purified YFP-SspB (milli and nano_3M) in native PAGE. 200 ng of each sample was loaded (∗: monomer, ∗∗: dimer).

SspB_nano-3M was further compared to SspB_micro-3M and SspB_milli-3M. However, both SspB_micro-3M and SspB_milli-3M showed functional loss that cannot be precipitated by H1021-iLID under light (Figure 3.22).
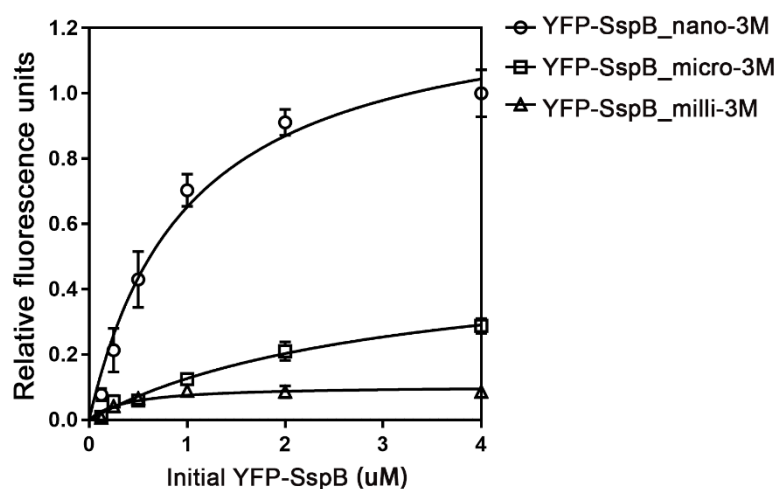
Figure 3.22 The binding affinity comparison between SspB-3M.
The difference of binding affinity of SspB_nano-3M, SspB_micro-3M and SspB_milli-3M under blue light. Fluorescence emission values were normalized with the reaction under 4 μM YFP-SspB_nano-3M as 1 after subtraction of control emission values. n = 3, error bars = SEM.

The binding affinity and releasing efficiency of YFP-SspB_nano-3M were further compared with YFP-SspB_milli. Under 4 μM soluble fraction, there is no significant difference in the L/D ratio between YFP-SspB_nano-3M (~5) and YFP-SspB_milli (~6) (Figure 3.23a), whereas higher releasing efficiency from YFP-SspB_nano-3M was observed (Figure 3.23b). Several factors could explain these differences. For example, the binding amount of YFP-SspB_nano-3M by H1021-iLID was two-fold higher than YFP-SspB_milli. It is also possible that the binding between SsrA and monomeric SspB becomes unstable, leading to higher releasing efficiency.
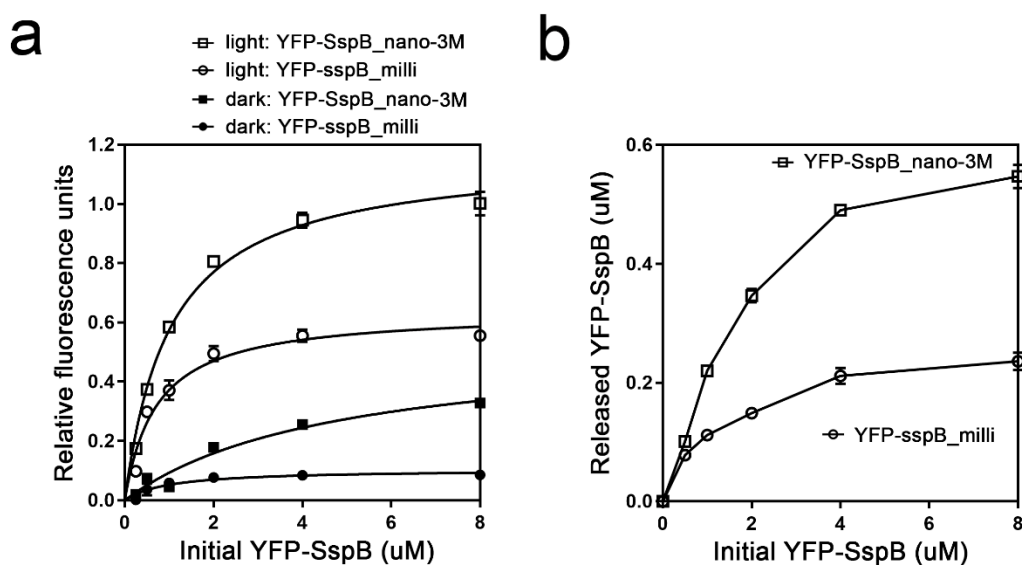
Figure 3.23 The binding affinity and releasing efficiency comparison.

(a). The fluorescence emission from membrane fractions after binding with SspB-YFP under dark or 20 min blue illumination. Fluorescence emission values were normalized with light-induced reaction under 8 μM YFP-SspB_nano-3M as 1 after subtraction of control emission values.

(b). The concentration of released YFP-SspB under dark for 30 min. Before releasing, the membrane fractions (from 5 mL *E. coli* media) were mixed with 4 μM YFP-SspB (in 300 μL buffer A) under 20 min light illumination. n = 3, error bars = SEM.

In the oocyte system, I discussed the time-dependent binding and releasing efficiency based on SspB_nano. And the results showed that 20 min was enough for precipitation as well as 30 min for release. However, due to the change from dimer to monomer, I then tested the time-dependent binding and releasing efficiency from SspB_nano-3M/H1021-iLID. As shown in Fig. 3.24a, after 10 min, the fluorescence in membrane fraction increased significantly. LOV domain is sensitive to blue illumination and long-time illumination could bleach this photoreceptor. Therefore, 10 min was chosen for the binding experiment. For protein releasing, it was also time-dependent and reached maximum efficiency after 30 min (Figure 3.24b).
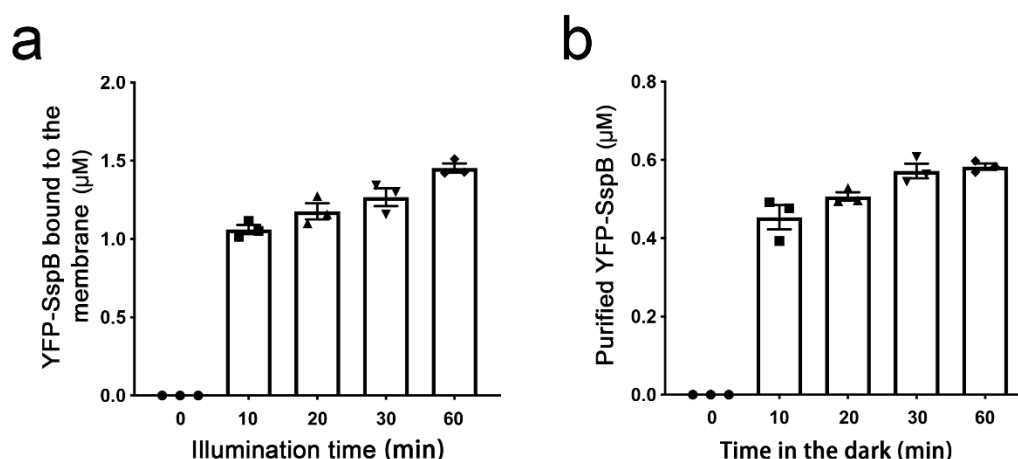
Figure 3.24 Time-dependent binding and releasing efficiency for SspB_nano-3M.

(a). Time-dependent binding efficiency between H1021-iLID and YFP-SspB_nano-3M under blue illumination. Each reaction contained 4 μM YFP-SspB (in 300 μL buffer A) and membrane fraction from 5 mL *E. coli*.

(b). Time-dependent release efficiency under 30 min dark from the H1021-iLID and YFP-SspB_nano-3M binding complex stimulated by 10 min blue light of (a).

Here, to separate the target protein from the supernatant of cell lysate, cell membrane fraction was used instead of traditional agarose beads. Compared to agarose beads, membrane fraction is easily harvested from *E. coli* or other cell types via ultrasonic disruption and centrifugation. The ligand (iLID) bonding to affinity tag (SspB) can also be widely anchored in the cell membrane by the membrane targeting signal. Besides H1021-iLID, membrane fractions from *E. coli* contain large amounts of other membrane proteins that could be released during the purification process, affecting the purity of the target protein. I then tested the effect of ion concentration, pH and temperature on protein purification (Figure 3.25). The sodium concentration ranging from 0 to 500 mM showed no significant effect on protein purification. When pH increased to 9.0, some membrane proteins became unstable and released from membrane fraction. In addition, low temperature decreased the binding affinity of iLID/SspB, contributing to the decrease of purification efficiency.

Figure 3.25 Purity identification under different conditions.

Purity identification under different conditions: ion concentration (0 to 500 mM NaCl), pH (6.8, 7.6 and 9.0) and temperature (0 °C and 24 °C). The purified samples were loaded in SDS-PAGE with same volume.
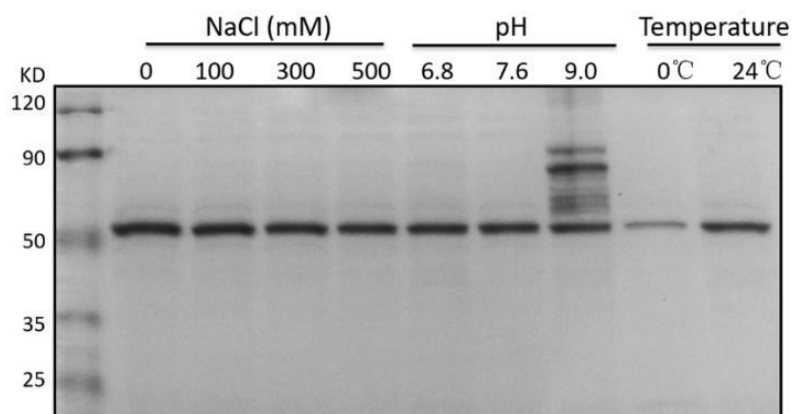
3.2.4 bPAC purification

bPAC is a photoactivated adenylyl cyclase composed of a blue light sensing (BLUF) domain and an adenylyl cyclase (AC) domain from the soil bacterium *Beggiatoa*. Because of low dark activity and high light activity, bPAC has become the most popular tool for cAMP manipulation. As the AC domain is only functional in a homodimer form, we first fused YFP-SspB_nano and YFP-SspB_nano-3M to the C-terminal of bPAC, respectively, and compared the effect on bPAC activity. After three days expression in *Xenopus* oocyte, the supernatant was extracted and dialyzed by using an ultra-centrifugal filter tube to remove the accumulated cAMP/cGMP. The turnover of bPAC-YFP-SspB_nano by light was then determined to be ~71 min^{-1} in buffer A, while for bPAC-YFP-SspB_nano-3M the turnover was ~116 min^{-1} (Figure 3.26a). SspB changed from dimer to monomer significantly increased bPAC activity. To purify bPAC-YFP-SspB_nano-3M, the soluble fraction from oocytes containing bPAC-YFP-SspB_nano-3M was mixed with H102-iLID from *E. coli* under blue light for binding within 2 min. After 1 min high-speed centrifugation, the soluble fraction was discarded. The sediment was washed three times, resuspended by 200 μL buffer A, and moved into dark condition for release within 30 min. After 30 min high-speed centrifugation at 4 °C, the supernatant was moved into a fresh tube and loaded in SDS-PAGE. As shown in Fig. 3.26b, bPAC-YFP-SspB_nano-3M (90 kDa) was in the supernatant as the dominant protein with over 90% purity. I further used western blot to check purified

bPAC-YFP-SspB_nano-3M (Figure 3.26c). In addition, the enzymatic activity of purified bPAC-YFP-SspB_nano-3M was also tested with the turnover of 130 min^{-1} (2.2 s^{-1}), which is close to the bPAC activity (2.6 s^{-1}) detected by Lindner et al. [113] and SUMO-bPAC activity (1.8 s^{-1}) detected by Stierl et al. [114] after purification (Figure 3.26d).
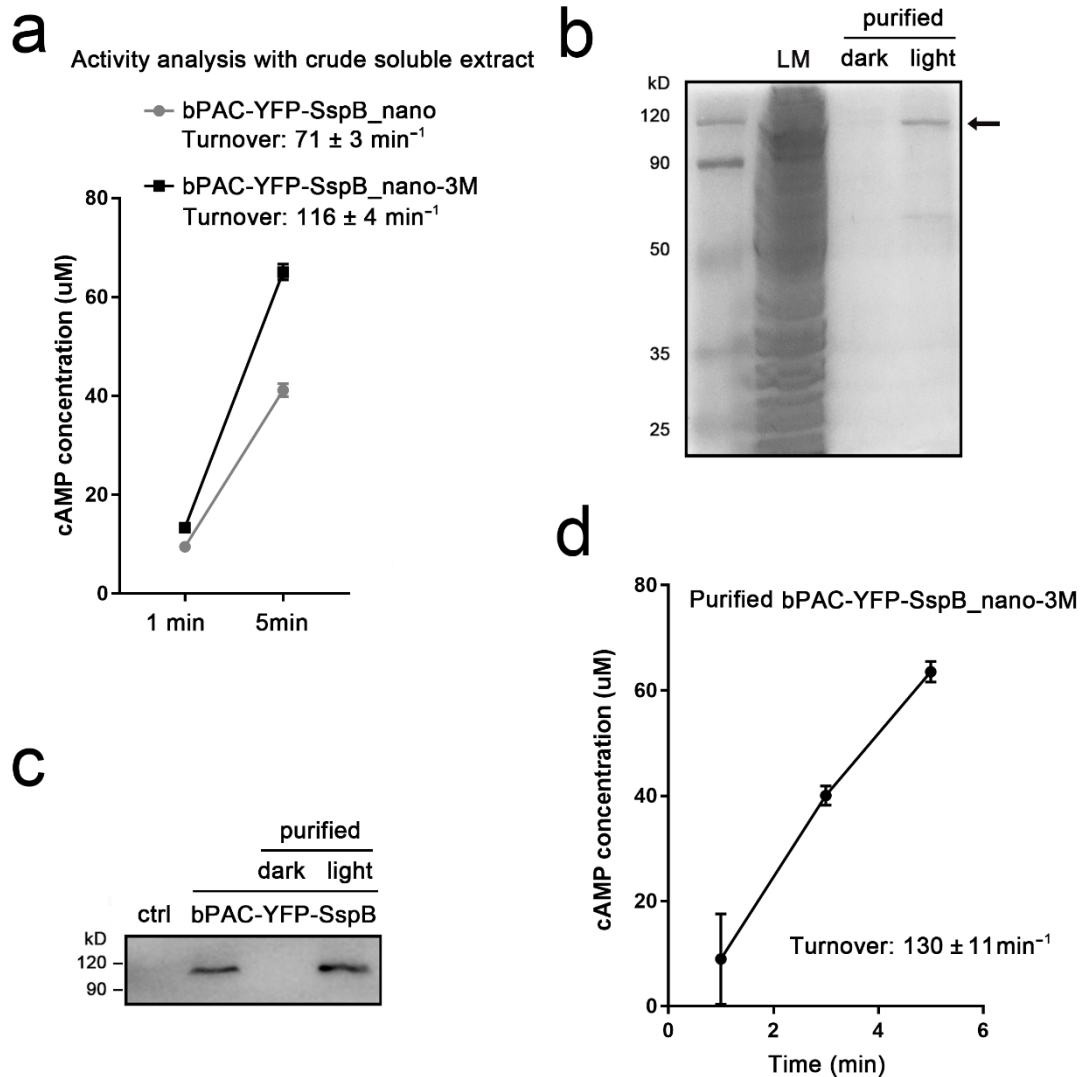
Figure 3.26 Evaluation of purified bPAC.

(a). bPAC activity comparison between different tags: SspB_nano (71 ± 3 min^{-1}) and SspB_nano-3M (116 ± 4 min^{-1}). 10 oocytes for each group were homogenized 3 dpi by 100 μL buffer A. 10 μL extraction was tested in each reaction under blue light (473 nm, 0.3 mW/mm^2).

(b). The purified bPAC with the tag of YFP-SspB_nano-3M was loaded in SDS-PAGE. 100 oocytes injected with bPAC-YFP-SspB_nano-3M were homogenized by 300 μL buffer A, and precipitated by 5 mL membrane fraction (H1021-iLID) from *E. coli*. Total: the lysed mixture from oocytes expressed bPAC-YFP-SspB_nano-3M. D: binding in the dark. L: binding in the light.

(c). Analysis of the cell lysed and purified bPAC by Western Blot using the antibody against YFP. ctrl: oocytes without injection.

(d) bPAC activity after purification: 130 ± 11 min^{-1}. n = 3, error bars = SEM.

3.2.5 DNA polymerase purification

DNA polymerase fused with SspB_nano-3M was overexpressed in *E. coli* BL21 (DE3). Buffer B (Tris-HCl 75 mM, KCl 300mM, MgCl$_2$ 2mM, DTT 5mM, pH 7.6) was used to harvest and disrupt the cells. Following 10 min high-speed centrifugation, the soluble fraction including DNA polymerase was mixed with H102-iLID under blue light for binding within 10 min. The mixture was then centrifuged to discard the soluble fraction. The sediment was washed three times, resuspended by 200 µL buffer B, and moved into dark condition for release within 30 min. After 30 min high-speed centrifugation at 4 °C, the supernatant was moved into a fresh tube. The purified SspB-tagged *Pfu*-Sso7d DNA polymerase from 50 mL culture was dialyzed extensively with buffer C (100 mM Tris-HCl pH 8.0, 0.2 mM EDTA, 0.2% NP-40, 0.2% Tween20, and 2 mM DTT) for activity analysis and storage. SDS-PAGE analysis of the purified protein showed the presence of the band, which corresponds to the estimated size of the 120 kDa (Figure 3.27a). In addition, the total amount of the purified DNA polymerase was 200 µL with 50% glycerol. The enzymatic activity of DNA polymerase was estimated based on the band intensity from PCR product of 1.1 kb fragment. Meanwhile, different amounts of purified DNA polymerase (2 µL, 1 µL and 0.5 µL) was tested and compared to 0.2 µL (2 U/µL) commercial Thermo Fisher Scientific Phusion DNA polymerase (Figure 3.27b). The relative intensity of PCR band using 1µL purified DNA polymerase was estimated to be close to 0.4 U Thermo Fisher Scientific Phusion DNA polymerase, suggesting that the enzymatic activity of purified DNA polymerase was estimated at 0.4 U/µL. In the end, an estimated 80 units of functional DNA polymerase were produced from a 50 mL culture.
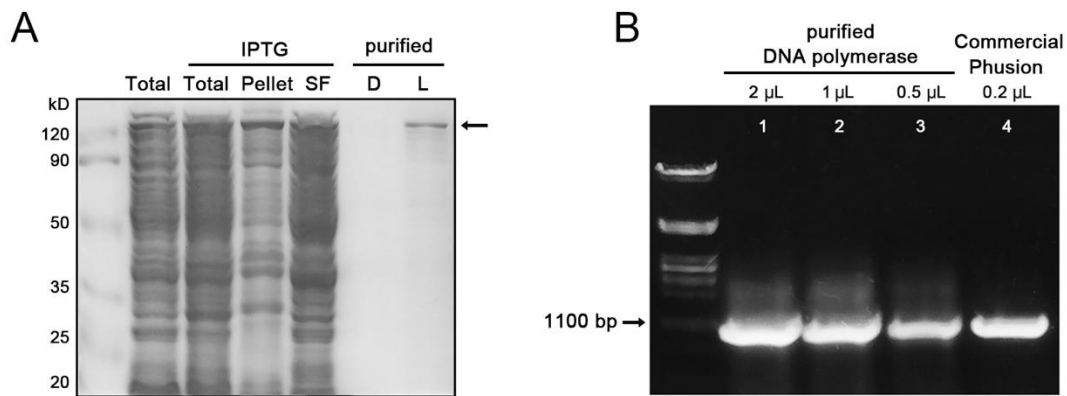
Figure 3.27 Evaluation of purified DNA polymerase.

(a). DNA polymerase tagged with SspB_nano-3M was expressed in *E. coli* induced by 0.5 mM IPTG. 50 mL media with cultured *E. coli* was washed and resuspended by 1 mL buffer A and 5 μL was mixed with loading buffer to run SDS-PAGE. The total amount of the purified DNA polymerase was 200 μL with 50% glycerol from 50 mL media and 20 μL was mixed with the loading buffer to run SDS-PAGE. Total: the whole cell lysed mixture after ultrasonic treatment. Pellet: sediment. SF: soluble fraction. D: the purified polymerase-SspB_nano-3M by dark. L: the purified polymerase-SspB_nano-3M by light.

(b). Gel electrophoresis of PCR products (1.1 kb fragment) by purified DNA polymerase (2 μL, 1 μL and 0.5 μL), compared with 0.2 μL (0.4 U) commercial Phusion DNA polymerase. The left lane is maker from Lambda DNA digested by PstI.

4 Discussion

4.1 New complexes for water transport regulation

As one of the most prevalent molecules in the biological system, water can transport through either AQPs or biological membranes directly in response to osmotic gradients, and AQPs expression can increase membrane water permeability by up to ~50 fold. Here, we co-assembled light-gated channels, including ChR2, GtACR1 and Sthk-bPAC, and AQP1 to form heteromultimeric water/ion channel complexes that generated osmotic gradient and then regulated transmembrane water flux.

$Xenopus$ oocyte system was used to express the complexes due to efficiency in expressing heterologous proteins for functional study, especially for the ion flux measurement of light-gated channels. In addition, the volume increase of $Xenopus$ oocyte in the hypotonic environment is easy to be observed due to water uptake, so that AQP1, as the first identified water channel, was characterized in $Xenopus$ oocyte by monitoring cell volume change [1]. In contrast to swelling, the shape of cell membrane becomes wrinkled in a hypertonic environment due to water loss, and then the vitelline membrane will be separated from cell membrane, which can be easily observed under microscopy. In our study, to evaluate water transport efficiency based on optogenetic tools and AQP1 assembled systems, we easily counted the number of broken oocytes as swelling due to water uptake and wrinkled oocytes as shrinking due to water loss.

To achieve highly regulated water transport through human body, AQPs are expressed and distributed in most tissues associated with diverse physiological and pathophysiological processes. It is now generally accepted that transcellular water flow regulation is accompanied by salt transport through ion channels in $vivo$. As shown in Fig. 4.1a, in response to hypotonicity-induced cell swelling, the swelling- activated K^+ channels, volume-regulated anion channels (VRACs) and K^+-Cl^- co-transporters (KCCs) allow efflux of K^+/Cl^- from the cell and subsequent water loss by osmosis either through AQPs or directly through the lipid bilayer. On the other hand, in response to hypertonicity-induced cell shrinkage, Na^+-H^+ exchangers, Na^+-K^+-$2Cl^-$ co-transporters (NKCCs) and some non-selective cation channels (NSCCs) induce influx of Na^+/Cl^- in cellular and subsequent water uptake to recover cell volume (Figure 4.1b). To sum up, water transport regulation in $vivo$ is mainly based on the cooperation of channels to form Na^+/Cl^- influx or K^+/Cl^- efflux. Our results from $Xenopus$ oocyte also confirmed

that water transport through AQP1 induced by the complex of XXM2.0-β-GtACR1 or GtACR1-SthK-bPAC is more efficient than that induced by a single channel. In fact, the osmotic gradient formation only by Na^+ or K^+ channel is restricted by the ion concentration between the intracellular and extracellular. Whereas co-expressing GtACR1 with XXM2.0 or SthK-bPAC could break this restriction. On the one hand, the movement of Cl^- via GtACR1 following Na^+ or K^+ flux could further increase the osmotic gradient. In addition, Cl^- flux could change the membrane potential in reverse, which will further stimulate Na^+ or K^+ flux. To sum up, if the complexes of XXM2.0-β-GtACR1 or GtACR1-SthK-bPAC are expressed *in vivo*, water transport could be regulated by light to maintain cytoplasm isotonic relative to the environment.
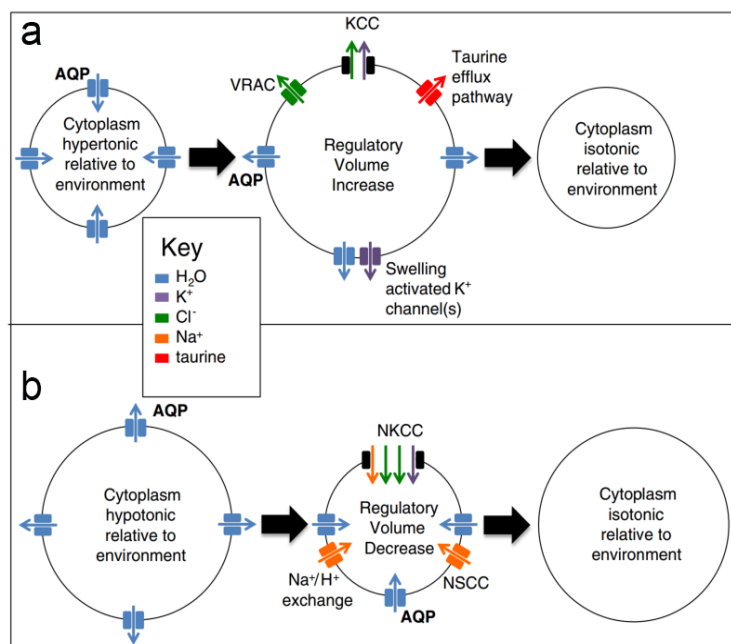
Figure 4.1 Solute transport pathways mediating cell volume regulation.

(a). Regulatory volume decreases. KCC: potassium chlorine cotransporter; VRAC: volume regulated anion channel.

(b). Regulatory volume increases. NKCC: sodium potassium chlorine cotransporter; NSCC: non-selective cation channel. Taken from [115].

For water transport efficiency, the oocytes exhibited swelling or shrinking slowly even under more than 20 min illumination. It was limited to the flowing of NaCl or KCl between *Xenopus* oocyte and outside buffer. The amount of NaCl, flowing into oocyte during swelling in ND96 buffer through XXM2.0 and GtACR1, can be calculated by Faraday's laws:

$$n = It/(Fv)$$

(I: the constant current, 1 μA; t: the total time; F: Faraday constant, 9.6485×10^4 C/mol; v: the valency of the ions, 1). Then n is 6.22×10^{-10} mol per min. The volume for an oocyte can be calculated by the formula:

$$V = (4/3)\,\pi r^3$$

(r: the radius of an oocyte, 0.6 mm; π: 3.14). Then V is 0.9 μL. Here, we assume that the certain inward current is 1 μA, and the radius of an oocyte is 0.6 mm. The concentration of NaCl in an oocyte will then increase 0.691 mM/min. 20 min later, NaCl concentration in an oocyte could only increase 13.82 mM, determining the swelling efficiency.

If the light-gated channels are expressed in mammalian cells, like HEK293 or HeLa cells, the shape changes or migration could be observed under illumination. As shown in Fig. 4.2a, AQPs participate in the protrusion formation based on actin polymerization that drives cell migration [116-118]. Comparing to the single expression of AQP in cells, the complex of XXM2.0-β-GtACR1 and AQP1 could regulate actin polymerization by light, which is more flexible and precise to control filopodia or lamellipodia formation. For cell shrinkage, chromatin condensation and membrane blebs could initiate the formation of apoptotic bodies, which are eventually engulfed by macrophages or neighboring cells through endocytosis/phagocytosis (Figure 4.2b) [119]. This suggests that the complex of GtACR1-SthK-bPAC can also be used to induce program cell death, such as apoptosis.
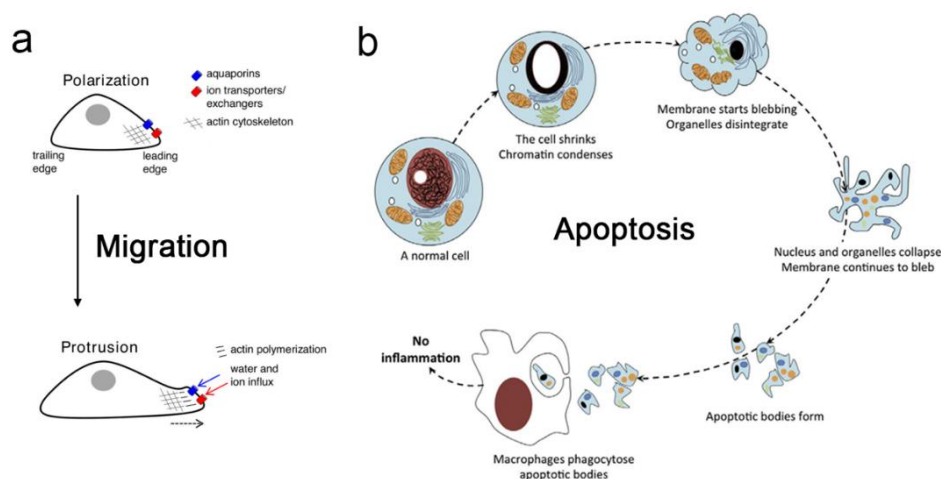

Figure 4.2 Aquaporins in cell migration.

(a). The redistribution of aquaporins, ion transporters/exchangers, and actin polymerization machinery to the leading edge before cell movement. Later, protrusions of the membrane were

formed via water/ion influx and actin polymerization beneath the plasma membrane to push the membrane forward. Modified from [117].

(b). The different stages of apoptosis start with cellular shrinkage and chromatin condensation. Taken from [119].

4.2 Membrane fraction from *E. coli* as protein purification platform

iLID, as a light-induced dimer, is widely used to regulate cell signaling and protein expression. The new application of iLID in our study was protein purification. We found that membrane fraction anchored with iLID from *E. coli* could be used to precipitate SspB-tagged protein from soluble fraction. The application of membrane fraction was easier than beads used by Hörner et al. [120] or Carrasco-López et al. [121] to combine photoreceptors for light-controlled protein purification, and it also has some other advantages. First, *E. coli* contains the inner membrane and outer membrane, and both tend to form stable vesicles after disruption by sonication, which are native platforms for the characterization of folding, structure and function of membrane proteins [122]. We changed the buffer condition to harvest membrane vesicles and further confirmed that the membrane vesicles are stable as protein purification platforms when the conditions including NaCl concentration, temperature and pH value were changed in a wide range (Figure 3.25). This advantage allows us to purify DNA polymerase with 300 mM KCl but 100 mM NaCl for bPAC. Meanwhile, to keep the enzymatic activity of bPAC, the binding and releasing process can be operated on ice. Second, because the weight of inner membrane vesicle or outer membrane vesicle is between soluble fraction and cell debris, we used two-step centrifugation to harvest these membrane vesicles. The first low-speed (~500 g) centrifugation was used to centrifuge down the cell debris. A second-high speed (~10000 g) centrifugation was used to centrifuge down the membrane vesicles. Therefore, we can easily harvest large amounts of membrane vesicles within a short time. Third, before precipitation, the unstable protein binding directly or indirectly to the membrane vesicles can be washed to decrease the unwanted proteins during target protein release.

4.3 *In vitro* assay the binding and dissociation of iLID

The binding or dissociation between SspB_nano and iLID is fast within several minutes in cells. To evaluate the binding and dissociation efficiency in a buffer system, we first expressed iLID and SspB_nano in *Xenopus* oocyte. We used *Xenopus* oocyte because

it is efficiently expressed heterologous proteins for functional study, and easy to separate soluble fraction and membrane fraction (Figure 2.2). During the binding period, we observed strong (more than 50% binding efficiency) and fast (within 10 min) interaction between SspB_nano and iLID in response to blue light (Figure 3.15c and d). Meanwhile, we used *E. coli* to repeat the time-dependent binding efficiency and further confirmed the interaction between SspB_nano and iLID (Figure 3.19). However, SspB_nano exhibited low dissociation efficiency in both *Xenopus* oocyte and *E. coli* systems. When we used SDS-PAGE to check the released SspB_nano, no significant band could be observed. As reported by Liu Qi et al. [123], SspB_nano binds with high affinity to iLID in HEK293 cells, even in the dark. Therefore, they used SspB_milli instead of SspB_nano, which resulted in robust light-dark differences. But for hippocampal neurons, due to low expression level, SspB_micro is better than SspB_milli to regulate split protein assembly. When we compared SspB_nano, SspB_micro and SspB_milli in *E. coli*, only SspB_milli exhibited significant dissociation due to lower dark activity. Therefore, when we apply iLID in different systems, we should consider the appropriate variant of SspB to keep light activity and decrease dark activity.

4.4 SspB optimization from dimer to monomer

Although iLID is a powerful optogenetic tool, one problem has been ignored that SspB is easy to form the homodimer. McGinness et al. [98] first introduced eight mutations in the N-terminal α helix of SspB_nano (SspB_nano-8M) to inhibit dimer formation, which is about 3-fold weaker than SspB_nano to bind with SsrA due to the slightly hydrophobic groove distortion in SspB_nano-8M. However, our results found that the binding affinity between SspB_nano-8M and iLID was too low to be used for protein precipitation (Figure 3.21f). The possible reason is that SsrA fused to iLID has been truncated from 11 to 8 amino acids, which could affect the binding with iLID. Meanwhile, the C-terminal phenylalanine in iLID contributes to ~10-fold affinity decrease according to the comparison between starting LOV-SsrA (no phenylalanine) and oLID (with phenylalanine) [95]. We also truncated the total N-terminal α helix of SspB, and the truncated SspB_nano cannot bond with SsrA at all. These suggest that the α helix of SspB participates in dimer formation, and contributes to the hydrophobic interaction to keep the stability of SspB. To solve this problem, we designed a new mutant by introducing only three mutations to SspB_nano (SspB_nano-3M) that

exhibited a hundred percent of the monomeric state in native-PAGE (Figure 3.21g). In addition, the L/D ratio of SspB_nano-3M is higher than SspB_nano and SspB_milli *in vitro*, so that SspB_nano-3M can also be used as a tag for protein purification. Furthermore, compared to SspB dimer, SspB monomer has less effect on the target protein activity when we compared bPAC activity fused with dimeric and monomeric SspB.

4.5 Fast and mild pathway for protein purification

The most common protein purification method is based on affinity chromatography, which requires different chromatography columns. This method also requires harsh conditions like acidic pH 4.5 - 6 and/or adding imidazole or high salt concentration, to elute and collect the purified proteins. The conditional change could influence the activity of target protein. The light-controlled protein pathway is easy and flexible based on iLID-SspB, which regulates protein binding with light in mild conditions and does not require solution change for elution. The plasma membrane fraction and the soluble cytosolic fraction from *E. coli* can be easily separated by centrifugation. The SspB-POI can be then captured to the membrane fraction with light and released to clean buffer in the dark after washing. This method does not require any specific column and functions in mild conditions, which are very flexible at scale and will facilitate extensive protein engineering and purification of proteins sensitive to buffer conditions. Besides DNA polymerase purification from *E. coli*, this purification system can also purify soluble proteins from *Xenopus* oocyte, HEK cell or other expression systems.

Though different kinds of DNA polymerases have been cloned and purified during the past two decades, the cost of DNA polymerase is also astonishing to some labs that need to do large amounts of PCR. Here, our DNA polymerase purification method can be easily used for large-scale purification in many labs and companies without a need for expensive equipment and skilled biochemical techniques. This can interest many laboratories and companies that hope to make their own DNA polymerase for PCR assays.

5 Reference

1. Preston, G.M., et al., Appearance of Water Channels in Xenopus Oocytes Expressing Red Cell CHIP28 Protein, Science, 1992. 256: p. 385-387.
2. Verkman, A.S., Mammalian aquaporins: diverse physiological roles and potential clinical significance, Expert Rev Mol Med, 2008. 10: p. e13.
3. Rojek, A., et al., A current view of the mammalian aquaglyceroporins, Annu Rev Physiol, 2008. 70: p. 301-27.
4. King, L.S., et al., From structure to disease: the evolving tale of aquaporin biology, Nat Rev Mol Cell Biol, 2004. 5(9): p. 687-98.
5. Papadopoulos, M.C. and Verkman, A.S., Aquaporin water channels in the nervous system, Nat Rev Neurosci, 2013. 14(4): p. 265-77.
6. Kozono, D., et al., Aquaporin water channels: atomic structure molecular dynamics meet clinical medicine, J Clin Invest, 2002. 109(11): p. 1395-9.
7. Yang, B., et al., The Mercurial Insensitive Water Channel (AQP-4) Forms Orthogonal Arrays in Stably Transfected Chinese Hamster Ovary Cells, 1996. 271(1): p. 4577-4580.
8. Verkman, A.S., et al., Aquaporins: important but elusive drug targets, Nat Rev Drug Discov, 2014. 13(4): p. 259-77.
9. Finn, R.N. and Cerda, J., Evolution and Functional Diversity of Aquaporins, Biol. Bull, 2018. 229: p. 6-23.
10. Zelenina, M., et al., Prostaglandin E2 interaction with AVP: effects on AQP2 phosphorylation and distribution, Am J Physiol Renal Physiol, 2000. 278: p. F388-F394.
11. Yukutake, Y. and Yasui, M., Regulation of water permeability through aquaporin-4, Neuroscience, 2010. 168(4): p. 885-91.
12. Dibas, A., et al., Changes in ocular aquaporin-4 (AQP4) expression following retinal injury, Molecular Vision, 2008. 14: p. 1770-1783.
13. Blanc, L., et al., The water channel aquaporin-1 partitions into exosomes during reticulocyte maturation: implication for the regulation of cell volume, Blood, 2009. 114(18): p. 3928-34.
14. Tamma, G., et al., Glutathionylation of the aquaporin-2 water channel: a novel post-translational modification modulated by the oxidative stress, J Biol Chem, 2014. 289(40): p. 27807-13.
15. Kreida, S., et al., Protein-protein interactions in AQP regulation - biophysical characterization of AQP0-CaM and AQP2-LIP5 complex formation, Faraday Discuss, 2018. 209(0): p. 35-54.
16. Reichow, S.L., et al., Allosteric mechanism of water-channel gating by Ca^{2+}-calmodulin, Nat Struct Mol Biol, 2013. 20(9): p. 1085-92.
17. van Balkom, B.W., et al., LIP5 interacts with aquaporin-2 and facilitates its lysosomal degradation, J Am Soc Nephrol, 2009. 20(5): p. 990-1001.
18. Stokum, J.A., et al., SUR1-TRPM4 and AQP4 form a heteromultimeric complex that amplifies ion/water osmotic coupling and drives astrocyte swelling, Glia, 2018. 66(1): p. 108-125.
19. Woo, S.K., et al., The sulfonylurea receptor 1 (Sur1)-transient receptor potential melastatin 4 (Trpm4) channel, J Biol Chem, 2013. 288(5): p. 3655-67.
20. van den Bos, E.J., et al., A novel model of cryoinjury-induced myocardial infarction in the mouse: a comparison with coronary artery ligation, Am J Physiol Heart Circ Physiol, 2005. 289(3): p. H1291.
21. Baumgart, F., et al., Light inactivation of water transport and protein–protein interactions of aquaporin–Killer Red chimeras, J Gen Physiol, 2011. 139(1): p. 83-90.
22. Schneider, F., et al., Biophysics of Channelrhodopsin, Annu Rev Biophys, 2015. 44: p. 167-86.
23. Zhang, F., et al., The microbial opsin family of optogenetic tools, Cell, 2011. 147(7): p. 1446-57.
24. Oesterhelt, D. and Stoeckenius, W., Rhodopsin-like Protein from the Purple Membrane of *Halobacterium halobium*, Nature New Biology, 1971. 233: p. 149-152.
25. Oesterhelt, D. and Stoeckenius, W., Functions of a New Photoreceptor Membrane, PNAS, 1973. 70(10): p. 2853-2857.

26. Chow, B.Y., et al., High-performance genetically targetable optical neural silencing by light-driven proton pumps, Nature, 2010. 463(7277): p. 98-102.

27. Gradinaru, V., et al., Molecular and cellular approaches for diversifying and extending optogenetics, Cell, 2010. 141(1): p. 154-165.

28. Inoue, K., et al., A light-driven sodium ion pump in marine bacteria, Nat Commun, 2013. 4: p. 1678.

29. Grimm, C., et al., Electrical properties, substrate specificity and optogenetic potential of the engineered light-driven sodium pump eKR2, Sci Rep, 2018. 8(1): p. 9316.

30. Nagel, G., et al., Channelrhodopsin-1: A Light-Gated Proton Channel in Green Algae, Science, 2002. 296: p. 2395-2398.

31. Nagel, G., et al., Channelrhodopsin-2, a directly light-gated cation-selective membrane channel, PNAS, 2003. 100(24): p. 13940-5.

32. Nagel, G., et al., Light activation of channelrhodopsin-2 in excitable cells of Caenorhabditis elegans triggers rapid behavioral responses, Curr Biol, 2005. 15(24): p. 2279-84.

33. Boyden, E.S., et al., Millisecond-timescale, genetically targeted optical control of neural activity, Nat Neurosci, 2005. 8(9): p. 1263-8.

34. Berndt, A., et al., Bi-stable neural state switches, Nat Neurosci, 2009. 12(2): p. 229-34.

35. Dawydow, A., et al., Channelrhodopsin-2-XXL, a powerful optogenetic tool for low-light applications, PNAS, 2014. 111(38): p. 13972-7.

36. Duan, X., et al., Mutated Channelrhodopsins with Increased Sodium and Calcium Permeability, Applied Sciences, 2019. 9(4): p. 664.

37. Wietek, J., et al., Conversion of Channelrhodopsin into a Light-Gated Chloride Channel, Science, 2014. 344: p. 409-412.

38. Govorunova, E.G., et al., Natural light-gated anion channels: A family of microbial rhodopsins for advanced optogenetics, Science, 2015. 349(6248): p. 647-650.

39. Mohamed, G.A., et al., Optical inhibition of larval zebrafish behaviour with anion channelrhodopsins, BMC Biol, 2017. 15(1): p. 103.

40. Mauss, A.S., et al., Optogenetic Neuronal Silencing in Drosophila during Visual Processing, Sci Rep, 2017. 7(1): p. 13823.

41. Mahn, M., et al., High-efficiency optogenetic silencing with soma-targeted anion-conducting channelrhodopsins, Nat Commun, 2018. 9(1): p. 4125.

42. Messier, J.E., et al., Targeting light-gated chloride channels to neuronal somatodendritic domain reduces their excitatory effect in the axon, Elife, 2018. 7.

43. Kleinlogel, S., et al., A gene-fusion strategy for stoichiometric and co-localized expression of light-gated membrane proteins, Nat Methods, 2011. 8(12): p. 1083-8.

44. Avelar, G.M., et al., A rhodopsin-guanylyl cyclase gene fusion functions in visual perception in a fungus, Curr Biol, 2014. 24(11): p. 1234-40.

45. Gao, S., et al., Optogenetic manipulation of cGMP in cells and animals by the tightly light-regulated guanylyl-cyclase opsin CyclOp, Nat Commun, 2015. 6: p. 8046.

46. Scheib, U., et al., The rhodopsin–guanylyl cyclase of the aquatic fungus Blastocladiella emersonii enables fast optical control of cGMP signaling, 2015. 8(389).

47. Tian, Y., et al., A novel rhodopsin phosphodiesterase from Salpingoeca rosetta shows light-enhanced substrate affinity, Biochem J, 2018. 475(6): p. 1121-1128.

48. Tian, Y., et al., Two-component cyclase opsins of green algae are ATP-dependent and light-inhibited guanylyl cyclases, BMC Biol, 2018. 16(1): p. 144.

49. Fegan, A., et al., Chemically Controlled Protein Assembly- Techniques and Applications, Chem Rev, 2010. 110: p. 3315-3336.

50. Rivera, V.M., et al., A humanized system for pharmacologic control of gene expression, Nature, 1996. 2(9): p. 1028-1032.

51. Quail, P.H., Phytochrome photosensory signaling networks, Nat Rev Mol Cell Biol, 2002. 3(2): p. 85-93.

52. Burgie, E.S. and Vierstra, R.D., Phytochromes: an atomic perspective on photoactivation and signaling, Plant Cell, 2014. 26(12): p. 4568-83.

53. Fankhauser, C., The phytochromes, a family of red/far-red absorbing photoreceptors, J Biol Chem, 2001. 276(15): p. 11453-6.

54. Rockwell, N.C., et al., Phytochrome structure and signaling mechanisms, Annu Rev Plant Biol, 2006. 57: p. 837-58.

55.   Butler, W.L., et al., Detection, assay, and preliminary purification of the pigment controlling photoresponsive development of plants, PNAS, 1959. 45: p. 1703-1708.

56.   Burgie, E.S., et al., Crystal structure of the photosensing module from a red/far-red light-absorbing plant phytochrome, PNAS, 2014. 111(28): p. 10179-84.

57.   Chernov, K.G., et al., Near-Infrared Fluorescent Proteins, Biosensors, and Optogenetic Tools Engineered from Phytochromes, Chem Rev, 2017. 117(9): p. 6423-6446.

58.   Ni, M., et al., PIF3, a Phytochrome-Interacting Factor Necessary for Normal Photoinduced Signal Transduction, Is a Novel Basic Helix-Loop-Helix Protein, Cell, 1998. 95: p. 657-667.

59.   Ni, M., et al., Binding of phytochrome B to its nuclear signaling partner PIF3 is reversibly induced by light, Nature, 1999. 400: p. 781-4.

60.   Shimizu-S, S., et al., A light-switchable gene promoter system, Nat Biotech, 2002. 20(10): p. 1041.

61.   Tyszkiewicz, A.B. and Muir, T.W., Activation of protein splicing with light in yeast, Nat Methods, 2008. 5(4): p. 303-5.

62.   Leung, D.W., et al., Genetically encoded photoswitching of actin assembly through the Cdc42-WASP-Arp2/3 complex pathway, PNAS, 2008. 105(35): p. 12797-802.

63.   Levskaya, A., et al., Spatiotemporal control of cell signaling using a light-switchable protein interaction, Nature, 2009. 461(7266): p. 997-1001.

64.   Uda, Y., et al., Efficient synthesis of phycocyanobilin in mammalian cells for optogenetic control of cell signaling, PNAS, 2017. 114(45): p. 11962-11967.

65.   Kaberniuk, A.A., et al., A bacterial phytochrome-based optogenetic system controllable with near-infrared light, Nat Methods, 2016. 13(7): p. 591-7.

66.   Beyer, H.M., et al., Red Light-Regulated Reversible Nuclear Localization of Proteins in Mammalian Cells and Zebrafish, ACS Synth Biol, 2015. 4(9): p. 951-8.

67.   Toettcher, J.E., et al., Light-based feedback for controlling intracellular signaling dynamics, Nat Methods, 2011. 8(10): p. 837-9.

68.   Milias-Argeitis, A., et al., In silico feedback for in vivo regulation of a gene expression circuit, Nat Biotechnol, 2011. 29(12): p. 1114-6.

69.   Ruess, J., et al., Iterative experiment design guides the characterization of a light-inducible gene expression circuit, PNAS, 2015. 112(26): p. 8148-53.

70.   Ahmad, M. and Cashmore, A.R., HY4 gene of A. thaliana encodes a protein with characteristics of a blue-light photoreceptor, Nature, 1993. 366: p. 162-166.

71.   Lin, C., et al., Expression of an Arabidopsis cryptochrome gene in transgenic tobacco results in hypersensitivity to blue, UV-A, and green light, PNAS, 1995. 92: p. 8423-7.

72.   Lin, C., et al., Association of Flavin Adenine Dinucleotide with the Arabidopsis Blue Light Receptor CRY1, Science, 1995. 269: p. 968-970.

73.   Lin, C., et al., Enhancement of blue-light sensitivity of Arabidopsis seedlings by a blue light receptor cryptochrome 2, PNAS, 1998. 95: p. 2686-2690.

74.   Sang, Y., et al., N-terminal domain-mediated homodimerization is required for photoreceptor activity of Arabidopsis CRYPTOCHROME 1, Plant Cell, 2005. 17(5): p. 1569-84.

75.   Liu, B., et al., Searching for a photocycle of the cryptochrome photoreceptors, Curr Opin Plant Biol, 2010. 13(5): p. 578-86.

76.   Liu, H., et al., The action mechanisms of plant cryptochromes, Trends Plant Sci, 2011. 16(12): p. 684.

77.   Liu, H., et al., Photoexcited CRY2 Interacts with CIB1 to Regulate Transcription and Floral Initiation in Arabidopsis, Science, 2008. 322: p. 1535-9.

78.   Kennedy, M.J., et al., Rapid blue-light–mediated induction of protein interactions in living cells, Nat Methods, 2010. 7(12): p. 973-975.

79.   Bugaj, L.J., et al., Optogenetic protein clustering and signaling activation in mammalian cells, Nat Methods, 2013. 10(3): p. 249-52.

80.   Bugaj, L.J., et al., Regulation of endogenous transmembrane receptors through optogenetic Cry2 clustering, Nat Commun, 2015. 6: p. 6898.

81.   Das, S., et al., Single molecule tracking of small GTPase Rac1 uncovers spatial regulation of membrane translocation and mechanism for polarized signaling, PNAS, 2015. 112(3): p. E267-76.

82. Polstein, L.R. and Gersbach, C.A., A light-inducible CRISPR-Cas9 system for control of endogenous gene activation, Nat Chem Biol, 2015. 11(3): p. 198-200.

83. Idevall-Hagren, O., et al., Optogenetic control of phosphoinositide metabolism, PNAS, 2012. 109(35): p. E2316-23.

84. Nguyen, M.K., et al., Optogenetic oligomerization of rab GTPases regulates intracellular membrane trafficking, Nature Chemical Biology, 2016. 12(6): p. 431-6.

85. van Bergeijk, P., et al., Optogenetic control of organelle transport and positioning, Nature, 2015. 518(7537): p. 111-114.

86. Briggs, W.R. and Christensen, J.M., Phototropins 1 and 2- versatile plant blue-light receptors, TRENDS in Plant Science, 2002. 7(5): p. 204-210.

87. Tokutomi, S., et al., Molecular structure and regulation of phototropin kinase by blue light, BBA, 2008. 1784(1): p. 133-42.

88. Harper, S.M., et al., Structural Basis of a Phototropin Light Switch, Science, 2003. 301: p. 1541-4.

89. Strickland, D., et al., Light-activated DNA binding in a designed allosteric protein, PNAS, 2008. 105: p. 10709-14.

90. Lee, J., et al., Surface Sites for Engineering Allosteric Control in Proteins, Science, 2008. 322: p. 438-442.

91. Wu, Y.I., et al., A genetically encoded photoactivatable Rac controls the motility of living cells, Nature, 2009. 461(7260): p. 104-8.

92. Mills, E., et al., Engineering a photoactivated caspase-7 for rapid induction of apoptosis, ACS Synth Biol, 2012. 1(3): p. 75-82.

93. Strickland, D., et al., TULIPs: tunable, light-controlled interacting protein tags for cell biology, Nat Methods, 2012. 9(4): p. 379-84.

94. Huang, J., et al., Structural basis for exquisite specificity of affinity clamps, synthetic binding proteins generated through directed domain-interface evolution, J Mol Biol, 2009. 392(5): p. 1221-31.

95. Guntas, G., et al., Engineering an improved light-induced dimer (iLID) for controlling the localization and activity of signaling proteins, PNAS, 2015. 112(1): p. 112-7.

96. Hersch, G.L., et al., SspB delivery of substrates for ClpXP proteolysis probed by the design of improved degradation tags, PNAS, 2004. 101(33): p. 12136-12141.

97. Song, H.K. and Eck, M.J., Structural Basis of Degradation Signal Recognition by SspB, a Specificity-Enhancing Factor for the ClpXP Proteolytic Machine, Molecular Cell, 2003. 12(1): p. 75-86.

98. McGinness, K.E., et al., Altered tethering of the SspB adaptor to the ClpXP protease causes changes in substrate delivery, J Biol Chem, 2007. 282(15): p. 11465-73.

99. Lungu, O.I., et al., Designing photoswitchable peptides using the AsLOV2 domain, Chem Biol, 2012. 19(4): p. 507-17.

100. Zimmerman, S.P., et al., Tuning the Binding Affinities and Reversion Kinetics of a Light Inducible Dimer Allows Control of Transmembrane Protein Localization, Biochemistry, 2016. 55(37): p. 5264-71.

101. Wang, H., et al., LOVTRAP: an optogenetic system for photoinduced protein dissociation, Nat Methods, 2016. 13(9): p. 755-8.

102. Heintzen, C., et al., The PAS Protein VIVID Defines a Clock-Associated Feedback Loop that Represses Light Input, Modulates Gating, and Regulates Clock Resetting, Cell, 2001. 104: p. 453-464.

103. Zoltowski, B.D., et al., Conformational Switching in the Fungal Light Sensor Vivid, Science, 2007. 316: p. 1054-7.

104. Wang, X., et al., Spatiotemporal control of gene expression by a light-switchable transgene system, Nat Methods, 2012. 9(3): p. 266-9.

105. Nihongaki, Y., et al., Genetically engineered photoinducible homodimerization system with improved dimer-forming efficiency, ACS Chem Biol, 2014. 9(3): p. 617-21.

106. Kawano, F., et al., Engineered pairs of distinct photoswitches for optogenetic control of cellular proteins, Nat Commun, 2015. 6: p. 6256.

107. Weber, W., Ion currents of *Xenopus laevis* oocytes: state of the art, BBA, 1999. 1421: p. 213-233.

108. Stegen, C., et al., Swelling-induced taurine release without chloride channel activity in *Xenopus laevis* oocytes expressing anion channels and transporters, BBA, 2000. 1467: p. 91-100.

109. Wang, Y., et al., 2A self-cleaving peptide-based multi-gene expression system in the silkworm *Bombyx mori*, Sci Rep, 2015. 5: p. 16273.

110. Beck, S., et al., Synthetic Light-Activated Ion Channels for Optogenetic Activation and Inhibition, Front Neurosci, 2018. 12: p. 643.

111. Shepard, B.D., et al., A cleavable N-terminal signal peptide promotes widespread olfactory receptor surface expression in HEK293T cells, PLoS One, 2013. 8(7): p. e68758.

112. Nenninger, A., et al., Independent mobility of proteins and lipids in the plasma membrane of Escherichia coli, Mol Microbiol, 2014. 92(5): p. 1142-53.

113. Lindner, R., et al., Photoactivation Mechanism of a Bacterial Light-Regulated Adenylyl Cyclase, J Mol Biol, 2017. 429(9): p. 1336-1351.

114. Stierl, M., et al., Light modulation of cellular cAMP by a small bacterial photoactivated adenylyl cyclase, bPAC, of the soil bacterium Beggiatoa, J Biol Chem, 2011. 286(2): p. 1181-8.

115. Day RE., et al., Human aquaporins: regulators of transcellular water flow, BBA. 2013. 1840(5): 1492-506.

116. Papadopoulos, M.C., et al., Aquaporins and cell migration, Pflugers Arch, 2008. 456(4): p. 693-700.

117. De Ieso, M.L. and Yool, A.J., Mechanisms of Aquaporin-Facilitated Cancer Invasion and Metastasis, Front Chem, 2018. 6: p. 135.

118. McLennan, R., et al., Neural crest cells bulldoze through the microenvironment using Aquaporin 1 to stabilize filopodia, Development, 2020. 147(1).

119. Abou-Ghali, M. and Stiban, J., Regulation of ceramide channel formation and disassembly: Insights on the initiation of apoptosis, Saudi J Biol Sci, 2015. 22(6): p. 760-72.

120. Horner, M., et al., Light-Controlled Affinity Purification of Protein Complexes Exemplified by the Resting ZAP70 Interactome, Front Immunol, 2019. 10: p. 226.

121. Carrasco-López, C., et al., Development of light-responsive protein binding in the monobody non-immunoglobulin scaffold, Nat Commun, 2020. 11(1).

122. Sueki, A., et al., Systematic Localization of Escherichia coli Membrane Proteins, mSystems, 2020. 5(2): p. e00808-19.

123. Liu, Q., et al., A Photoactivatable Botulinum Neurotoxin for Inducible Control of Neurotransmission, Neuron, 2019. 101(5): p. 863-875 e6.

6 Appendix

6.1 Supplement Table

Table S1. List of primers used in this study

β linker BH5F	TAGGATCCATGGCAGCCCTG CAGGAGAAGAAG	For constructs with β linker
β linker BglXb3R	TGCTCTAGAAGATCTGGAGC TGTTTTCAGAGATGTTG	For constructs with β linker
H1021 Bh5F	CGGGATCCGCCACGATGGG CAGCCCGCTGCGTTTCTTTC CGGTCGTGATCATTGCGGTA ATCTTTTTGATTCTGGTGAC CATCTTCCTCTATACCCGCT	For constructs with H1021
H1021 Xh3R	CTCCGCTCGAGTGCCATGGC AGATCTCGCTGATCCGTTAT TATTGTTGTTCGCTTCATTGT TCGGCGCAATAACATAAAA GCGGGTATAGAGGAAGATG	For constructs with H1021
SspB A58V F	GCCAGCGTCACAGGCAATCT CCAACT	For SspB mutation
SspB A58V R	GCCTGTGACGCTGGCACTCA AATTGA	For SspB mutation
SspB R73Q F	TCAATGCACAATTTAAAGGC GTTAGCA	For SspB mutation
SspB R73Q R	CCTTTAAATTGTGCATTGAA TTGTATG	For SspB mutation
SspB 3M Xh5F	CCGCTCGAGGCAGCTGCTGG AGCTCCAGCTCGTCCACTGG TACTGCGTGCTTATTATGAC TGGTTGGTAGA	For SspB mutation
SspB 3AM Xh5F	CCGCTCGAGGCAGCTGCTGG AGCTCCAGCTCGTCCAGCAG CTCTGCGTGCTTATTATGAC TGGTTGGTAGA	For SspB mutation
SspB 8M Xh5F	CACCGCTCGAGGGATCCATG GCACGCTCTCCAGAGCGTCC ACAGAAGCTCCGTGAGAAG TATGATGAGTTGGTAAAGA ACAGCTTTACTCCCTACCTG	For SspB mutation
SspB BhNc5F	CGGGATCCACCATGGTGGA GTACAAGAGCTCTCCAA	For SspB cloning
SspB Hd3R	GCCCAAGCTTATCTAGCTAG TCTACGATCCTCAAATGGGA T	For SspB cloning

6.2 Abbreviation

aa	amino acid
ATR	all-trans-retinal
AQP	aquaporin
ACR	anion-conducting channelrhodopsin
BLUF	sensors of blue light using FAD
bp	base pair
BSA	bovine serum albumin
cAMP	Cyclic adenosine monophosphate
cDNA	complementary DNA
cRNA	complimentary ribonucleic acid
ChR	Channelrhodopsin
CIB	CRY-interacting basic-helix-loop-helix
CID	chemically induced dimerization
CRY	cryptochrome
TEVC	Two Electrode Voltage Clamp
dNTP	deoxynucleotide triphosphate
DTT	dithiothreitol
ELISA	Enzyme-linked immunosorbent assay
FAD	flavin adenine dinucleotide
FMN	flavin mononucleotide
iLID	improved light induced dimer
IPTG	Isopropyl β-D-Thiogalactoside
kb	kilobase
kDa	kilodalton
LB	Lysogeny broth
LED	Light Emitting Diode
LOV	Light-Oxygen-Voltage-sensing
LR	Leucine rich
mRNA	messenger RNA
NMG	N-Methyl-(D)-Glutamine
OD	optical density
PAC	Photoactivated adenylyl cyclase
PAS	Per-Arnt-Sim

|	
PCR	polymerase chain reaction
PCB	phytochromobilin
Phy	phytochrome
PIF	phytochrome-interacting factor
pI	isoelectric point
POI	protein of interest
qPCR	Quantitative PCR
RFU	relative fluorescence units
RNA	ribonucleic acid
SDS	sodium dodecyl sulfate
SDS-PAGE	SDS-polyacrylamide gel electrophoresis
TBST	Tris-buffered Saline with Tween 20
U	Unit
V	Volt
W	Watt
WT	wild type
YFP	yellow fluorescent protein

6.3 Supplement Figure
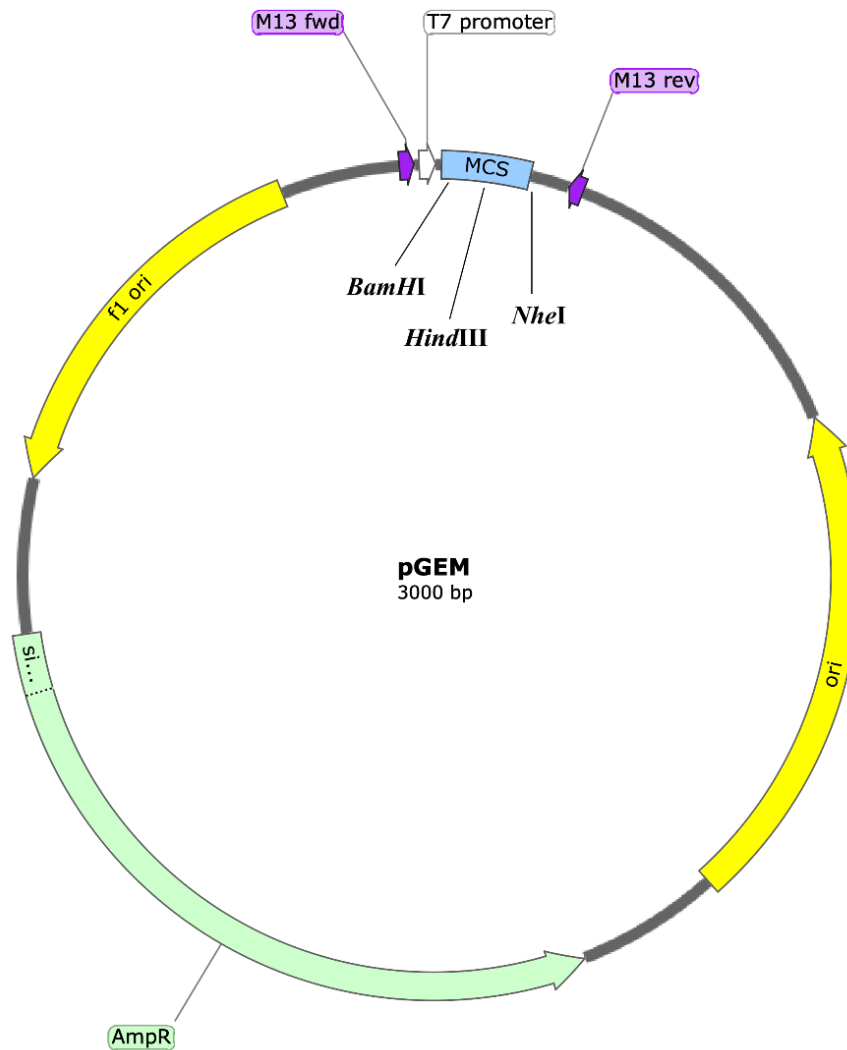
Figure S1 The map of vector pGEM.

pGEM vector was applied to generate cRNA after linearization with *Nhe*I for *Xenopus* oocyte injection. The transcription starts with the T7 promoter *in vitro*. Multiple cloning sites (MCS) region with *BamH*I and *Hind*III was used for target gene connection.
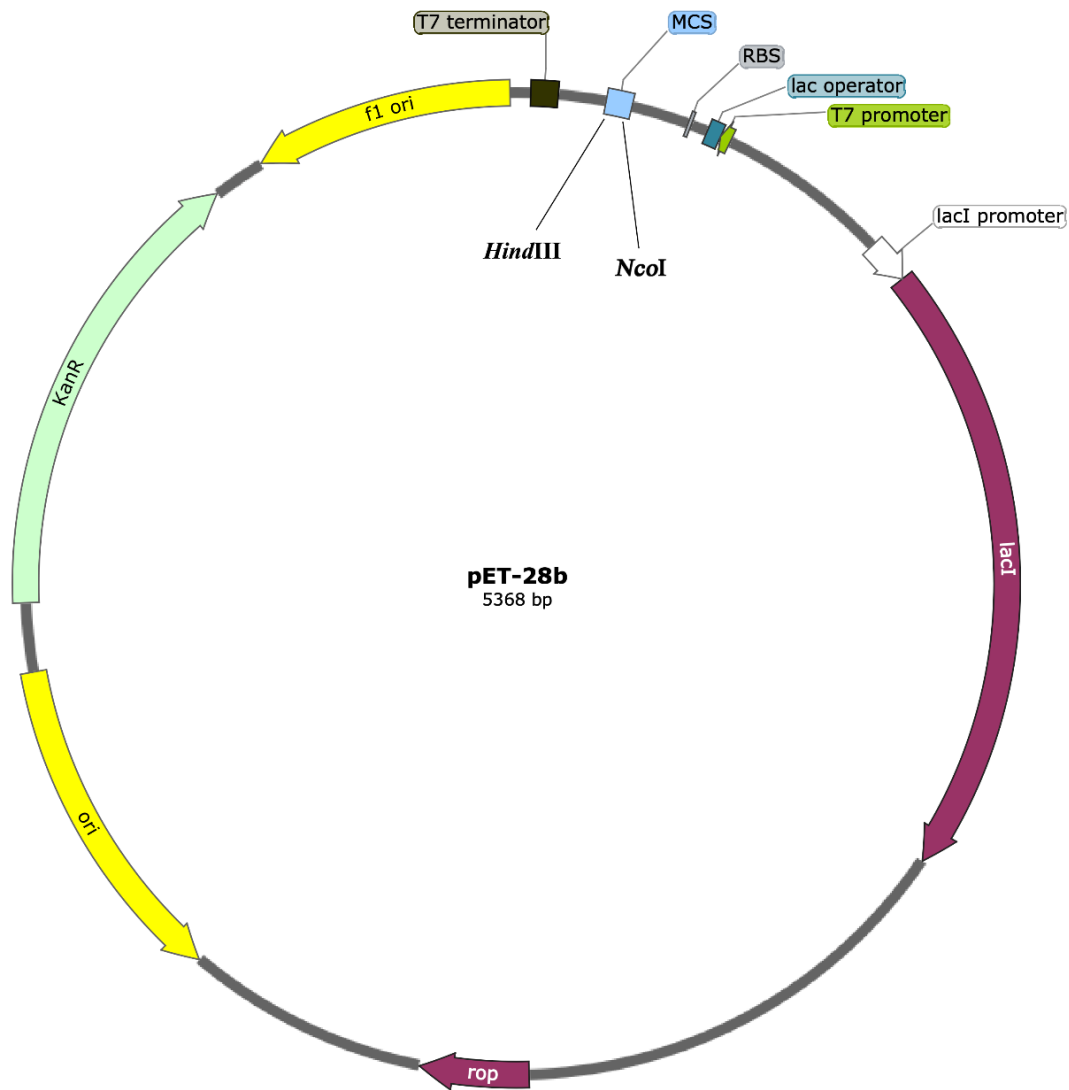
Figure S2 The map of vector pET-28b.

pET-28b vector was applied to target protein overexpression with IPTG stimulation in *E. coli* BL21(DE3). MCS region with *Nco*I and *Hind*III was used for target gene connection.

Acknowledgements

First of all, I would like to express my deepest thanks and sincere appreciation to my supervisor, Prof. Dr. Georg Nagel, for his supervision, discussion and support about my study in these years. In addition, I appreciate my secondary supervisor Prof. Dr. Robert Kittel and third supervisor Prof. Dr. Thomas Müller, for their suggestions during my start-up report and progress report.

I would like to thank Dr. Shiqiang Gao. Under his instructions, I learned many details of experiments and how to solve problems during my study. I also thank our lab members, Yuehui Tian, Yang Shang, Yu Jing, Zhou Yang, Chong Zhang and Yundan Wang, for the help in my experiments.

Many thanks to Prof. Dr. Anna-Leena Sirén and Claudia Häußlein for the help during HEK cell culture.

I want to thank my family for their support, especially my wife Shiwen Chen, who works hard in China and takes care of our daughter during these years.

Declaration of independence

I hereby declare that my thesis entitled "Optogenetic Methods to Regulate Water Transport and Purify Proteins" is the result of my own work. I did not receive any help or support from commercial consultants. All sources and materials applied are listed and specified in the thesis.

Furthermore, I confirm that this thesis has not yet been submitted as part of another examination process neither in identical nor in similar form.

Wuerzburg

Date:

Signature:

Curriculum Vitae

Personal Information

Name: Ruijing Tang

Date and place of birth: 23.10. 1990 in Jiangsu, China

Current address: Rotlöwengasse 1, 97072 Würzburg

E-mail: ruijing.tang@stud-mail.uni-wuerzburg.de

Educational and Working Experience

04.2017 – Now	PhD student in Institute of Physiology, University of Wuerzburg, Germany
11.2016 – 03.2017	Short-term study in Institute of Toxicology and Genetics, Karlsruhe Institute of Technology, Germany
09.2015 – 10.2016	Technician at Jiangsu University, China
09.2012 – 06.2015	Master study in School of Life Sciences, Nanjing University, China
09.2008 – 06. 2012	Bachelor study in School of Biotechnology, Changshu Institute of Technology, China

Publications

Tang R, Yang S, Nagel G, Gao S. An easy optogenetic protein purification method. *submitted*.

Tang R, Xu Y, Ma F, Ren J, Shen S, Du Y, Hou Y, Wang T. Extremely low frequency magnetic fields regulate differentiation of regulatory T cells: Potential role for ROS-mediated inhibition on AKT. Bioelectromagnetics. 2016 Feb;37(2):89-98.

Ren J, Nie Y, Lv M, Shen S, Tang R, Xu Y, Hou Y, Zhao S, Wang T. Estrogen upregulates MICA/B expression in human non-small cell lung cancer through the regulation of ADAM17. Cell Mol Immunol. 2015 Nov;12(6):768-76.

Tang R, Shen S, Zhao X, Nie Y, Xu Y, Ren J, Lv M, Hou Y, Wang T. Mesenchymal stem cells-regulated Treg cells suppress colitis-associated colorectal cancer. Stem Cell Res Ther. 2015 Apr 13;6(1):71.

You M, Dong G, Li F, Ma F, Ren J, Xu Y, Yue H, <u>Tang R</u>, Ren D, Hou Y. Ligation of CD180 inhibits IFN-α signaling in a Lyn-PI3K-BTK-dependent manner in B cells. Cell Mol Immunol. 2015 Feb;14(2):192-202.

Chen S, Zhao G, Miao H, <u>Tang R</u>, Song Y, Hu Y, Wang Z, Hou Y. MicroRNA-494 inhibits the growth and angiogenesis-regulating potential of mesenchymal stem cells. FEBS Lett. 2015 Mar 12;589(6):710-7.

Lv M, Xu Y, <u>Tang R</u>, Ren J, Shen S, Chen Y, Liu B, Hou Y, Wang T. miR141-CXCL1-CXCR2 signaling-induced Treg recruitment regulates metastases and survival of non-small cell lung cancer. Mol Cancer Ther. 2014 Dec;13(12):3152-62.

Tang X, <u>Tang R</u>, Xu Y, Wang Q, Hou Y, Shen S, Wang T. MicroRNA networks in regulatory T cells. J Physiol Biochem. 2014 Sep;70(3):869-75.